INFORMATION TO USERS

This manuscript has been reproduced from the microfilm master. UMI films the text directly from the original or copy submitted. Thus, some thesis and dissertation copies are in typewriter face, while others may be from any type of computer printer.

The quality of this reproduction is dependent upon the quality of the copy submitted. Broken or indistinct print, colored or poor quality illustrations and photographs, print bleedthrough, substandard margins, and improper alignment can adversely affect reproduction.

In the unlikely event that the author did not send UMI a complete manuscript and there are missing pages, these will be noted. Also, if unauthorized copyright material had to be removed, a note will indicate the deletion.

Oversize materials (e.g., maps, drawings, charts) are reproduced by sectioning the original, beginning at the upper left-hand corner and continuing from left to right in equal sections with small overlaps. Each original is also photographed in one exposure and is included in reduced form at the back of the book.

Photographs included in the original manuscript have been reproduced xerographically in this copy. Higher quality 6" x 9" black and white photographic prints are available for any photographs or illustrations appearing in this copy for an additional charge. Contact UMI directly to order.

UMI

A Bell & Howell Information Company
300 North Zeeb Road. Ann Arbor. MI 48106-1346 USA
313/761-4700 800/521-0600

OBSERVATIONS AND GENERATION MECHANISMS OF SLOW-MODE WAVES IN THE MAGNETOSHEATH

A

THESIS

Presented to the Faculty of the University of Alaska

in Partial Fulfillment of the Requirements

for the Degree of

DOCTOR OF PHILOSOPHY

By

Ming Yan, B. S., M. S.

Fairbanks, Alaska

May 1995

OBSERVATIONS AND GENERATION MECHANISMS OF

SLOW-MODE WAVES IN THE MAGNETOSHEATH

by

Ming Yan

RECOMMENDED:

John Craven

Joseph Hawkins

Dave Sentman

Brenton Watkins

Lou Lee, Chairman, Advisory Committee

John Morack, Head, Physics Department

APPROVED:

Paul Reichardt, Dean, College of Natural Sciences

Joseph Kan, Dean of the Graduate School

April 27, 1995

Date

Abstract

The interaction of solar wind with the geomagnetic field leads to the formation of the bow shock, magnetosheath, and magnetopause. Magnetohydrodynamic (MHD) slow-mode structures with a plasma density enhancement and magnetic field depression have been observed to appear frequently in the inner magnetosheath. In addition, the slow-mode structures usually consist of slow-mode waves with a smaller length scale. These slow-mode structures and waves are studied in this thesis through satellite observations and numerical simulations. We find, through satellite observations, that some of the slow-mode structures are associated with Alfven waves in the solar wind. On the other hand, simulations show that slow-mode waves are generated through the interactions between the bow shock and interplanetary shocks, magnetosonic waves, rotational discontinuities, or Alfven waves. The generated slow-mode waves stay in the inner magnetosheath for a long time (about 15 minutes) before the wave energy is convected away tailward. Of particular importance are the interactions between the bow shock and interplanetary rotational discontinuities or Alfven waves. These interactions generate a region with an enhanced plasma density and depressed magnetic field, which is very similar to the slow-mode structures observed in the inner magnetosheath. Based on observations and simulations, it is suggested that the interactions of various types of solar wind fluctuations with the bow shock may lead to the frequent appearance of slow-mode structures and waves in the inner magnetosheath. The generated slow-mode structures have strong pressure variations, and may impinge on the magnetopause as strong pressure pulses.

Table of Contents

List of Figures

Acknowledgments

This thesis is dedicated to my wife, Wei Han, who has shared the sorrow and happiness with me for years.

I would like to thank Professor L. C. Lee, my thesis advisor in the University of Alaska-Fairbanks. He is inspirational in terms of hard working, deep thinking, and dedication. His continuous advice, encouragement, and financial support made the completion of this thesis possible. I am grateful for this opportunity to work with him.

My sincere appreciation also goes to other members of graduate advisory committee. Professors John Craven, Joseph Hawkins, Dave Sentman, and Brenton Watkins. Their concerns and helpful suggestions improved my research work and the quality of my thesis.

My gratitude also extends to Professor Antonius Otto, with whom I have had many stimulating and inspiring conversations. I also thank Professor Paul Song who invited me to High Altitude Observatory, National Center for Atmospheric Research, and open the satellite observational data to me for the study of Chapter 2 of this thesis. I would also thank Professor Eric Priest and Dr. Harry Petschek for helpful discussions.

This thesis work was supported by grants from the National Aeronautics and Space Administration, the National Science Foundation, and the Department of Energy to the University of Alaska Fairbanks. The computer work was supported by the Computer Service Center of the Geophysical Institute and the Pittsburgh Supercomputer Center.

Chapter 1 Introduction

The solar wind and interplanetary magnetic field drive geomagnetic activity. However, it is the magnetic field and the plasma in the magnetosheath downstream of the bow shock that directly impinge onto the magnetopause. Hence an understanding of solar wind control of the magnetosphere must include the intervening processes associated with the bow shock and the magnetosheath. Figure 1.1 is a schematic plot of the solar wind, bow shock, magnetopause, and the magnetosheath.

The purpose of this thesis is to study the nonlinear interaction between the Earth's bow shock and interplanetary magnetohydrodynamic fluctuations, which include interplanetary shocks, rotational discontinuities, large-amplitude Alfven waves, and magnetosonic waves. The emphasis is on the generation of slow-mode waves or structures with anti-correlated plasma density and magnetic field, and their propagation in the nonuniform magnetosheath. This study tries to explain the slow-mode structures recently observed in the inner magnetosheath [*Song et al.*, 1990; 1992].

In this chapter, we briefly review existing knowledge about the magnetosheath and its nearby environment, which includes the solar wind, bow shock, and magnetopause. Then we describe the motivation and outline of this thesis.

1.1 General Properties of the Solar Wind, Bow Shock, and Magnetopause

1.1.1 Solar Wind Properties at Earth's Orbit

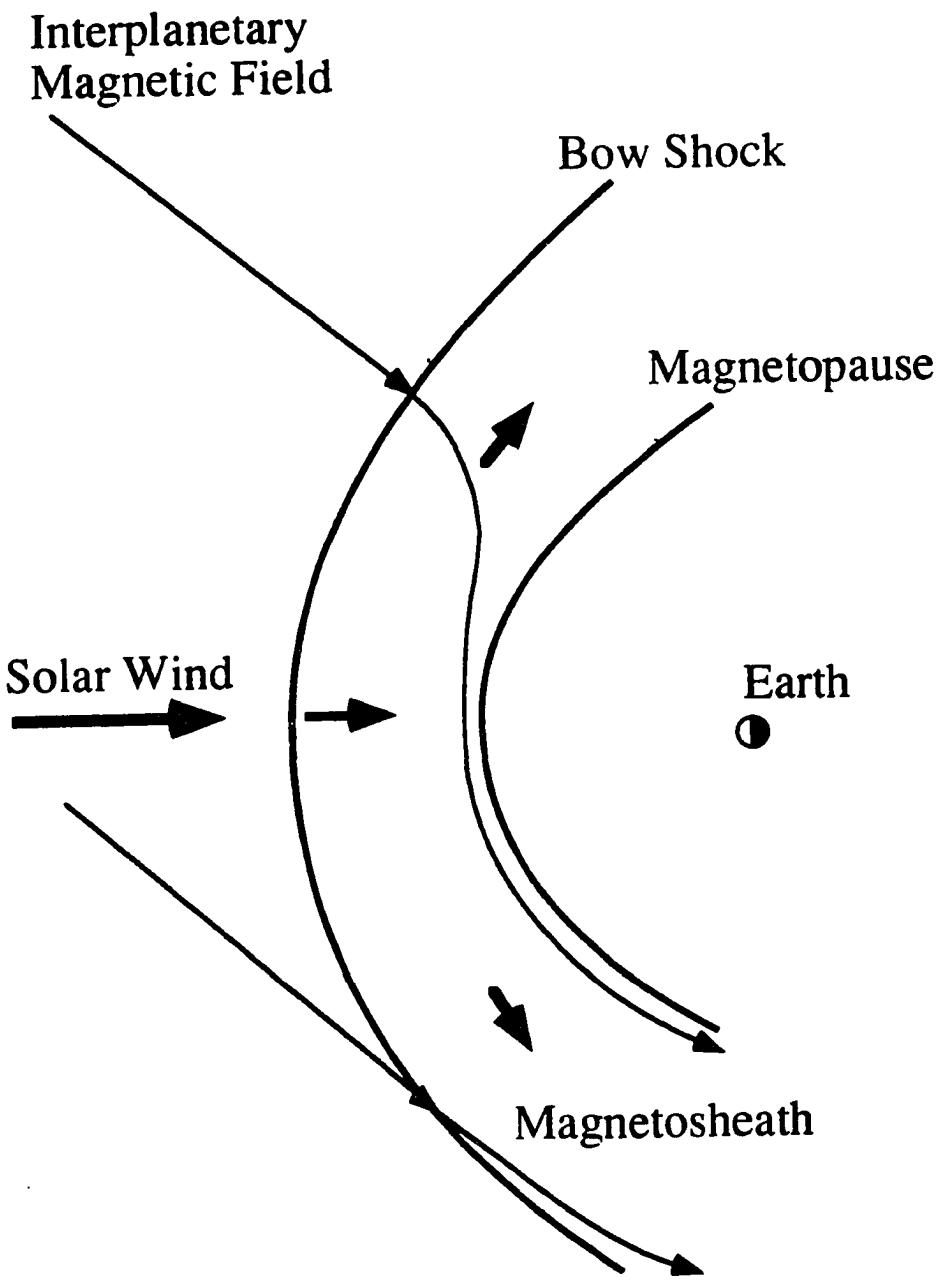

Figure 1.1 A schematic plot of the solar wind, bow shock, magnetopause and the magnetosheath.

Knowledge of the solar wind as it approaches Earth's bow shock is fundamental to all understandings of the present subject. Various satellite observations showed that the solar wind plasma number density ranges between 0.4 and 80 cm^{-3} with an average of 5 cm^{-3} [*Brandt*, 1970; *Wolfe*, 1972]. The solar wind flow is basically in the radial direction away from the Sun [*Wolfe*, 1970]. The speed ranges from 200 to 900 km/s with an average around 400 km/s [*Hundhausen*, 1972]. The average proton temperature is 4×10^4 K. The average electron temperature is 1.5×10^5 K, larger than the proton temperature. The electron temperature is almost isotropic with an average $T_{\|}/T_{\perp} = 1.08$. The proton anisotropy is strong with an average $T_{\|}/T_{\perp} = 1.48$ [*Wolfe*, 1972].

The interplanetary magnetic field (IMF) embedded in the solar wind as it approaches the bow shock is predominantly aligned near the ecliptic plane and oriented at 45° from the line joining the Sun and Earth [*Ness et al.*, 1966]. The amplitude of the interplanetary magnetic field ranges from 0.25 to 40 nT with an average value of 6.0 nT [*Ness et al.*, 1966].

The Alfven speed V_A depends on the amplitude of the magnetic field and the plasma density. Taking average value of the magnetic field $B = 6$ nT and the plasma density $n = 5$ cm^{-3}, the solar wind Alfven speed is around 60 km/s. The sound speed V_s for ideal gas depends only on temperature. Suppose the solar wind has a temperature of 10^5 K, the sound speed comes out to be 50 km/s. The solar wind flow speed V is much larger than the phase speed of the fast mode wave. The average solar wind Alfven Mach number $M_A \equiv V/V_A$ and the Mach number $M \equiv V/V_s$ are both between 6 and 7 [*Fairfield*, 1971]. The plasma β is defined as P/P_B, where P and P_B are the thermal and magnetic pressure, respectively. In the solar wind, the plasma β varies around unity.

Slow-mode waves usually cannot be observed in the solar wind because they are strongly damped [*Barnes*, 1966; *Barnes and Choe*, 1977; *Hada and Kennell*, 1985]. Alfven waves are observed frequently because there is little damping associated with them. About half of the time, Alfven waves are the main micro-structures of the solar wind [*Belcher and Davis*, 1971]. Almost all the Alfven waves observed at Earth's orbit are propagating away from the Sun. Fast-mode waves are also observed sometimes, because their damping is intermediate between that of Alfven and slow-mode waves.

Tangential discontinuities arrive as frequently as every several minutes to several hours and tend to be aligned with the IMF [*Siscoe et al.*, 1968; *Burlaga*, 1969; *Tuner and Siscoe*, 1971]. Rotational discontinuities arrive as frequently as the tangential discontinuities, and except for the thickness of the transition layer in which the magnetic field makes the rotation, they are not different from the large-amplitude Alfven waves. Contact discontinuities have not been observed in the solar wind. It is widely believed that they will not be observed because they would rapidly broaden into a smooth transitions.

Most of the shocks observed at 1 AU are forward fast shocks. Only a few slow shocks have been identified [*Chao and Olbert*, 1970; *Burlaga and Chao*, 1971], and one of them was identified as a reverse slow shock [*Burlaga and Chao*, 1970]. The propagation speeds of the shocks in the solar wind frame are usually around 150 km/s corresponding to a Mach number or Alfven Mach number of between 2 and 3. The dynamic pressure can increase by a factor of 20 across solar wind shocks, but factors of 3 are more common [*Siscoe*, 1968].

1.1.2 Bow Shock

The bow shock, the outer boundary of the magnetosheath, is a stationary reverse fast shock that propagates towards the Sun in the solar wind frame at a speed equal to the solar wind speed. According to MHD theory, the two sides of any stationary shock or discontinuity have to satisfy the following Rankine-Hugoniot jump conditions [*Landau and Lifshitz*, 1960]:

$$[\rho v_n] = 0 \tag{1.1}$$

$$[\rho v_n \mathbf{v_t} - B_n \mathbf{B_t}/\mu_0] = 0 \tag{1.2}$$

$$[\rho v_n^2 + P + B^2/2\mu_0] = 0 \tag{1.3}$$

$$[(\rho v^2/2 + \varepsilon + P + B^2/\mu_0)v_n - B_n^2 v_n/\mu_0 - B_n(\mathbf{B_t} \cdot \mathbf{v_t})/\mu_0] = 0 \tag{1.4}$$

$$[B_n] = 0 \tag{1.5}$$

$$[B_n \mathbf{v_t} - v_n \mathbf{B_t}] = 0 \tag{1.6}$$

where $\varepsilon = \rho v^2/2 + \frac{P}{\gamma - 1} + \frac{B^2}{2\mu_0}$, the subscripts n and t denote the components normal and tangential to the discontinuity surface, respectively, and the square brackets denote the difference between the values on the two side of the discontinuity.

Across the bow shock, the plasma flow speed decreases from super-fast to sub-fast speed in the direction normal to the shock. At the same time, plasma density, temperature, and thermal pressure are all enhanced. The tangential magnetic field is also enhanced to make the magnetic field more aligned to the shock front. Across the bow shock, plasma bulk flow energy is converted to plasma thermal energy and magnetic energy.

The bow shock, like interplanetary shocks, is a collisionless shock. Collisionless shocks are divided into two categories according to the direction of the magnetic field relative to the shock normal: quasi-parallel shocks and quasi-perpendicular shocks. Observationally, a quasi-parallel shock consists of a broad (1-2 R_E thick) magnetic

profile, is very turbulent, and has no easily definable upstream-to-downstream transition in the magnetic field [*Greenstadt et al.*, 1970a, b; *Greenstadt and Fredricks*, 1979]. By contrast, a quasi-perpendicular shock possesses a well-defined transition and confined turbulence. At Earth's bow shock, the boundary between these two extremes generally occurs when the shock normal and the upstream magnetic field make an angle of 50° [*Greenstadt et al.*, 1970a, b; *Diodato*, 1976]. The shock is quasi-parallel when the angle is less than 50°, and quasi-perpendicular otherwise. At any instant, part of the bow shock is quasi-parallel while the other part is quasi-perpendicular.

Some ions are energized and reflected back into the solar wind at the quasi-parallel shock. The population of the bow-shock reflected ions in the upstream region consists of two distinctly different components, the reflected and the diffuse components [*Gosling et al.*, 1978]. While the reflected ions show the characteristics of a beamlike distribution which streams away from the shock along magnetic field lines, the diffuse component is generally more isotropic with a shock-directed bulk velocity slower than the solar wind speed. Each population has a number density of about 10% of the solar wind density [*Bonifazi and Moreno*, 1981]. Generally, the energetic particles in the upstream region are accompanied by hydromagnetic waves in the frequency range from 0.01 to 0.3 Hz [*Fairfield*, 1969; *Hoppe et al*, 1981] that are believed to be excited by the reflected ion beams. As the upstream waves are convected back to the shock, they steepen and are responsible for the cyclic reformation of the bow shock [*Scholer*, 1993]. The fluctuations can be convected into the magnetosheath by the plasma flow [*Crooker et al.*, 1981; *Luhmann et al.*, 1986].

1.3.3 Magnetopause

The magnetopause, inner boundary of the magnetosheath, is the interface between the magnetosheath plasma and magnetic field and those of the magnetosphere. The magnetopause is normally a tangential discontinuity which satisfies the following conditions [*Landau and Lifshitz*, 1960]:

$$v_n = B_n = 0 \tag{1.7}$$

$$[P + P_B] = 0 \tag{1.8}$$

On the magnetospheric side, the plasma density is very low and the temperature is high. The thermal pressure is negligible compared to the magnetic pressure. On the magnetosheath side, the thermal pressure and magnetic pressure are of the same order.

The position of the stationary magnetopause is theoretically determined by total pressure balance between the magnetosheath and the magnetosphere. However, the shape and position can be calculated quite accurately by the balance between the solar wind dynamic pressure and the dipole field of the magnetosphere [*Mead and Beard*, 1964; *Spreiter and Brigges*; 1962]. The earliest model for the equilibrium position of the magnetopause was given by *Chapman and Ferraro* [1937], who estimated that the magnetopause stand-off distance at the subsolar point as

$$D = \left(\frac{B_0}{4\pi m n V^2}\right)^{1/6} R_E \tag{1.9}$$

where $B_0 = 0.312$ Gauss is the strength of Earth's equatorial surface magnetic field, and m is the proton mass. Assuming the number density n of the solar wind is between 2 and 10 cm^{-3}, and the speed of the solar wind V is between 300 and 700 km/s, the stand-off distance is estimated to be around 10 R_E according to Equation 1.9.

The magnetopause is actually a layer with complex structures. The magnetopause current layer, in which the magnetic field evolves from that of the magnetosphere to the magnetosheath, has a thickness that ranges between 200 to 1800 km with an average of about 900 km or $\sim$ 10 ion gyroradii [*Elphic and Russell*, 1979; *Berchem and Russell*, 1982]. Magnetic reconnection [*Petschek*, 1964; *Yan et al.*, 1992, 1993, 1994] may occur when the shear between the magnetic field of the magnetosheath and that of the magnetosphere is large [*Russell and Elphic*, 1979; *Lee and Fu*, 1985], in which case the magnetopause current layer becomes a rotational discontinuity [*Levy et al.*, 1964; *Lin and Lee*, 1994].

1.2 Models and Observations of the Steady Magnetosheath

1.2.1 Gasdynamic Model

The gasdynamic model of the magnetosheath was developed about 30 years ago by *Spreiter* and his colleagues [*Spreiter et al.*, 1966; *Spreiter and Alksne*, 1969; 1970]. It is valid only in the region where the inertia force of the plasma flow is much larger than the magnetic force. As the first step in creating the model, the shape and position of the magnetopause are determined by pressure balance as described in subsection 1.1.3. Then, the position and shape of the bow shock, together with the plasma density, thermal pressure, temperature, and the plasma flow, are calculated by gasdynamic theory neglecting the influence of magnetic field. Finally, the magnetic field is calculated using the flow velocity obtained in the second step and the frozen-in condition for the magnetic field.

Once the shape and position of the magnetopause are determined, the plasma flow around the magnetopause can be calculated. Since the average Alfven Mach number is over 6 in the solar wind, and large in most of the magnetosheath's volume, the magnetic force is usually much smaller than the plasma's inertia force. Therefore, the plasma density ρ, thermal pressure P, the plasma flow velocity $\mathbf{v}$ can be determined by the following gasdynamic equations by neglecting the effect of the magnetic field:

$$\nabla \cdot (\rho \mathbf{v}) = \mathbf{0} \tag{1.10}$$

$$\rho \mathbf{v} \cdot \nabla \mathbf{v} + \nabla P = 0 \tag{1.11}$$

$$\mathbf{v} \cdot \nabla S = 0 \tag{1.12}$$

where $S = \ln P/\rho^{\gamma}$. The jump conditions (1.1-1.6) at the bow shock can then be simplified as

$$[\rho v_n] = 0 \tag{1.13}$$

$$[\mathbf{v_t}] = 0 \tag{1.14}$$

$$[\rho v_n^2 + P] = 0 \tag{1.15}$$

$$[\rho v_n (h + v^2/2)] = 0 \tag{1.16}$$

where $h = \varepsilon + P$ and $\varepsilon = \rho v^2/2 + \frac{P}{\gamma - 1}$. The boundary condition at the magnetopause is

$$v_n = 0. \tag{1.17}$$

For an ideal gas, the jump conditions (1.13)-(1.16) can be written as

$$\frac{\rho_b}{\rho_\infty} = \frac{(\gamma+1)M_\infty^2}{(\gamma-1)M_\infty^2 + 2} \tag{1.18}$$

$$\frac{P_b}{P_\infty} = \frac{2\gamma}{\gamma+1} M_\infty^2 - \frac{\gamma-1}{\gamma+1} \tag{1.19}$$

$$M_b^2 = \frac{2 + (\gamma+1)M_\infty^2}{2\gamma M_\infty^2 - (\gamma-1)} \tag{1.20}$$

where $M = v/V_s$ is the Mach number based on the local sound speed V_s, subscripts

b and ∞ indicate the regions just downstream and upstream of the bow shock, respectively. To simplify the calculation, the magnetopause is assumed to be symmetric around the Sun-Earth line. Figure 1.2 shows the preassumed shape of the magnetopause, and the calculated position of the bow shock, streamlines, contours of the plasma density, temperature, and the flow speed. The plasma flow velocity is deflected, first at the bow shock, and then again in the magnetosheath, to make it around the magnetopause. Below the sonic line around the subsolar area, the plasma flow speed is smaller than the local sound speed. The flow speed increases above the local sound speed farther tailward of the sonic line. The plasma density jump across the bow shock is close to its maximum value in most of the dayside region with the maximum density and temperature appearing at the stagnation point. The temperature at the stagnation point is 22.3 times as high as that in the solar wind.

Calculations for various values of MI_∞ and γ show that the ratio between the magnetosheath thickness Δ and the magnetopause stand-off distance D at the subsolar point is close to the ratio of the plasma densities upstream and downstream of the bow shock:

$$\frac{\Delta}{D} = 1.1\frac{\rho_\infty}{\rho_b} = 1.1\frac{(\gamma-1)MI_\infty^2+2}{(\gamma+1)MI_\infty^2}. \qquad (1.21)$$

When $MI_\infty >> 1$ and $\gamma = 2$, $\Delta/D \approx 1/3$.

Once the plasma flow around the magnetopause is obtained, the magnetic field

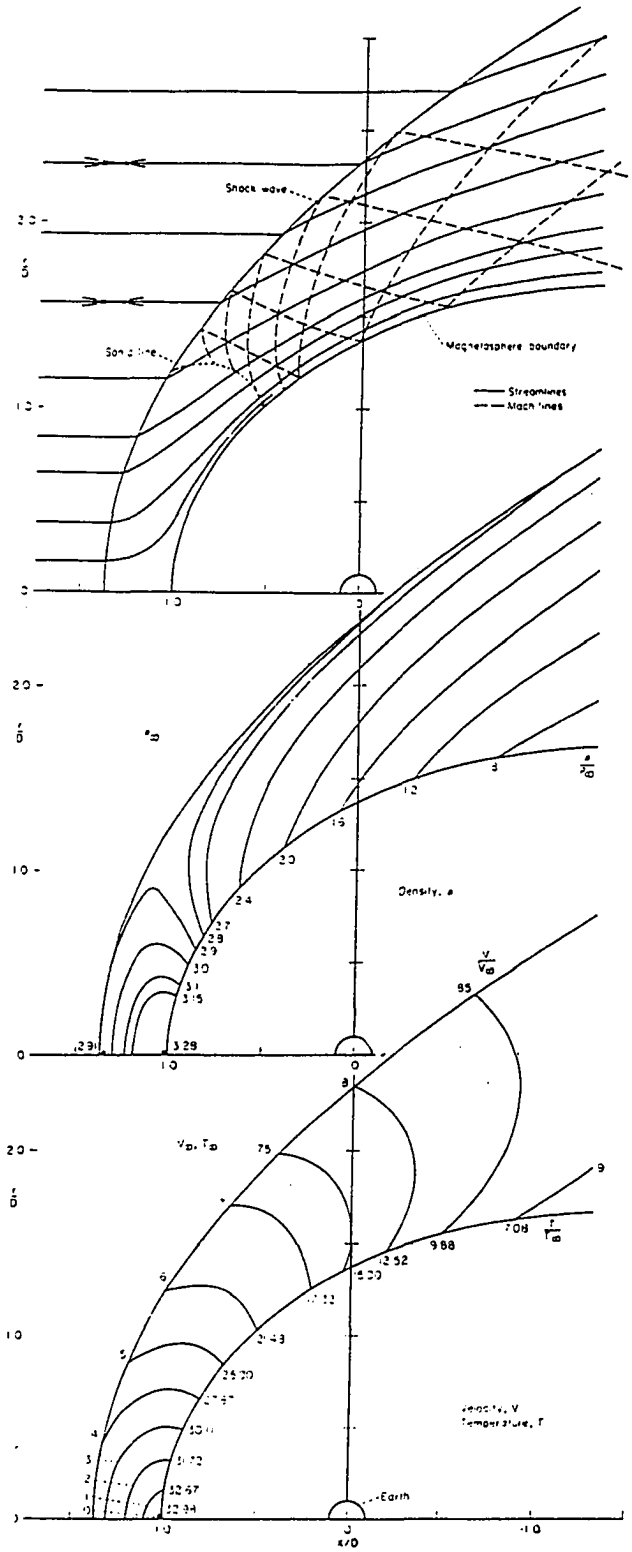

Figure 1.2 The preassumed shape of the magnetopause, the calculated shape and position of the bow shock, and the streamlines (upper panel), contours of the plasma density (center panel), temperature, and flow speed (lower panel) obtained by the gasdynamic model when $M_\infty = 8$ and $\gamma = 2$ [*Spreiter et al.*, 1966].

can be calculated by the following frozen-in equation for steady state,

$$\nabla \times (\mathbf{v} \times \mathbf{B}) = 0 \tag{1.22}$$

and

$$\nabla \cdot \mathbf{B} = 0. \tag{1.23}$$

The jump condition at the bow shock is

$$[B_n] = 0 \tag{1.24}$$

and the boundary condition at the magnetopause is

$$B_n = 0. \tag{1.25}$$

The calculated magnetic field lines corresponding to an interplanetary magnetic field with a 45° angle from the solar wind flow is shown in Figure 1.3a.

Given the shapes and positions of the magnetopause and the bow shock, the steady magnetic field in the magnetosheath is determined only by the interplanetary magnetic field [*Kobel and Fluckiger*, 1994] assuming there is no current inside the magnetosheath. Figure 1.3b shows the calculated magnetic field that corresponds to the same IMF conditions as Figure 1.3a. The draping and pile up of the magnetic field lines appear in front of the magnetopause, and magnetic field pile up occurs over most of the magnetosheath.

In the gasdynamic theory, the plasma parameters and flow are all symmetric about the Sun-Earth line since the shape of the magnetopause is assumed to be symmetric, but the magnetic field is usually not symmetric about the Sun-Earth line as shown in Figure 1.3. In MHD theories, the asymmetry of the magnetic field will eventually lead to asymmetry of the plasma parameters and flow in the magnetosheath. In the real

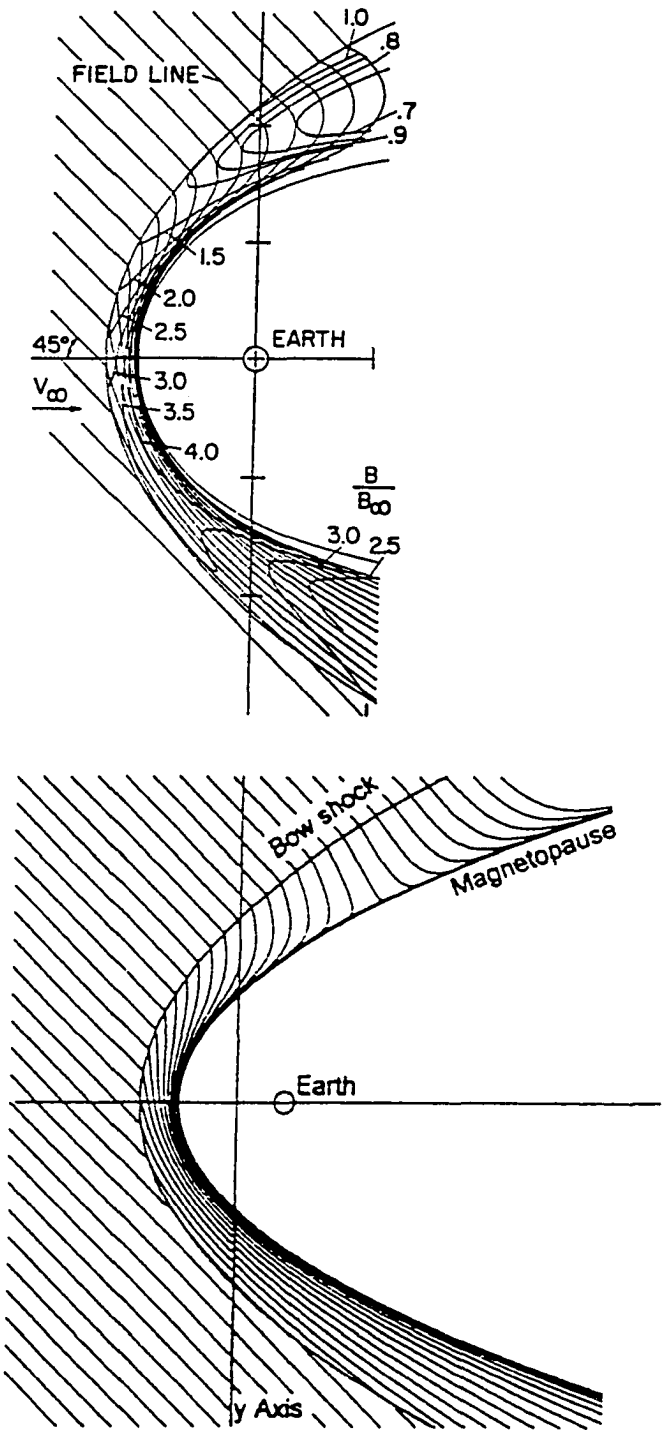

Figure 1.3 The steady magnetic field in the magnetosheath. Figure 1.3a is obtained from the gasdynamic model [*Spreiter et al.*, 1966]. Figure 1.3b is obtained from the analytical magnetic field model of *Kobel and Fluckiger* [1994].

magnetosheath, strong asymmetry is observed on fluctuations of the magnetosheath plasma and magnetic field parameters. The fluctuations are in the same order of the background values in the region downstream of a quasi-parallel bow shock, and much smaller in the region downstream of a quasi-perpendicular shock, which will be discussed later in this chapter.

1.2.2 Magnetohydrodynamic Models

Midgley and Davis [1963] and *Lees* [1964] predicted a decrease of plasma density in the magnetosheath region adjacent to the magnetopause due to compression of draped magnetic field lines against the dayside magnetopause. *Zwan and Wolf* [1976] worked out the idea in great detail, and showed that the pile up of the magnetic flux squeezes the plasma out of the region along the magnetic field as the cross sections of the flux tubes becomes smaller. A depletion layer, a region of very low plasma density, is formed just outside the magnetopause. For the case of Earth with a magnetopause standoff distance of 10 R_E, the theories predicted that the density should be reduced by a factor of ≥ 2 in a layer of about 700-1300 km thick if the solar wind Alfven Mach number M_A is 8. The layer thickness should vary as M_A^{-2}. The predicted plasma density and magnetic field variations from the bow shock to the magnetopause are given in Figure 1.4. *Zwan and Wolf* also speculated that the magnetic reconnection, which is believed to take place at the magnetopause when the magnetic shear is high, would make the depletion process less efficient.

A full three-dimensional MHD model of the stationary magnetosheath was analyzed numerically by *Wu* [1992]. In the steady configuration, the amplitude of the magnetic field increases from the bow shock to the magnetopause, and there is a region in front of the magnetopause in which the magnetic field is enhanced. The plasma density increases first, then decreases from the bow shock to the magnetopause. In

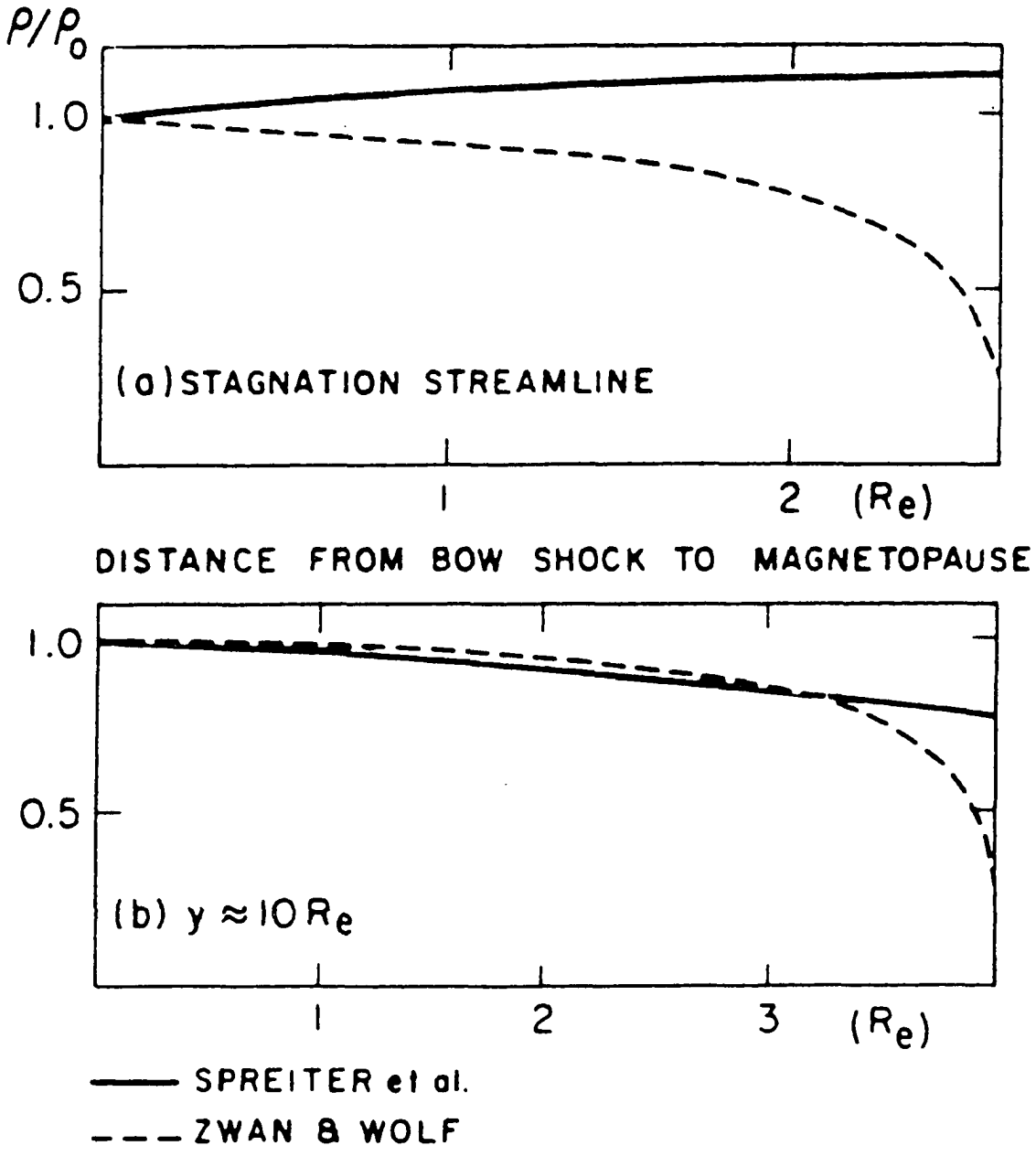

Figure 1.4 The profiles of plasma density across the magnetosheath as predicted by the gasdynamic model and the MHD model of *Zwan and Wolf* [1976]. Profiles from the gasdynamic model are also shown as comparison

the region where the magnetic field is strong, the plasma density becomes small. This region is the depletion layer predicted by *Lees* [1964] and *Zwan and Wolf* [1976]. However, the depletion layer is about 1/3 of the magnetosheath thickness in the simulation, much thicker than the predicted. The discrepancy might come from numerical dissipation involved in the numerical calculation.

1.2.3 Observational Results

Satellite observations show that the average positions of the magnetopause and the bow shock agree very well with the above theories [*Fairfield*, 1971]. Figure 1.5 is taken from the paper by *Farris et al.* [1991], with the circles and the crossings indicating the positions of the magnetopause and the bow shock, respectively. The curves are best fits to the observational data. The average stand-off distance is 10.3($\pm$0.3) R_E for the magnetopause, and 13.7($\pm$0.2) R_E for the bow shock, which corresponds to a subsolar thickness of 3.4 R_E for the magnetosheath. On the dawn-dusk meridian, the geocentric distance to the magnetopause is about 15 R_E and the magnetosheath thickness is about 10 R_E. The statistical analysis is over 351 independent bow shock crossings and 233 independent magnetopause crossings.

Paschmann et al. [1978] and *Crooker et al.* [1979] first reported evidence of the plasma depletion layer. In a recent statistical study by *Phan et al.* [1994], a depletion layer exists when the magnetosheath magnetic field piles up against the magnetopause when the magnetic shear is below 30°. The average thickness of the region is around 10 minutes in satellite observations which corresponds to a spatial distance of about 1200 km. This observed thickness agrees with the prediction by *Zwan and Wolf* [1976] for the plasma depletion layer. Observations show that the plasma density, β value, and proton and electron temperatures in the layer are lower than those in the magnetosheath region upstream of the layer. However, when the

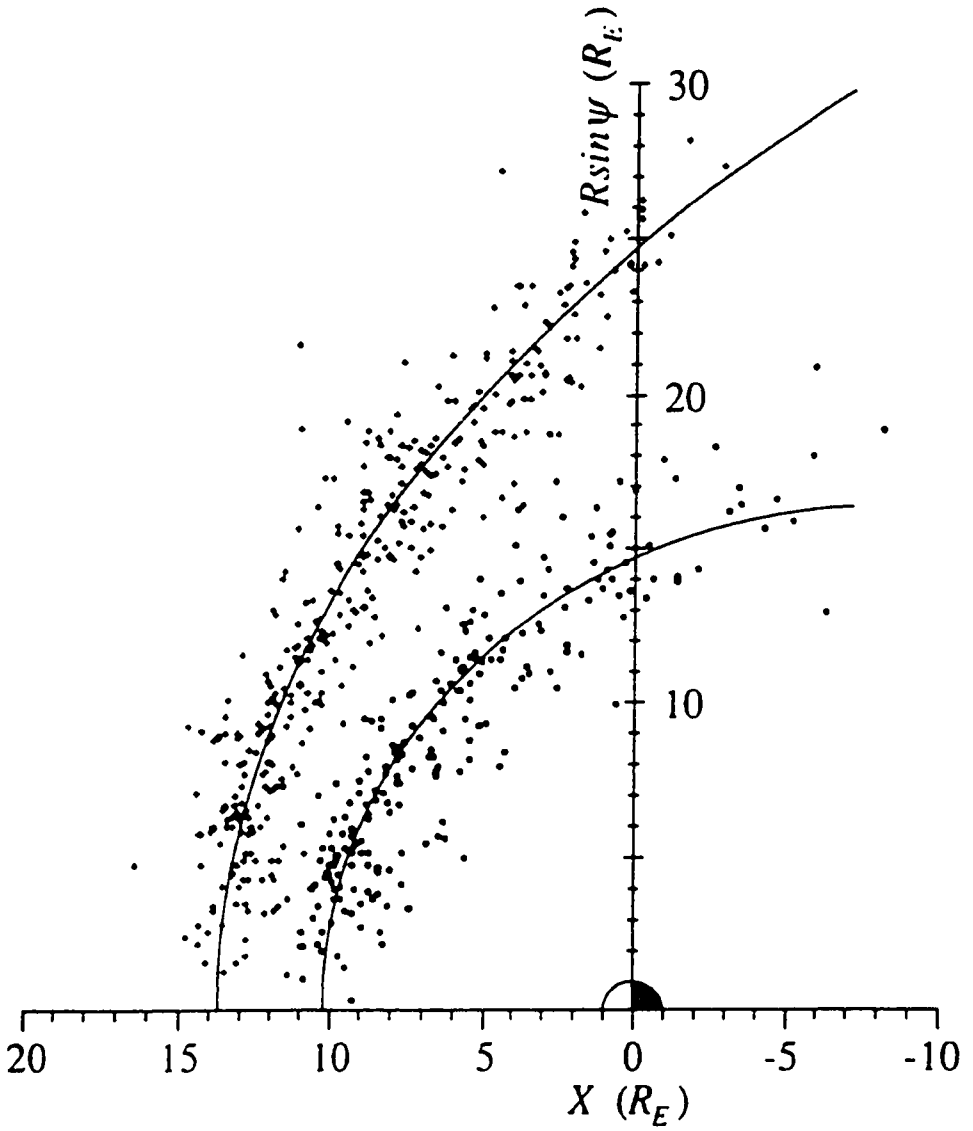

Figure 1.5 The satellite magnetopause and bow shock crossings, and the best fits to the observational data. Circles represent magnetopause crossings and crosses denote bow shock crossings [*Farris et al.*, 1991].

magnetic shear across the magnetopause is larger than 60°, the magnetic field does not pile up in the immediate vicinity of the magnetopause, and no systematic variations of the plasma parameters are observed in this region.

1.3 Plasma Waves in the Magnetosheath

The earliest measurements showed that the magnetosheath fluctuations were 10 to 100 times more intense than those in the magnetosphere or the solar wind [*Holzer et al.*, 1966]. The following waves have been identified in the magnetosheath: mirror wave, Alfven wave, ion acoustic wave, magnetosonic wave, and ion cyclotron wave.

1.3.1 Waves Convected from the Bow Shock

For quasi-perpendicular shocks, the ions have a sharp peak in $T_\perp/T_{||}$ just downstream of the shock which rapidly decays to less than 1.5 [*Gosling and Robson*, 1985; *Lee et al.*, 1988; *Hubert et al.*, 1989]. The high $T_\perp/T_{||}$ distributions drive cyclotron and mirror instabilities that pitch angle scatter the ions. The waves then propagate and are convected downstream [*Winske and Quest*, 1988].

The magnetosheath field is turbulent downstream of quasi-parallel shocks, and amplitude and direction of magnetic field are highly variable, with $\delta\mathbf{B} \approx \mathbf{B}$. For quasi-parallel shocks, backstreaming ions produce upstream waves which convect back to the shock and steepen, cyclically reforming the shock [*Scholer*, 1993]. The wave behavior at quasi-parallel shocks has been studied theoretically [*Krauss-Varban and Omidi*, 1991; *Scholer et al.*, 1993]. Upstream magnetosonic waves convert to Alfven or ion acoustic waves at the shock. Therefore, waves convected from the quasi-parallel shock originate as upstream waves rather than as instabilities generated at the shock.

1.3.2 Waves Generated by Local Instabilities

The earliest vector magnetic field observations in the magnetosheath reported large compressional, $\delta B/B_0 \approx 0.5$, $\delta B_\perp/B_0 << 1$, quasi-sinusoidal waves in the magnetosheath [*Kaufmann et al.*, 1970], and the mirror instability was immediately invoked to account for the features. *Tsuritani et al.* [1982] subsequently found that the waves exhibit features predicted for the mirror mode, in which magnetic and thermal pressures oscillate in anti-phase.

Crooker and Siscoe [1977] showed that magnetosheath flow implies the development of

$$\beta_\perp/\beta_\parallel >> 1 + 1/\beta_\perp \tag{1.26}$$

on the dayside for quasi-perpendicular IMF. As a magnetosheath flux tube converts earthward, the subsolar cross section A decreases, while the length L increases. The double adiabatic relations imply

$$\frac{d}{dt}(T_\perp A) = 0 \tag{1.27}$$

$$\frac{d}{dt}(T_\parallel L^2) = 0 \tag{1.28}$$

The transverse compression increases $T_\perp$ whereas the longitudinal expansion decreases $T_\parallel$. The mirror mode should therefore be unstable throughout nearly all of the dayside magnetosheath. Significantly, *Phan et al.* [1994] found $\beta_\perp/\beta_\parallel \approx 1 + 1/\beta_\perp$, strongly suggesting that the instability regulates $\beta_\perp/\beta_\parallel$.

Ion cyclotron waves have also been observed in the magnetosheath. *Fairfield* [1976] found that transverse fluctuations below about 1 Hz are fairly common near the magnetopause. Cyclotron and mirror fluctuations predominate for different ranges of plasma parameters. The cyclotron waves are common for $\beta < 1$ in the depletion

layer whereas mirror fluctuations are most often separated from the magnetopause by an interval of cyclotron waves [*Sckopke et al.*, 1990; *Anderson et al.*, 1993].

1.4 Slow-Mode Waves and Structures in the Inner Magnetosheath

Recently, *Song et al.* [1990, 1992] reported observations which indicate that slow-mode structures with enhanced plasma density and depressed magnetic pressure appear frequently in the inner magnetosheath. Figure 1.6 shows one of the examples reported in their paper [*Song et al.*, 1992]. In the period between 1533 to 1609 UT, the overall plasma density is enhanced from the background value while the amplitude of the magnetic field is depressed. This region is in the inner magnetosheath but slightly away from the magnetopause. The anti-correlation between the plasma thermal pressure and the magnetic pressure indicates that the structure is a slow-mode structure. Propagation in the direction normal to the magnetopause is found to be very small. Note that both the outer and inner edges of the structure steepen like the shock profiles. There are slow-mode waves with anti-correlated plasma density and magnetic field in the big slow-mode structure. Figure 1.7 shows the density enhancement relative to the background value versus the local plasma β value. It is obvious that the density enhancement in the slow-mode structure increases with decreasing β value. The above observations are confirmed by *Hubert et al.* [1994].

In summary, the slow-mode structures have the following observational properties. (a) The structures have an overall enhanced plasma density and depressed magnetic field. (b) The outer edge of the observed structures does not convect with the magnetosheath plasma flow; they seem to stand against the magnetosheath flow. (c) There are smaller scale fluctuations with anti-correlated plasma density and magnetic field in the slow-mode structure. (d) They are observed frequently in the inner

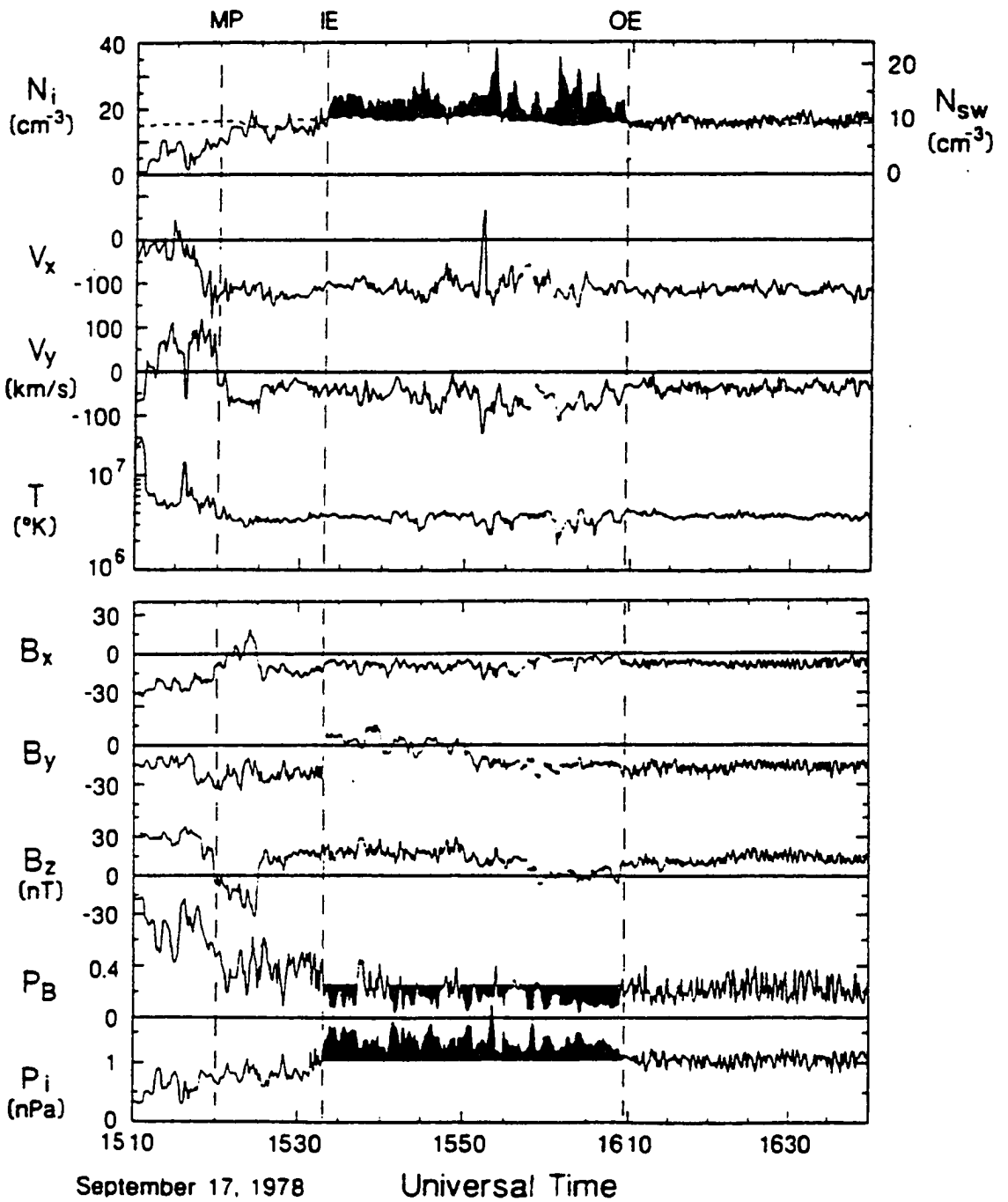

Figure 1.6 An outbound magnetosheath pass with a density maximum and anti-correlated magnetic field in front of the magnetopause [*Song et al.*, 1992].

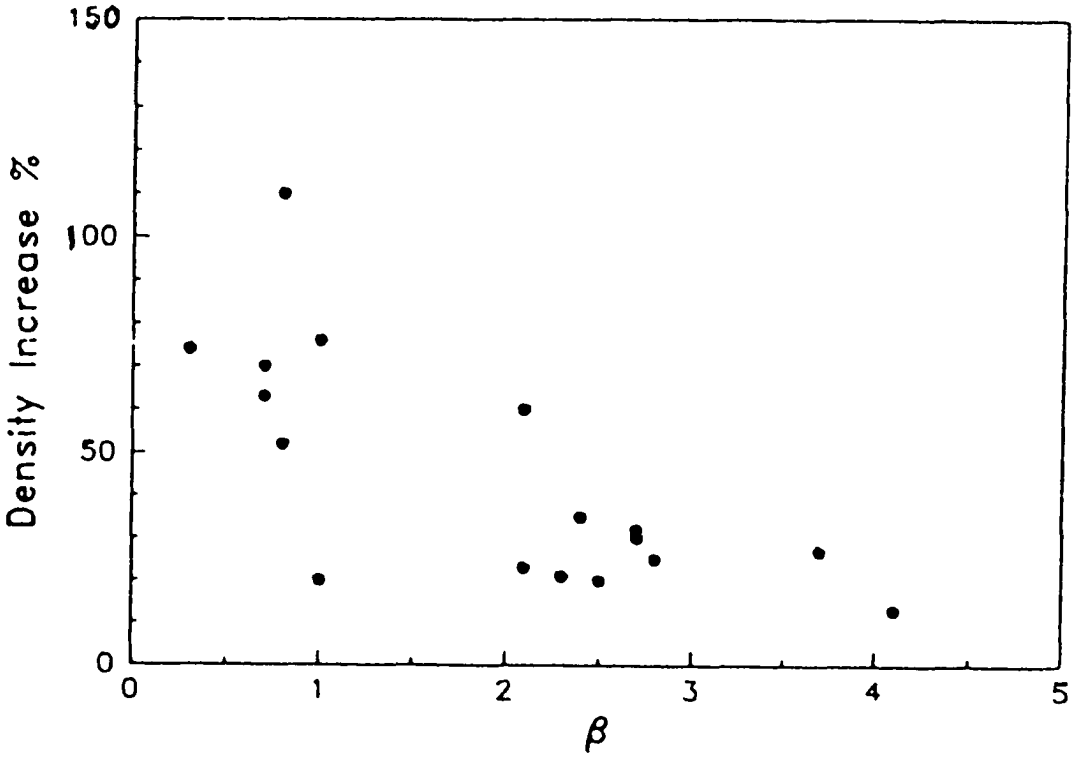

Figure 1.7 The fractional density increase relative to the ambient magnetosheath density versus plasma β for the magnetosheath passes with the density maximum [*Song et al.*, 1990].

magnetosheath. (e) The relative density enhancement in the structures increases with a decreasing plasma β value. (f) The wavelength of (λ_n) in the direction normal to the magnetopause is typically 2000-6000 km while the wavelength (λ_t) in the tangential direction is much larger than λ_n. (g) The plasma density variations at the edges of the structure are steepened with shock-like profiles.

A few theoretical mechanisms have been devised to explain the observed slow-mode structures since the observations were reported. *Lee et al.* [1991] conducted a two-dimensional MHD simulation for the region close to the stagnation point. The magnetic field lines, streamlines, and contours of plasma density and amplitude of the magnetic field resulting from that work are shown in Figure 1.8. The simulation results show that the bending of magnetic field lines in front of the magnetopause may correspond to the observed slow-mode structure in which plasma density or pressure increases first then decreases. *Southwood and Kivelson* [1991] calculated the possible slow shock front orientation in front of the magnetopause given that the shock waves are excited by some sources at the magnetopause. It was found that the shock front may be closer to the magnetopause on one side of the magnetosheath than the other side depending on the direction of interplanetary magnetic field.

1.5 Objective and Outline of This Thesis

The objective of this thesis is to further study the properties of these slow-mode structures in the magnetosheath and to find mechanisms that generate these structures. The following is the outline of the thesis.

The satellite observations of the dayside magnetosheath and the corresponding solar wind conditions are analyzed in chapter 2. The observational results show that slow-mode variations with anti-correlated plasma density and magnetic field are

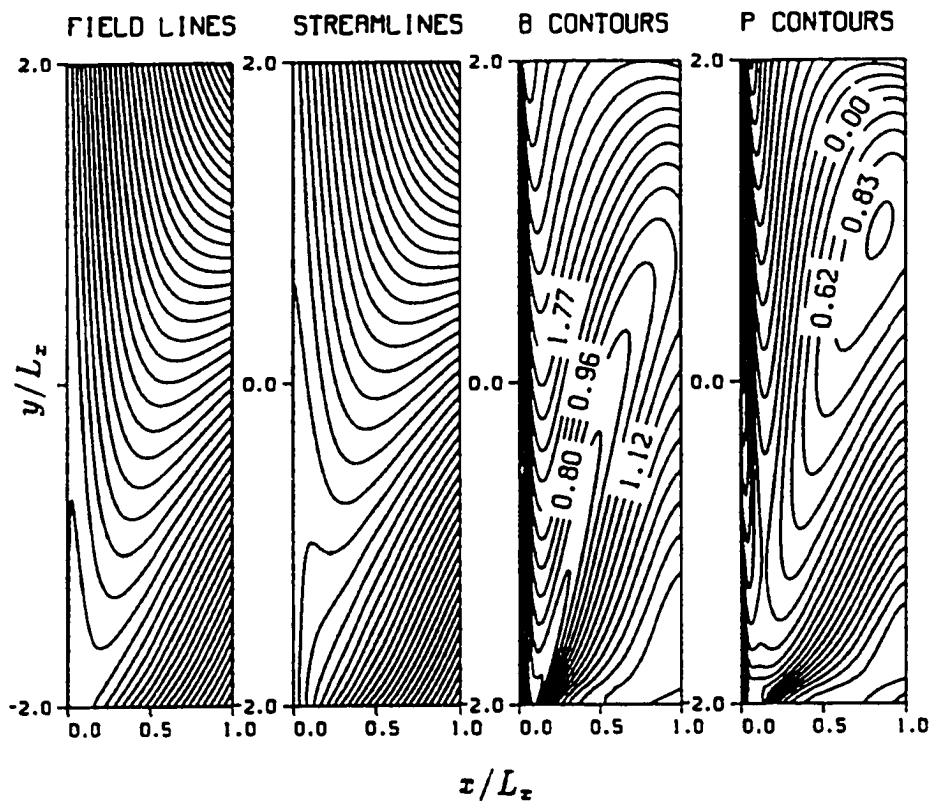

Figure 1.8 The magnetic field lines, streamlines, and contours of plasma density and amplitude of the magnetic field corresponding to the in the region close the the stagnation point [*Lee et al.*, 1991].

dominant in the dayside magnetosheath on time scales over 5 minutes. Some of density and magnetic field variations come from the solar wind. Some of the observed slow-mode structures with enhanced plasma density and depressed magnetic field in the magnetosheath correspond to Alfven-mode structures without variations in the plasma density and magnetic field strength in the solar wind.

Chapters 3 and 4 study the interactions between the bow shock and interplanetary fluctuations and waves generated through the interactions. Chapter 3 uses one-dimensional MHD simulations to study the bow shock interactions with interplanetary shocks, rotational discontinuities, and large-amplitude Alfven waves. The results show that the bow shock interaction with an incident rotational discontinuity results in a slow-mode structure with enhanced plasma density and depressed magnetic field downstream of the bow shock. The bow shock interaction with an incident shock also generates a slow shock and a slow-expansion wave in the magnetosheath. Further, chapter 4 uses two-dimensional MHD simulations to study the interaction processes as well as the propagation of the generated waves in the magnetosheath. The simulations show that the fluctuations in the plasma density associated with the slow-mode waves are amplified as they propagate from the bow shock to the magnetopause because of the decreased propagation speed in the direction normal to the magnetopause. The slow-mode waves generated in the interactions stay in the inner magnetosheath for about 15 minutes before the wave energy is convected tailward.

In chapter 5, the observational and simulation results are discussed and a summary is given. The study shows that the some of the slow-mode structures observed in the magnetosheath may be generated through interactions between the bow shock and fluctuations in the solar wind, and convected to the inner magnetosheath by the plasma flow.

Chapter 2 Observational Properties of Magnetosheath Large-Scale Fluctuations

2.1 Introduction

The slow-mode structures reported by *Song et al.* [1990; 1992] have the following observational properties. (a) The structures have an overall enhanced plasma density and depressed magnetic field. (b) The outer edge of the observed structures does not convect with the magnetosheath plasma flow; they seem to stand against the magnetosheath flow. (c) There are smaller scale fluctuations with anti-correlated plasma density and magnetic field in the slow-mode structure. (d) They are observed frequently in the inner magnetosheath. (e) The relative density enhancement in the structures increases with a decreasing plasma β value. (f) The wavelength λ_n in the direction normal to the magnetopause is typically 2000-6000 km while the wavelength λ_t in the tangential direction is much larger than λ_n. (g) The plasma density variations at the edges of the structure are steepened with shock-like profiles.

In this chapter we will further examine the data from satellite observations to study the properties of these slow-mode structures with emphasis on their solar wind sources. The data used in this study include those from the ISEE 2 magnetometer [*Russell et al.*, 1978] and fast plasma experiment (FPE) [*Bame et al.*, 1978]. To explore the sources of these magnetosheath fluctuations, solar wind plasma [*Bame et al.*, 1978] and magnetic field data [*Frandsen*, 1978] from ISEE 3 are compared with the magnetosheath observations.

In section 2.2, we study two representative cases in detail to demonstrate the properties of large-scale magnetosheath fluctuations and their sources in the solar wind. In section 2.3, we study two other example cases in which slow-mode structures with enhanced plasma density and depressed magnetic field are observed in the inner magnetosheath, while their sources are identified as Alfven waves in the solar wind. There are no variations in the solar wind plasma density or the amplitude of the magnetic field associated with these Alfven waves; only the direction of the magnetic field changes in these waves. In section 2.4, we select 51 complete magnetosheath crossing of ISEE 2 and show some statistical results for the location of the slow-mode structures in the magnetosheath. A summary is given in the final section of this chapter, section 2.5.

2.2 Examples of Large-Scale Fluctuations with Solar Wind Sources

2.2.1 Case 1: November 10, 1977

Figure 2.1 shows ISEE 2 data obtained during an outbound magnetosheath crossing from 2220 UT on November 10, 1977, to 0100 UT the next day. The top panels show the three components and the magnitude of the magnetic field in GSE coordinates, with a time resolution of 4 s. (GSE coordinates are used throughout this analysis of the satellite data.) The lower panels show the ion density, average ion temperature, and bulk flow velocity, all measured near the x-y plane, with a time resolution of 12 s. The satellite crossed the magnetopause for the last time at 2240 UT, which is indicated by a vertical dashed line in Figure 2.1. The magnetosheath is identified in comparison to the magnetosphere by higher ion

density, lower temperature, higher flow speed, and stronger fluctuations on both the magnetic field and the plasma parameters. For this case, the magnetic field in the magnetosheath immediately next to the magnetopause is slightly smaller than that in the magnetosphere. The GSE coordinates of ISEE 2 were (2.4, -9.4, 3.5) R_E at 2240 UT and (4.3, -11.4, 4.7) R_E at 0100 UT.

We will focus on the observations obtained between the magnetopause and the bow shock. There are continuous, strong fluctuations in the ion density in time scales greater than 5 minutes. To measure the large-scale variations and take the higher frequency variations out, we perform a 3 minutes avearge on the ISEE 2 data. The results are shown in Figure 2.2. As indicated by the shadings in Figures 2.1 and 2.2, the first plasma density enhancement is present from 2240 to 2248 UT, right next to the magnetopause in the magnetosheath. Note that it is the variations with time scales greater than 5 min that are under concern, the peaks with smaller durations shown in Figure 2.1 should be disregarded when measuring the maximum value. From Figure 2.2, it is found that the maximum value of the ion density is 46 cm^{-3} and the background value is about 37 cm^{-3}, the ion density enhancement relative to the background is 24%. The second ion density enhancement is observed in the 52 min time interval between 2248 and 2340 UT. The maximum value of the ion density is 62 cm^{-3}, and the background value is around 38 cm^{-3}. The relative ion density enhancement is 63%. The plasma density is enhanced for the third time in the 45 min interval between 2340 and 0025 UT. This time the ion density enhancement is smaller, with a peak value of 46 cm^{-3} and a background value of about 34 cm^{-3}. The relative enhancement is 35%. The fourth plasma density enhancement is seen between 0025 and 0058 UT. The ion density peak value is 47 cm^{-3} with the background value of about 34 cm^{-3}; The relative ion density enhancement is 38%. The strong ion density fluctuations observed over the larger time scales are observed all the way to the

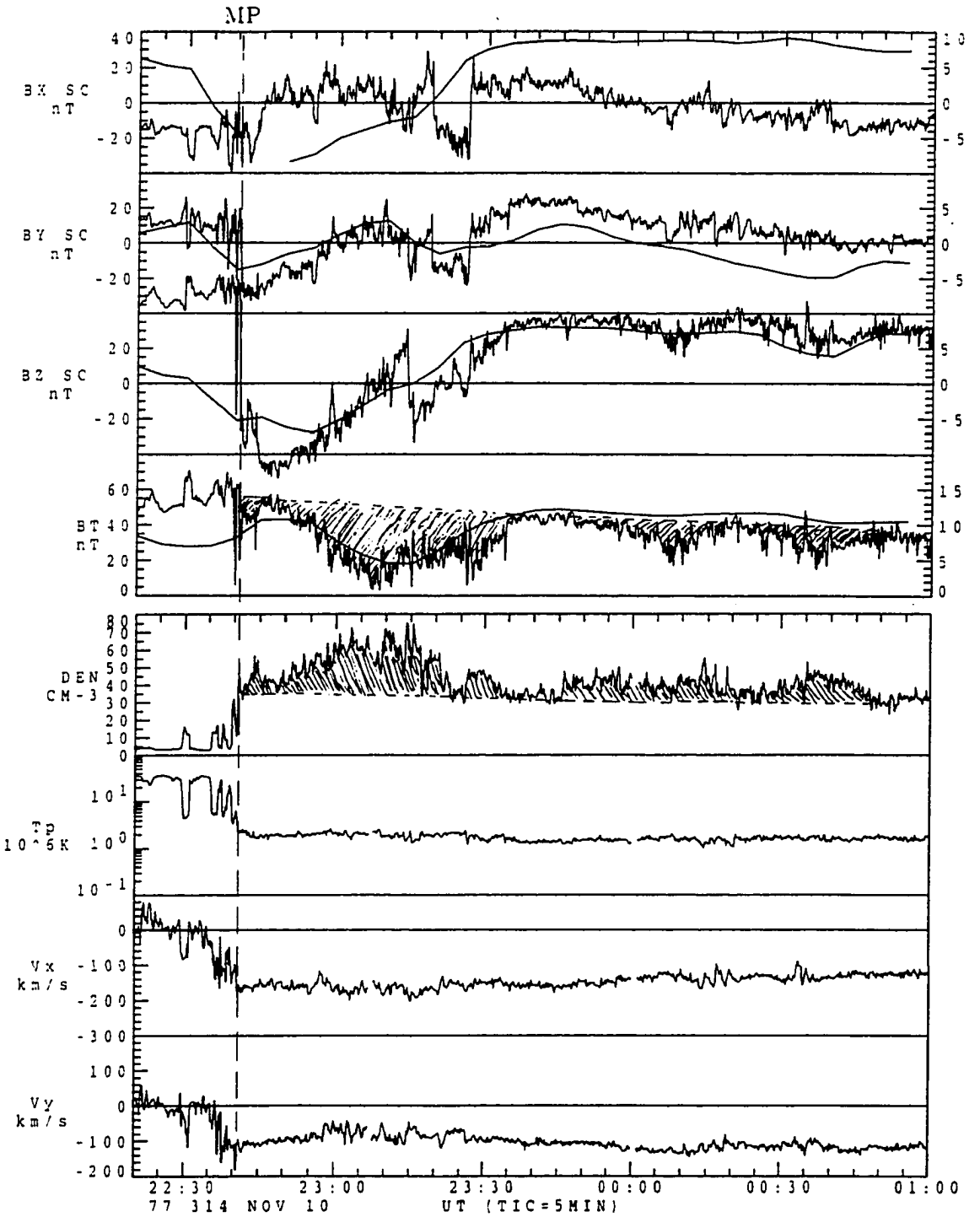

Figure 2.1 An outbound magnetosheath crossing by ISEE 2 and corresponding solar wind conditions observed by IMP 8. The magnetic field data has a resolution of 4s for ISEE 2 and 5 min for IMP 8. The plasma data has a resolution of 12s for ISEE 2.

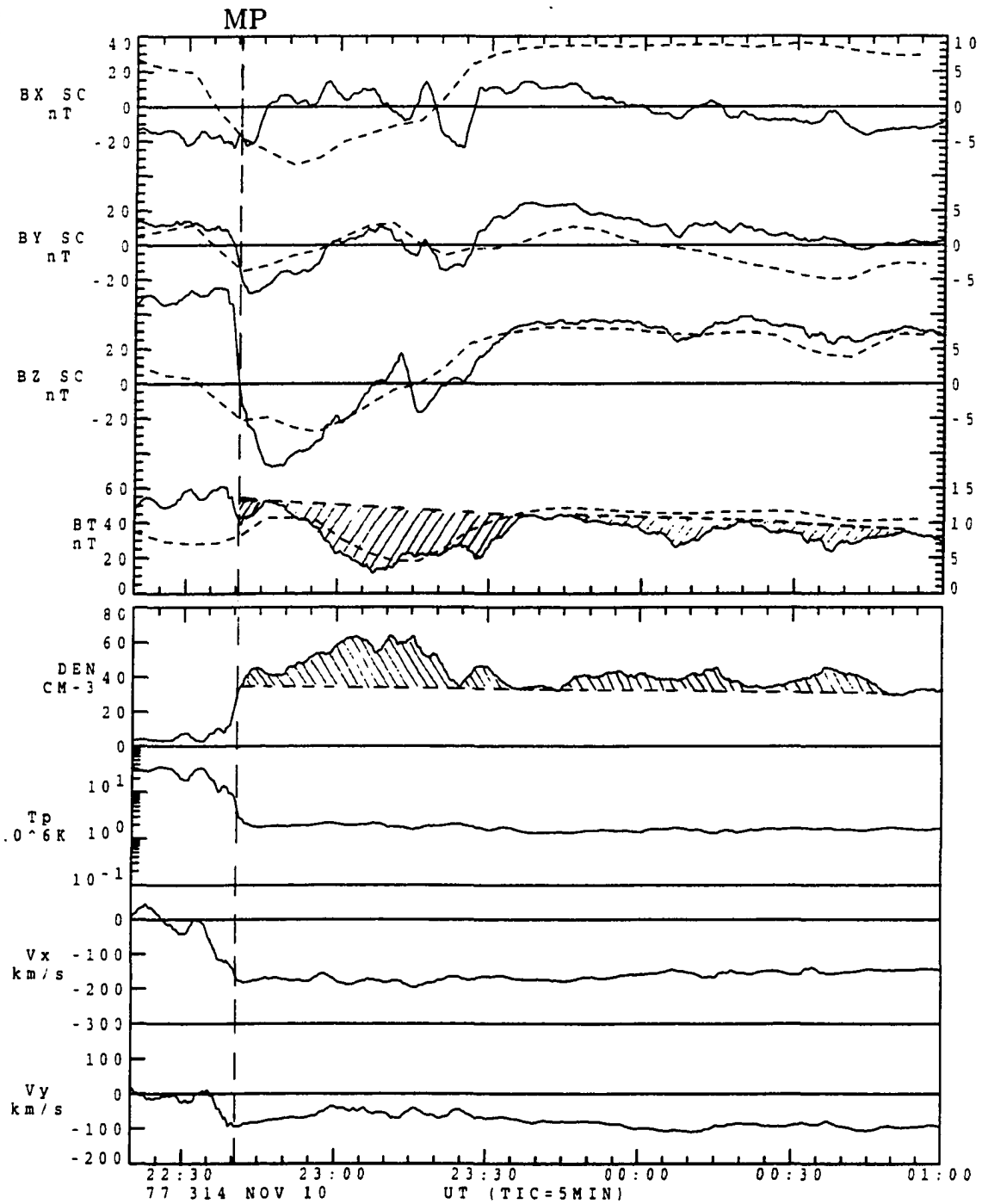

Figure 2.2 The same as Figure 2.1 except that the 3 min running average has been applied to the ISEE 2 data. The ISEE 2 data are shown by the solid lines and the IMP 8 data are shown by the dashed lines.

satellite's crossing of the bow shock at 0330 UT, which is not shown in Figures 2.1 and 2.2. The average ion temperature does not vary significantly during large-scale density variations.

Strong depressions of the magnetic field are observed simultaneously with the plasma density enhancements. The amplitude of the magnetic field decreases 19% from the background value of 54 to 44 nT during the first plasma density enhancement event. During the second density enhancement event, the magnetic field depression is around 75% from a background value of 48 nT. A 36% overall depression in the period of the third event is recorded. The background value is around 42 nT. A 30% depression from the background value of 35 nT is recorded during the fourth event. The magnetic field depression in the first event is also significant. This anti-correlation between the plasma density and the strength of the magnetic field is good for the first, second, and the fourth events. In the third event, the plasma density is overall enhanced and the magnetic field is overall depressed, but the anti-correlation is not as good as the the other events on the detail variations. The anti-correlation between the plasma density and the magnetic field amplitude indicates that all the evnets have slow-mode structures. Note that anti-correlations with smaller time scales also show up in the long-duration second event. For example, during the period from 2325 to 2335 UT, the ion density is enhanced and the magnetic field is depressed. The anti-correlation between the plasma density and the magnetic field continues after 0100 UT through the remainder of the passage through the magnetosheath, which is not shown in Figures 2.1 and 2.2.

The IMP-8 satellite was in the solar wind during the ISEE 2 magnetosheath crossing. Its position in GSE coordinates was (-11.1, -34.3, 2.8) R_E at 2240 UT and (-10.0, -35.0, 3.8) R_E at 0100 UT. The magnetic field data from IMP 8 are shown in Figure 2.1 and 2.2 at a time resolution of 5 minutes. The IMP 8 data

have been time-shifted 3 minutes ahead in order to match the two observations when the ISEE 2 was close to the magnetopause. Because of the ISEE 2's slow motion and variable solar wind speed, the match may not be good for other times in the magnetosheath crossing. There are significant magnetic field depressions in the solar wind that correspond to the magnetic field depressions of the first and second events observed in the magnetosheath. For the third and fourth events, the interplanetary magnetic field does exhibit weak depressions, but they are not nearly as strong as in the magnetosheath. The solar wind proton density is not shown in the Figures 2.1 and 2.2 since there is a large data gap during the period.

2.2.2 Case 2: September 12, 1978

Figure 2.3 shows observations for an outbound crossing of the magnetosheath by ISEE 2 on September 12, 1978. A running average with a window of 3 min and a resolution of 12 s has been applied to the magnetic field and plasma data of ISEE 2. The format is the same as that used in Figure 2.2. The satellite crossed the magnetopause for the last time at 1956 UT. Compared to the magnetosphere, the magnetosheath has a much higher plasma density, much lower temperature, much higher bulk flow speed, and a slightly weaker magnetic field. The satellite then crossed the bow shock about 10 minutes after the midnight. Compared to the solar wind upstream of the bow shock, the magnetosheath has a higher plasma density, higher temperature, stronger magnetic field, and lower bulk flow speed. The positions of the magnetopause and the bow shock are indicated by the vertical dashed lines in Figure 2.3. ISEE 2 was located at (8.6, 1.9, 3.9) R_E at 1956 UT and (14.1, 0.3, 5.6) R_E at 0010 UT, while ISEE 3 was positioned upstream of the bow shock at around (207,-68,18) R_E during the period of observation. Figure 2.3 also shows ISEE 3 observations of the magnetic field and ion density, at a time resolution of 5 minutes.

The average solar wind flow speed is 385 km/s during the period from 1900 to 2300 UT. The time required for the plasma to travel from ISEE 3 to ISEE 2 is estimated to be about 57 minutes. The actual time shift used in Figure 2.3 for the ISEE 3 observation is 56 minutes.

Three ion density enhancements with large time scales are observed in the magnetosheath. The first event is from 1957 to 2008 UT, shortly after the satellite crossed the magnetopause. The ion density peak value is 23 cm^{-3}, and the background value is 13 cm^{-3}, for a relative enhancement of 77%. The second event is from 2015 to 2102 UT, or a duration of 47 minutes. The peak value is 34 cm^{-3} with a background value of around 12 cm^{-3}. The density enhancement is 183%. The third event is between 2146 and 2217 UT (a duration of 32 minutes), with a maximum ion density of 30 cm^{-3} and a background value of 9 cm^{-3}. Its relative enhancement is 233%. The ion temperature is also enhanced in the third event, but with only a small amplitude. No significant variations are found in the ion temperature during the first and the second events. All three events have sharper edges than the events in Case 1. The three events are clearly separated from each other, which is also different from Case 1 where they are consecutive. The magnetic field is depressed during each plasma density enhancement. This is why they are called slow-mode structures. The suggestion of a fourth, weak event is seen in the data from 2230 to 2330 UT, where the ion density increases gradually while the magnetic field decreases gradually. This is also a slow-mode variation. Actually there exist fluctuations between the second and the third events, which also show anti-correlation between the plasma density and the magnetic field, but the magnetic field variation is marginal.

Corresponding to the plasma density enhancement events observed in the magnetosheath, there are similar signatures in the solar wind, as shown in Figure 2.3 by the dashed lines. The ion density is locally enhanced within the solar wind during

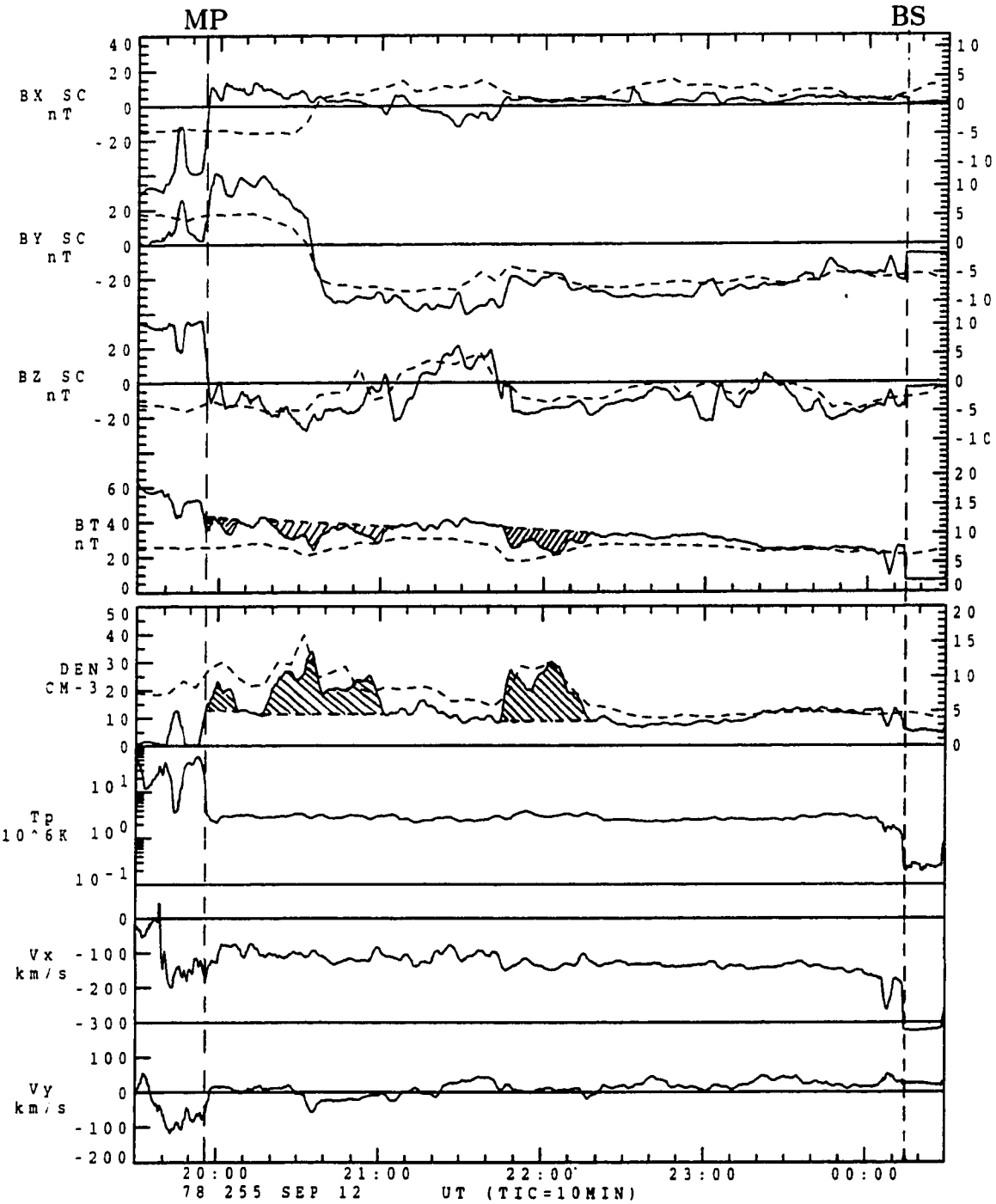

Figure 2.3 An outbound magnetosheath crossing by ISEE 2 (solid lines) and corresponding solar wind conditions observed by ISEE 3 (dashed lines).

the periods in which the three slow-mode events are seen in the magnetosheath. The edges of these ion density enhancements do not look as sharp as those observed in the magnetosheath due to the poor time resolution of the solar wind data. The higher density region of the second event does not appear as wide in the solar wind as observed in the magnetosheath. Note that there is a dramatic change in the IMF direction in the middle of the events. As this structure crosses the bow shock, the density enhancement region may be broadened because of the change in IMF direction as will show in the two example cases to follow. The solar wind magnetic field does decrease during the third event observed in the magnetosheath. The slow variations after the third event also have a similar weak signature in the solar wind. In this case, all the slow-mode structures seen in the magnetosheath can be matched with corresponding structures in the solar wind. However, the signatures observed in the magnetosheath deviate from the signatures observed in the solar wind significantly because of the modification by the bow shock.

2.3 Examples of Slow-Mode Fluctuations Associated with Alfven-Mode Structures in the Solar Wind

In this section, we study two example cases in which slow-mode structures with enhanced plasma density and depressed magnetic field are observed in the inner magnetosheath, and their sources are identified in the solar wind. They are different from the two previous examples, however, in that there are no variations in the plasma density or the amplitude of the magnetic field. The sources are variations on the direction of IMF.

2.3.1 Case 3: September 17, 1978

Figure 2.4 shows data obtained during an outbound crossing of the magnetosheath by ISEE 2 on September 17, 1978. The 3 min running average has been applied to the magnetic field and plasma data of ISEE 2. The format is the same as that used for Figure 2.3. The satellite crossed the outer edge of the magnetopause current layer at 1520 UT near 1103 LT and at about 23.5° (GSE). The position of the outer edge of the magnetopause current layer is indicated by the dashed line. The corresponding ISEE 3 observations for the magnetic field and the ion density in the solar wind are also shown in Figure 2.4. The ISEE 3 satellite was located at (211, -80, 17) R_E. The average solar wind flow speed was about 400 km/s in the period from 0730 UT to 0830 UT, giving a time delay between ISEE 2 and ISEE 3 observations of about 56 minutes. The actual time delay used in Figure 2.3 is 54 minutes. The time resolution of the ISEE 3 data is 5 minutes.

The single plasma density enhancement is seen from 1533 UT to 1610 UT; a duration of 37 minutes. The ion density has a peak value of 17 cm^{-3} and a background value of 10 cm^{-3}. The relative enhancement is 70%. The magnetic field is depressed for the same period of time. Because of the pile-up effect, the magnetic field tends to increase from the magnetosheath to the magnetopause. With this in mind, the depression of the magnetic field in the density enhanced area is more obvious. Some small structures are observed during the long period in which the ion density and the amplitude of magnetic field show very good large-scale anti-correlation. Magnetosheath plasma density remains low and steady after 1610 UT. The comparison between ISEE 1 and ISEE 2 observations by *Song et al.* [1992] shows that the slow-mode structure has a near zero propagation speed in the direction normal to the magnetopause [*Song et al.*, 1992]. There is no obvious plasma density variation in the solar wind during the corresponding period. There is no much variation in the magnitude of the magnetic field.

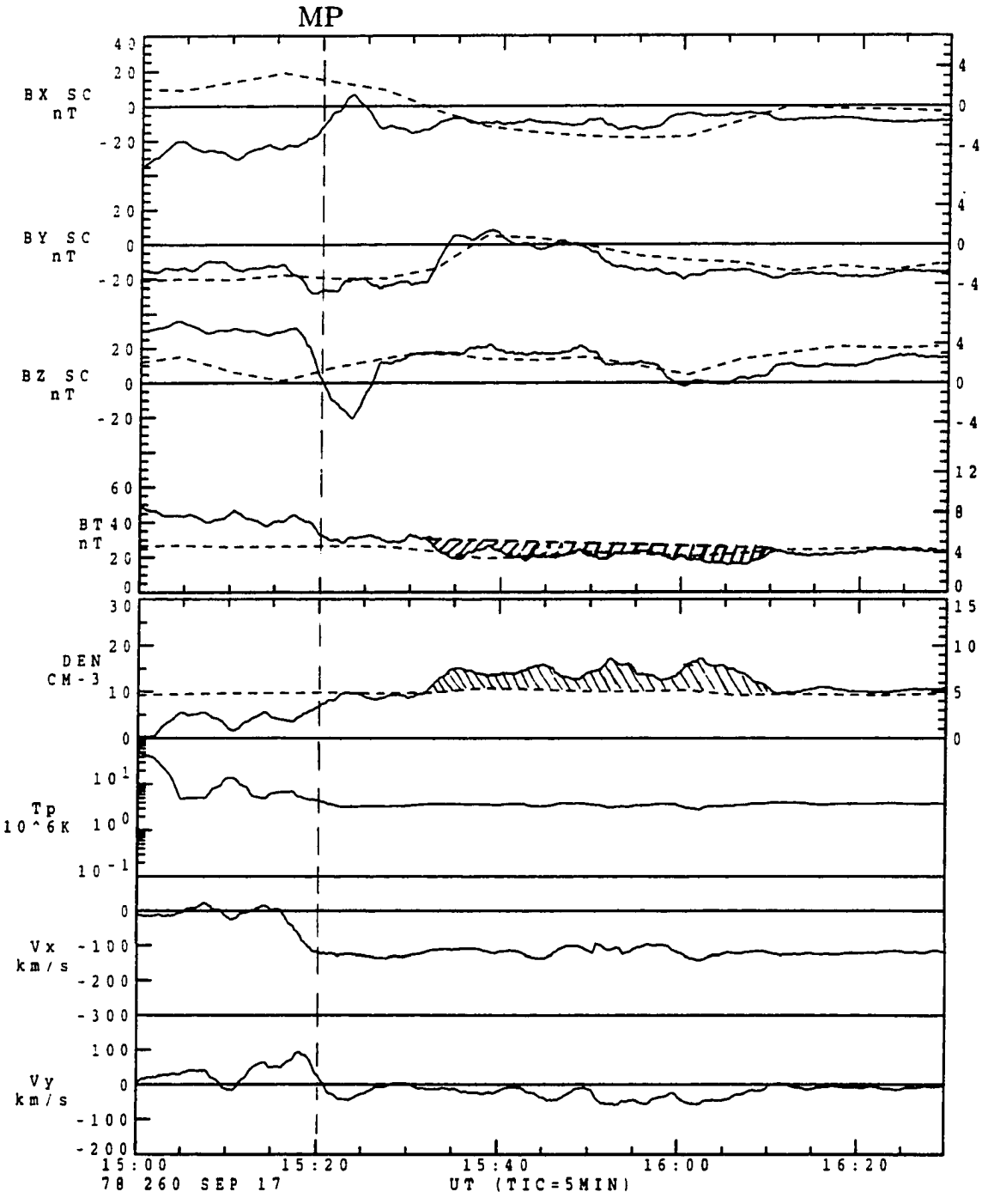

Figure 2.4 An outbound magnetosheath crossing by ISEE 2 (solid lines) and corresponding solar wind conditions observed by ISEE 3 (dashed lines).

However, at the leading edge of the slow-mode structure, there is a sharp change in the y component of the magnetic field. The magnetic field rotates by an angle of over 90^o at the leading edge of the slow-mode structure. Similar rotation also appears in the solar wind. Note the gradual variations in both the y and z components from 1533 UT to 1610 UT. No significant variations are observed in the direction of the magnetic field at the trailing edge of the region . The change in plasma density is steep at both edges, as is the amplitude of the magnetic field.

2.3.2 Case 4: August 22, 1978

Figure 2.5 shows the data obtained during outbound crossing of the magnetosheath by ISEE 2 on August 22, 1978. The 3 min running average has been applied to the ISEE 2 data. The format is the same as used in Figure 2.3. ISEE 2 satellite is in the magnetopause boundary layer from 0842 UT to 0900 UT. In the boundary layer, the plasma density is much higher than that in the magnetosphere and lower than that in the magnetosheath. The magnetic field transition from high values in the magnetosphere to lower values in the magnetosheath occurs at the outer edge of the boundary layer. ISEE 2 was located at (10.0, 2.2, 4.4) R_E at 0900 UT.

The ion density is enhanced in the region next to the magnetopause boundary layer. There are two peaks in the ion density, one at 0912 UT, the second peak at 0917 UT. They both have a maximum density value of 28 cm^{-3}. The ion density background is 17 cm^{-3} between the two peaks. The maximum relative density enhancement is 65%. The ion temperature is almost constant across the density enhancement region on the same time scale. The x component of the flow velocity is close to -100 km/s at the time the two peaks are seen in the ion density, and its amplitude increases to near zero between the two peaks. The y component of the bulk flow velocity is small throughout the density enhancement region on the same

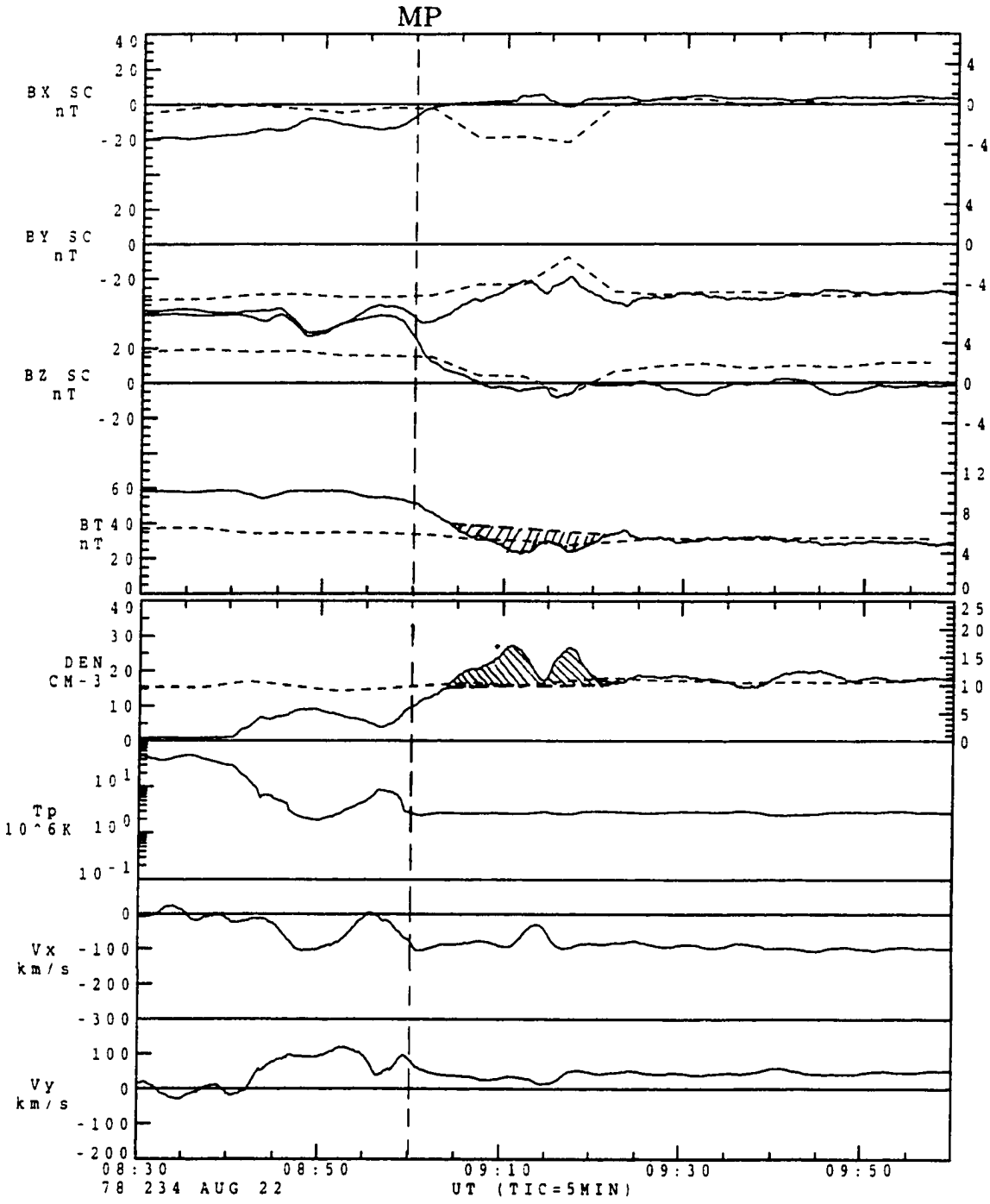

Figure 2.5 An outbound magnetosheath crossing by ISEE 2 (solid lines) and corresponding solar wind conditions observed by ISEE 3 (dashed lines).

time scale. Because of the magnetic field pile up effect in front of the magnetopause, the amplitude of the magnetic field should increase from the magnetosheath proper to the magnetopause. Taking this effect into account, the depression of the magnetic field is obvious in the same region of the density enhancement. Minimum are seen in the magnitude of the magnetic field at the times of the density enhancements. The anti-correlation between the plasma density and the magnetic field strength means they are slow-mode structures.

The magnetic field and ion density data from ISEE 3 are also shown in Figure 2.5 with a time resolution of 5 minutes. ISEE 3 was located around (135, -15, 14) R_E in the solar wind during the period. There are no variations in the ion density and the strength of the magnetic field. However, the y component of the magnetic field changes dramatically from -4 nT to 3 nT and then changes back to -5 nT. The x component of the magnetic field also changes strongly from -5 nT to 1 nT. The direction of the magnetic field rotates about 140^o and then rotates back. As in Case 3, the directional variation of the magnetic field in the solar wind may be responsible for the slow-mode structure with a density enhancement and magnetic field depression in the magnetosheath.

2.4 Statistical Results

In order to study how often the large-scale fluctuations appear in the magnetosheath. We selected 51 magnetosheath passes of ISEE 2 in the time period from October 27, 1977 to the Nov 21, 1979. Figure 2.6 shows the positions in GSE coordinates of the magnetopause crossings in the selected magnetosheath passes. In the Figure, $D = \sqrt{y^2 + z^2}$ is the distance normal to the x axis. The average magnetopause (thick line) and bow shock (thin line) positions obtained by *Farris et al.* [1991] are

also shown in the Figure. All 51 passes are in the dayside magnetosheath. Some of the crossings are close to the subsolar point while the others are far from the subsolar area. For this work it is required that the data for the passes have to include the crossings of both the magnetopause and the bow shock, and have no large data gaps during the passes.

A common feature in the magnetosheath is the frequent occurrence of the large-amplitude fluctuations of the plasma density and magnitude of the magnetic field with durations over 5 minutes. For this work, an "event" is defined as a plasma density enhancement that increases from its background value by 50% or more for more than 5 minutes. When we measure the maximum density enhancement for a event, the small peaks with duriations smaller than 5 min are disregarded as what we do for the four example cases as described previously. Under this definition, a total of 122 events were found in the 51 magnetosheath crossings: Each crossings has an average of 2.4 events. One of the important properties of these large-scale fluctuations is that the majority of these large scale fluctuations are slow mode structures, which means that the variations of the plasma density and the strength of the magnetic field are anti-correlated. Among the 122 events, only 3 (2% of the total) events are fast-mode events with enhancements both in the plasma density and the magnetic field. The other 119 events are all slow-mode structures. Among the 119 slow-mode events, 42 events (35%) have density enhancements relative to the background value of over 100%. The relative density enhancement is between 50% and 100% in the remaining 77 events (65%).

In Figure 2.7, the magnetosheath is divided evenly into three regions . From the magnetopause side to the bow shock side, they are defined as the inner, middle, and outer magnetosheath. It is impossible to be absolutely sure about the position of an observed slow-mode event in the magnetosheath relative to magnetopause or the bow

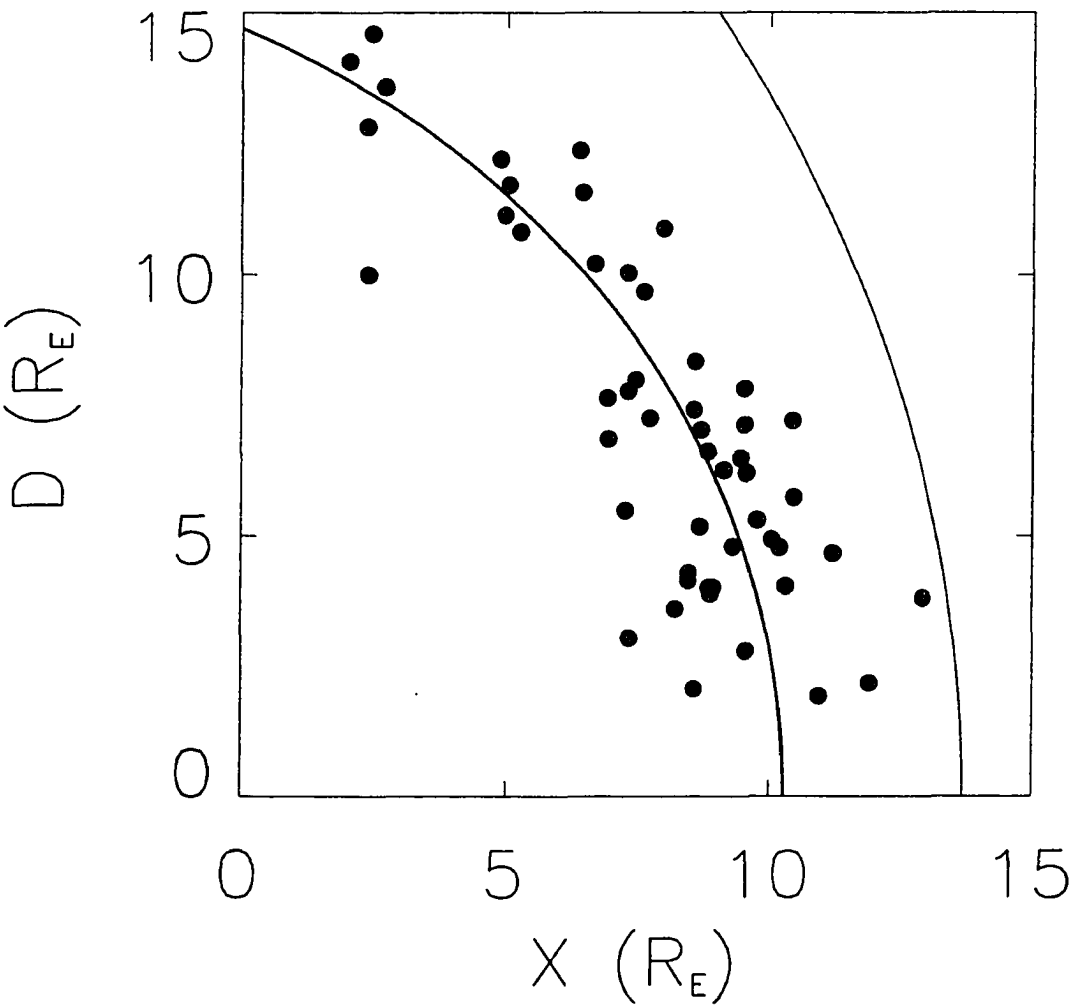

Figure 2.6 The locations in the GSE coordinate of the magnetopause crossings that correspond to the 51 selected complete magnetosheath crossings, and average magnetopause (thick line) and bow shock (thin line) positions obtained by *Farris et al.* [1991]. The distance to the x axis $D = \sqrt{y^2 + z^2}$.

shock since it requires the positions of the magnetopause, the bow shock, and the observed events at the same time. We assume that the positions of the magnetopause and the bow shock do not change much during the magnetosheath crossing. Therefore we can use the time separation between the observed events and the magnetopause or the bow shock to decide which region of the magnetosheath it is in. From the outer to the middle magnetosheath, the number of the observed events increases slightly from 16 to 24. However, a total of 79 events is found in the inner magnetosheath, corresponding to 66% of the slow-mode events found in the whole magnetosheath.

It should be noted that large-scale fluctuations with smaller plasma density variations are even more frequently observed in the inner magnetosheath. We found that anti-correlation between the plasma density and magnetic field magnitude is their characteric property. However, it is more difficult to make a reliable statistic for these weak fluctuations, which will be an important work in the future.

2.5 Summary

In summary, the following results are obtained through case studies and the statistical study of 51 magnetosheath passes.

(1) Fluctuations with time scales over 5 minutes frequently appear in the magnetosheath. A majority of large scale fluctuations are associated with an anti-correlated plasma density and magnetic field, indicating that they are slow-mode structures. These slow-mode fluctuations are more frequently observed in the inner magnetosheath close to the magnetopause.

(2) Some of the slow-mode fluctuations observed in the magnetosheath have their sources in the solar wind. However modifications at the bow shock make the signatures in the magnetosheath and the solar wind quite different at times. We

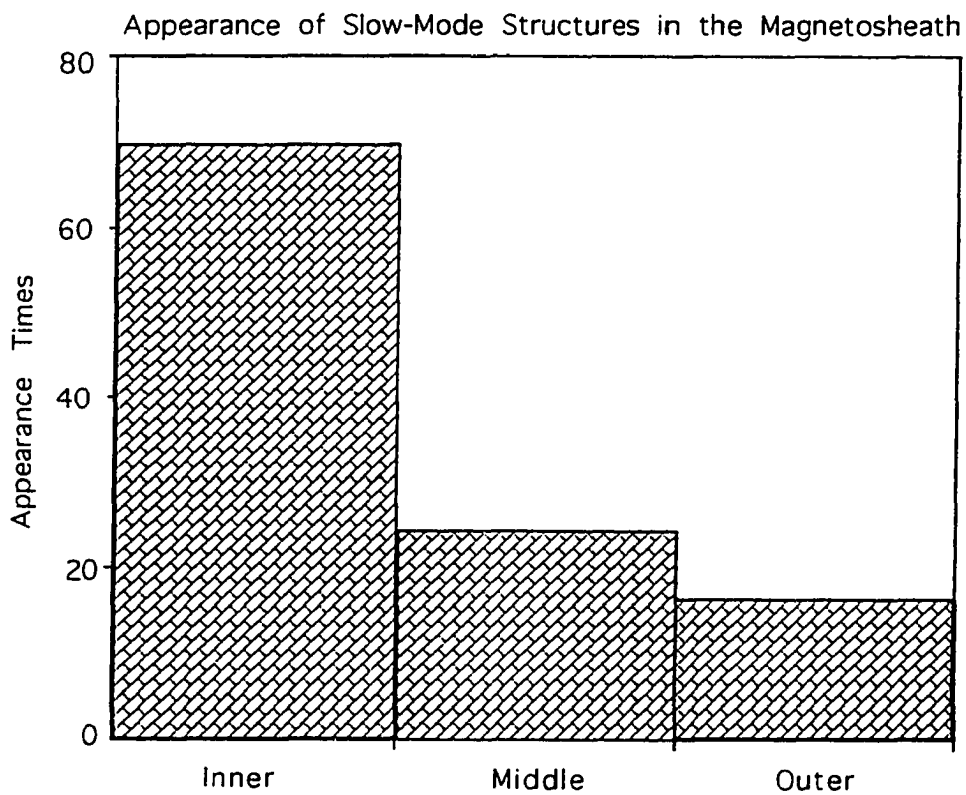

Figure 2.7 Number of large-scale slow-mode events as a function of the relative positions in the magnetosheath. The whole magnetosheath is evenly divided into three regions which are the inner, middle, and outer magnetosheath.

also notice that some of the slow-mode fluctuations in the inner magnetosheath, as reported previously by *Song et al.* [1990; 1992], are not proceeded by fluctuations in the solar wind. It is possible that they are generated locally at the magnetopause.

(3) Some of the slow-mode fluctuations with an enhanced plasma density and a depressed magnetic field observed in the inner magnetosheath correspond to Alfven-mode waves in the solar wind. Smaller-scale fluctuations with anti-correlated plasma density and magnetic field are found in these large-scale structures. For Alfven waves in the solar wind, plasma density and the magnitude of the IMF do not vary significantly, but the IMF direction changes.

Chapter 3 Interaction of Interplanetary Shocks and Rotational Discontinuities with the Bow Shock

3.1 Introduction

Most of the shocks observed in the interplanetary space are fast-mode shocks [*Hundhausen*, 1972; *Siscoe*, 1968]. Some of them propagate from the Sun outward in the solar wind frame. They are called forward fast shocks. The others are called reverse fast shocks because they propagate towards the Sun in the solar wind frame. A few slow-mode shocks are also identified in the interplanetary space [*Chao and Olbert*, 1970] and at least one of them is identified as a reverse slow shock [*Burlaga and Chao*, 1970]. The dynamic pressure can increase by a factor of 20 across solar wind shocks, but a factor of 3 are more common [*Siscoe*, 1968]. Rotational discontinuities arrive as frequently as every several minutes to several hours. There is usually no dynamic pressure variation associated with these rotational discontinuities. Observationally, there is no difference between a rotational discontinuity and a large-amplitude Alfven wave except that the thickness of the transition layer is small in a rotational discontinuity. About half of the time, Alfven waves are the main micro-structures of the solar wind [*Belcher and Davis*, 1971].

The bow shock's interaction with interplanetary shocks has been studied mainly by gas-dynamic theory [*e. g., Shen and Dryer*, 1972; *Dryer*, 1973]. Some MHD theories are only for perpendicular shocks [*e.g. Volk and Auer*, 1974; *Whang*, 1991].

Wu et al. [1993] studied the interaction between the bow shock and interplanetary tangential discontinuities. They found that the solar wind dynamic pressure jump carried by the tangential discontinuity is modified and energy is redistributed with an additional fast shock or fast expansion wave. Both the newly excited fast shock or fast expansion wave and the transmitted tangential discontinuity carry a strong pressure variations that may interact with the magnetosphere as pressure pulses [*Sibeck et al.*, 1989; *Sibeck*, 1990].

On the other hand, the study of the bow shock interaction with incident MHD waves has a history of more than 25 years [*Barnes*, 1970; *Mariani et al.*, 1970; *Fairfield and Ness*, 1970]. The linear theory about bow shock interactions with small amplitude Alfven waves in the solar wind was given by *Mckenzie and Westphal* [1969]. Because of their linear assumption, the results show that only a pair of Alfven waves is generated after an incident Alfven wave crosses the bow shock. As we will see in section 3.5 of this paper, when the nonlinear effects are included a pair of compressional slow-mode waves are also generated in addition to the Alfven waves.

In this Chapter, we systematically study the interaction of the bow shock with interplanetary shocks through one-dimensional simulations. The interplanetary shocks include forward fast shocks, reverse fast shocks, forward slow shocks, and reverse slow shocks. The magnetic field can be in any direction. The simulation model is briefly described in Section 3.2. We will see in Sections 3.3 and 3.4 that a slow shock and a slow expansion wave are generated downstream of the bow shock in addition to the fast shock or fast expansion wave and the contact discontinuity. The parameter dependence of the generated shocks and expansion waves will also be given in Sections 3.3 and 3.4. In Section 3.5, the bow shock interaction with interplanetary rotational discontinuities and large-amplitude Alfven waves will be studied. The main products of the interaction include an intermediate shock and a pair of slow shocks. A

summary of the simulation results will be given in Section 3.6. The results can be used to explain the generation of slow-mode waves observed in the inner magnetosheath.

3.2 One-Dimensional Simulation Model

Our simulations are based on the following complete set of MHD equations

$$\frac{\partial \rho}{\partial t} = -\nabla \cdot (\rho \mathbf{v}) \tag{3.1}$$

$$\frac{\partial (\rho \mathbf{v})}{\partial t} = -\nabla \cdot \left[(\rho \mathbf{v}\mathbf{v}) + \left(p + \frac{B^2}{2} \right) \mathbf{I} - \mathbf{B}\mathbf{B} \right] \tag{3.2}$$

$$\frac{\partial \mathbf{B}}{\partial t} = \nabla \times (\mathbf{v} \times \mathbf{B}) \tag{3.3}$$

$$\frac{\partial \epsilon}{\partial t} = -\nabla \cdot \mathbf{S} \tag{3.4}$$

The energy flux $\mathbf{S}$ and the energy density ϵ are defined as

$$\mathbf{S} = \left(\epsilon + p + \frac{B^2}{2} \right) \mathbf{v} - (\mathbf{B} \cdot \mathbf{v}) \mathbf{B} + \eta \mathbf{j} \times \mathbf{B} \tag{3.5}$$

$$\epsilon = \frac{1}{2} \rho v^2 + \frac{B^2}{2} + \frac{p}{\gamma - 1} \tag{3.6}$$

where the current density $\mathbf{j}$ is given by

$$\mathbf{j} = \nabla \times \mathbf{B} \tag{3.7}$$

In one-dimensional (1-D) simulations we set $\partial/\partial y = \partial/\partial z = 0$ and let the x component of the magnetic field B_x to be a constant. The simulations are carried out in the domain $0 \leq x \leq L$.

In Equation 3.1-3.7, all physical quantities are normalized. The length is normalized by the length of the simulation domain L, the magnetic field $\mathbf{B}$ is normalized by the initial magnetic field B_0 and the plasma density ρ is normalized by

the initial density ρ_0 just upstream of the bow shock. The velocity v, time t, current density J, pressure P, and temperature T are normalized by $V_A \equiv B_0/\sqrt{\mu_0\rho_0}$, $t_A = L/V_A$, $B_0/\mu_0 L$, B_0^2/μ_0, and $\mu_0 V_A L$, respectively, where μ_0 is the permeability of free space.

Initially, a steady bow shock is located at $x = x_1$ and the incident shock is located at $x = x_2$. Since the solar wind flows in the negative x direction, the incident shock also moves in the negative x direction. The bow shock and the incident interplanetary shock divide the whole simulation domain into three uniform regions: (1) the magnetosheath region ($0 \leq x \leq x_1$), (2) the solar wind region between the bow shock and the incident shock or rotational discontinuity ($x_1 < x < x_2$), and (3) the solar wind region upstream from the incident shock or rotational discontinuity ($x_2 \leq x \leq L$). The Rankine-Hugoniot jump conditions shown in Equations 1.1-1.6 are applied to determine the upstream and downstream conditions for both the bow shock and the interplanetary shock or rotational discontinuity. The incident shock or rotational discontinuity may propagate in the positive or negative x direction in the plasma frame. Because of the super-fast flow of the solar wind, they all move in the negative x direction towards Earth. For the cases with incident shocks, the initial configuration is completely determined by four parameters: the Alfven Mach number M_A which is the solar wind flow speed over the Alfven speed, the magnetic cone angle θ which is the angle between the magnetic field and the x axis, the plasma β which is defined as the ratio of the plasma pressure to the magnetic pressure, and the incoming shock strength r which is defined as the ratio of plasma density downstream of incident shock to the upstream density. The first three parameters are defined in region 2 between the bow shock and the incident interplanetary shock. The fourth parameter is replaced by a rotational angle $\Delta\phi$ of the magnetic field for the incident

rotational discontinuity. Free boundary conditions ($\partial/\partial x = 0$) are applied to both ends ($x = 0$ and $x = L$) of the simulation domain.

A total of 2000 grid points are used over the simulation domain. A Runge-Kutta scheme with a fourth-order accuracy in time and a second order accuracy in space is used to integrate the above MHD equations with time. Small diffusion terms are added to stablize the calculation. The diffusion terms determine the thickness of the transition layers of the shocks or expansion waves. This study concentrates on the products of the bow shock interaction with the interplanetary shocks or rotational discontinuities, the upstream and downstream values of each of these products. The diffusion term will only change the thickness of the transition layer but not the upstream and downstream values of the products. However, in this study, we make the diffusion terms as small as possible, and at least 5 grid points are located in each of the transition layers of the shocks and discontinuities.

3.3 Incident Fast Shocks

3.3.1 Forward Fast Shock

Figure 3.1 shows the spatial profiles of plasma density ρ, pressure P, and magnetic pressure P_B at times t =0, 0.11, and 0.22 for a case with an incident forward fast shock. Initially the bow shock is located at $x = 0.85$. From its upstream (right) side to downstream (left) side, the plasma density, plasma pressure, and magnetic pressure all increase. In the plasma frame, the bow shock is propagating away from the Earth. This propagation speed is balanced by the solar wind flow towards the Earth. As a result the bow shock is steady in the simulation frame. The

incident forward fast shock is propagating towards the Earth in the plasma frame. For the specific case shown in Figure 3.1, the parameters are chosen as $M_A = 7, \theta = 45^o$, $\beta = 1$, and $r = 2$, which are typical for the bow shock and the solar wind.

As the incident fast shock crosses the bow shock, a series of shocks, expansion waves, and discontinuities are generated downstream of the bow shock. From left to the right there are a fast shock, a slow expansion wave, a contact discontinuity, and a slow shock. In the plasma frame, the fast shock and slow expansion wave propagate away from the bow shock towards the magnetopause, the slow shock propagates towards the bow shock, and the contact discontinuity does not propagate. Because the plasma flow speed in the x direction downstream of the bow shock is locally below the fast-mode phase speed and over the slow-mode phase speed, all the generated waves are actually moving towards the magnetopause. In the plot for $t = 0.11$, the dashed lines indicate the positions of the generated fast shock (FS), slow expansion wave (SE), contact discontinuity (CD), and slow shock (SS). Plasma density, pressure, and magnetic pressure all increase across the fast shock. In the plot for $t = 0.22$, the dashed lines indicate the positions of the generated slow expansion wave (SE), contact discontinuity (CD), and slow shock (SS). The fast shock has propagated across the $x = 0$ boundary. The slow expansion wave is located at $x = 0.06$. From the upstream (left) to the downstream (right) of the slow expansion wave, the plasma density and pressure decrease and the magnetic pressure increases. The slow shock is located at $x = 0.18$. From the upstream (right) to the downstream (right) of the slow shock, plasma density and pressure increase and the magnetic pressure decreases. The contact discontinuity is located between the slow expansion wave and the slow shock at $x = 0.12$. Across the contact discontinuity from the magnetopause side to the bow shock side, the plasma density increases and the corresponding temperature decreases, while the plasma pressure, flow velocity, and magnetic field keep unchanged. As the

incident fast shock crosses the bow shock, the dynamic pressure upstream of the bow shock increases. As a result, the bow shock is modified and moves towards Earth. It can be seen from Figure 3.1 that the density variation is strong at the generated fast shock and the contact discontinuity and relatively weak at the slow expansion wave and the slow shock. But the magnetic field variation associated with the slow expansion wave or the slow shock as well as the fast shock is significant. Since the magnetic field and the plasma flow velocity are both in the x-y plane, the z components of the magnetic field and flow velocity are not involved in the interaction between the bow shock the incident shock, and no Alfven wave is generated.

The question how to determine the upstream and downstream of a shock or expansion wave is important. Suppose there is an object (shock, expansion wave, discontinuity). It can be moving. If the fluid flows from its right-hand side to left-hand side, the right-hand side is called upstream and the left-hand side is called downstream. The basic way to determine the upstream and downstream side of a shock is to measure the shock speed and the flow speeds at the two sides. There is an easier way to do the job in simulation cases of this chapter. Taking Figure 3.1 as an example, after the interaction, we know that the fast shock and the slow expansion wave propagate in the negative x direction while the bow shock and the slow shock propagate in the positive x direction in the plasma frame. Therefore, the left-hand side is the upstream for the fast shock and the slow expansion wave, and the right-hand side is the upstream for the bow shock and slow shock. The contact discontinuity moves with the plasma flow. Its propagation speed is zero in the plasma frame. There is no upstream or downstream for the contact discontinuity.

Figure 3.2 shows spatial distribution of the dynamic pressure $P_v = \rho v^2$ based on the total flow velocity and total pressure $P_T = P + P_B$ at time $t = 0.11$. Initially, the dynamic pressure decreases and the total pressure increases across the bow shock,

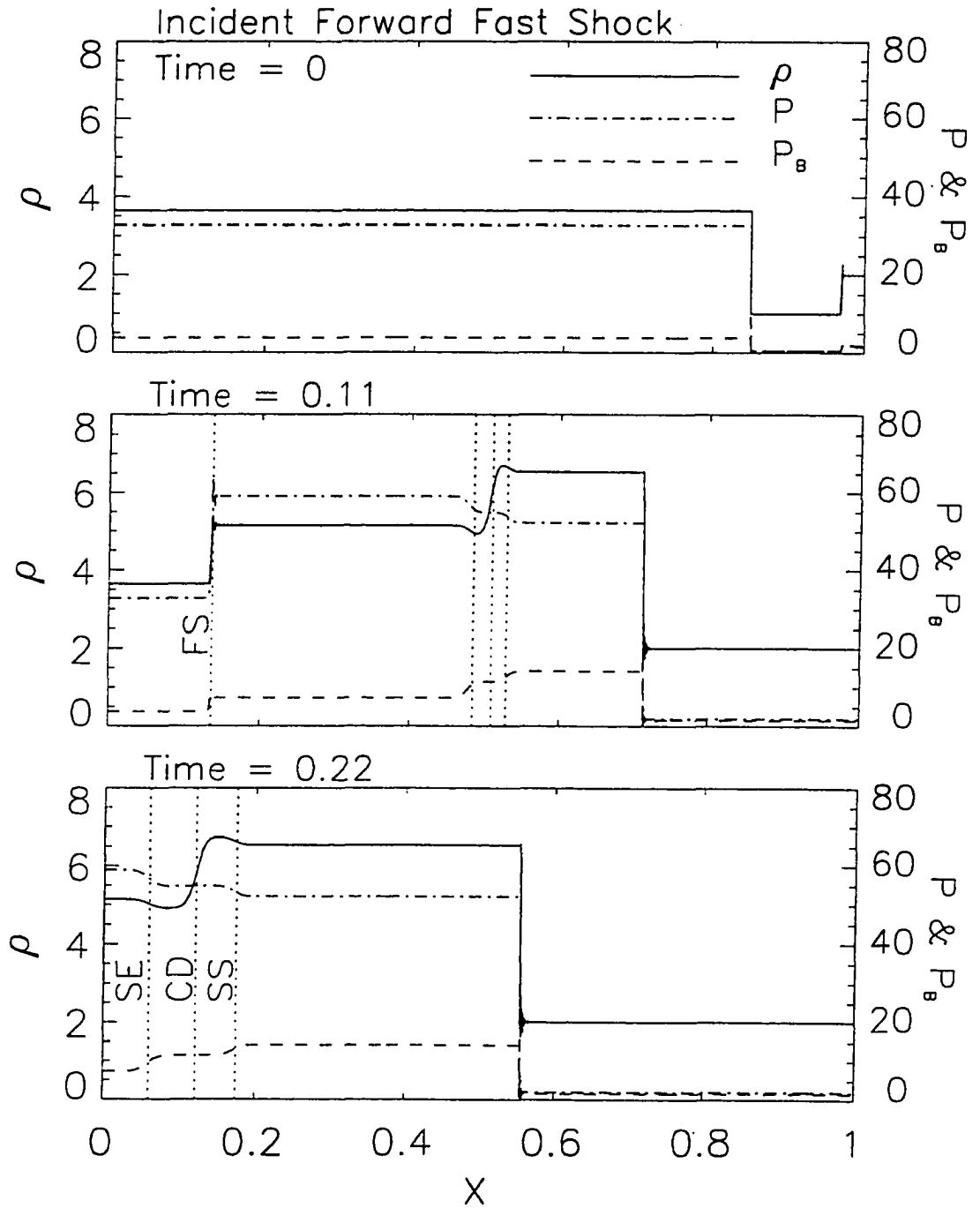

Figure 3.1 Spatial profiles of the plasma density ρ, pressure P, and magnetic pressure P_B at times t =0, 0.11, and 0.22 for a case with an incident forward fast shock. The parameters chosen are $M_A = 7$, $\theta = 45°$, $\beta = 1$, and $r = 2$.

but the summation of the two is constant. The dynamic pressure jump at the incident fast shock is 82. After the interaction, most of the dynamic pressure is carried by the fast shock. The dynamic pressure jump is about 50 and the total pressure jump is about 20. The total pressure is constant at the slow expansion wave, slow shock, and contact discontinuity. Dynamic pressure increases for about 15 at the contact discontinuity, but decreases slightly at the slow expansion wave and the slow shock from the magnetopause side to the bow shock side. Strictly, the dynamic pressure associated with the incident shock is distributed to all the waves generated through the interaction. But the fast shock carries most (85%) of it. The contact discontinuity also carries significant part (18%).

After interaction, the domain downstream of the bow shock is divided into 5 uniform regions. From left to right, they are region 1 (undisturbed magnetosheath), region 2 (between the fast shock and the slow expansion wave), region 3 (between the slow expansion wave and the contact discontinuity), region 4 (between the contact discontinuity and the slow shock), and region 5 (between the slow shock and the bow shock). Figure 3.3 shows the values of plasma density, pressure, and magnetic pressure in the five uniform regions after the shock-shock interaction as functions of the solar wind Alfven Mach number M_A for $\theta = 45^o$, $\beta = 1$, and $r = 2$. Note that the solar wind Alfven Mach number has a wide range with a most probable value of 7 [*Fairfield*, 1971]. The difference between the dotted line and the solid line is the jump at the fast shock. The density jump across the fast shock is not sensitive to the Alfven Mach number M_A. Because the plasma density just upstream of the fast shock becomes smaller as M_A increases, the relative jump of the plasma density becomes larger. The relative jump is defined as the ratio between the increment or decrement and the background value. The relative jump is 82% when $M_A = 2$ and 38% when $M_A = 10$. The pressure jump decreases with decreasing value of M_A,

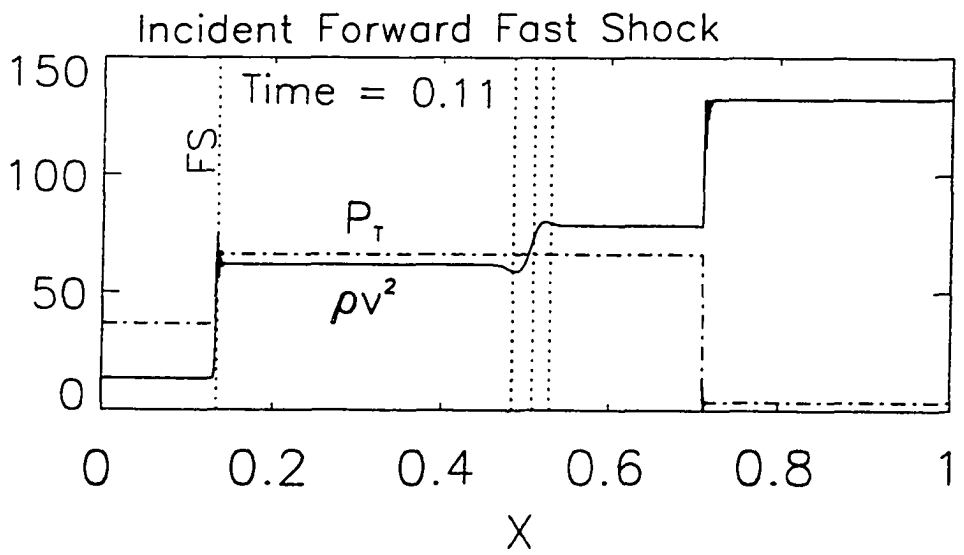

Figure 3.2 Spatial profiles of the dynamic pressure $P_r = \rho v^2$, and the total pressure $P_T = P + P_B$ at time 0.11 for the case in Figure 3.1.

but its relative jump increases with decreasing M_A. The relative jump of the plasma pressure is 206% when $M_A = 2$ and 74% when $M_A = 10$. The relative jump of magnetic pressure is 210% at $M_A = 2$. and 83% at $M_A = 10$. The difference between the dashed line and the dot-dashed line is the plasma density variation at the contact discontinuity. The two lines cross each other around $M_A = 3$, indicating that the density increases from the magnetopause side to the bow shock side of the contact discontinuity when $M_A > 3$ and decreases when $M_A < 3$. When $M_A = 10$, the relative increment is 46%. The difference between region 3 and region 2 gives the variations across the slow expansion wave. The maximum density decrement is about 10% which occurs at around $M_A = 4$. The density variation and the pressure variation are both small for all the M_A values in the chosen parameter domain. The difference between region 4 and 5 gives the jump at the slow shock. Note that when $M_A > 3.5$ the plasma density and pressure in region 4 become larger than those in region 5, while the magnetic pressure becomes smaller. When $M_A < 3.5$, the plasma density and pressure in region 4 are smaller than those in region 5 and magnetic pressure is larger. This means that the slow shock in the section $M_A > 3.5$ becomes a slow expansion wave when $M_A < 3.5$. The density and pressure variations at the slow shock or the slow expansion wave are small. But the variation of the magnetic pressure is significant at the slow shock and the slow expansion wave. The larger the value of M_A, the larger the jump in the magnetic pressure.

The strength of observed interplanetary shocks are generally smaller than that of the bow shock. Figure 3.4 shows the values of the plasma density, pressure, and magnetic pressure in the five regions as functions of the incident shock strength for $M_A = 7$, $\theta = 45°$, and $\beta = 1$. At the fast shock, the relative increment of the plasma density is 12% at $r = 1.3$, and increases to 86% at $r = 3$. The relative increment of the plasma pressure is 22% at $r = 1.3$ and increases to 209% at $r = 3$. The

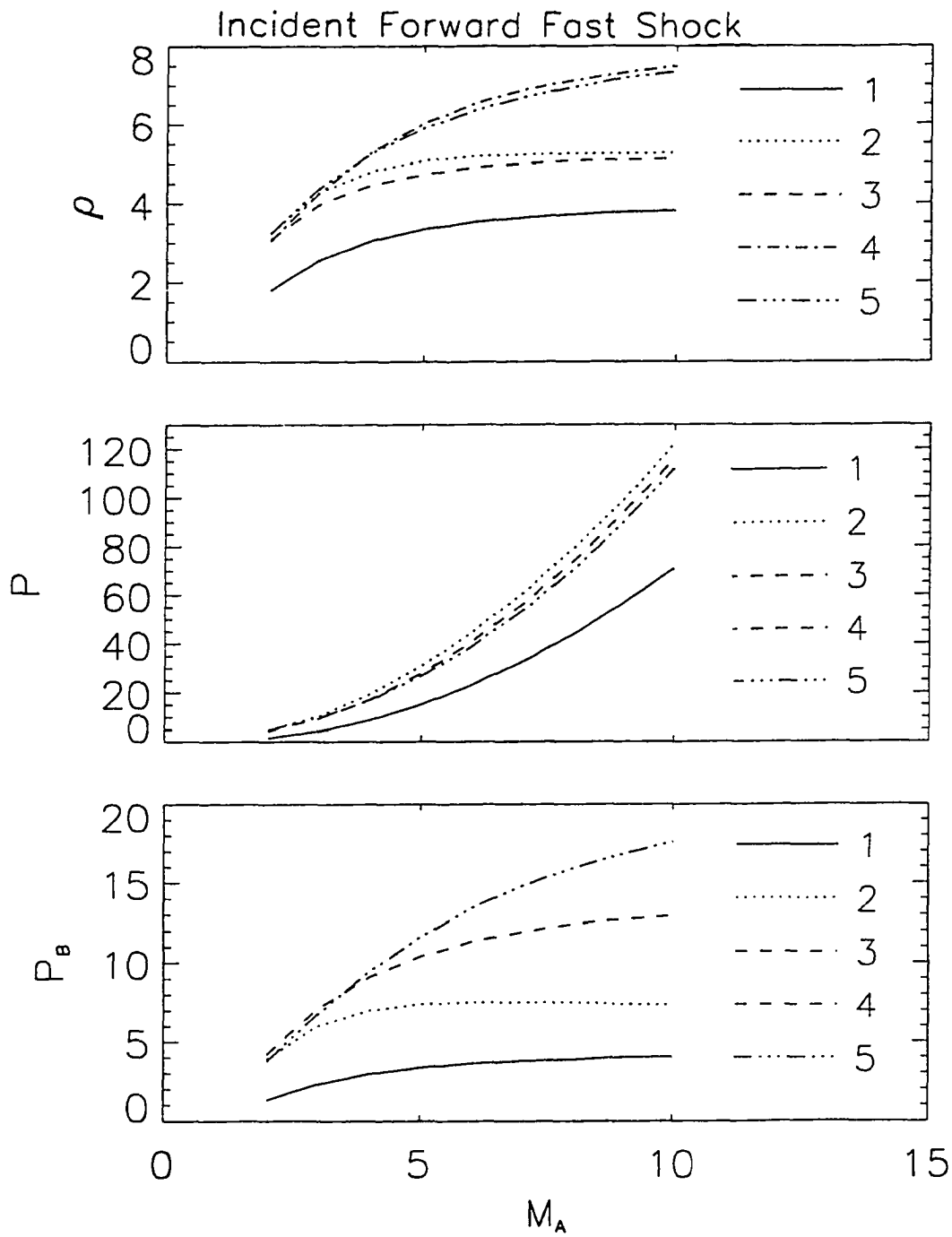

Figure 3.3 Plasma density ρ, pressure P, and magnetic pressure P_B in the five uniform regions after the interaction as functions of the Alfven Mach number M_A, given $\theta = 45^o$, $\beta = 1$, and $r = 2$.

magnetic pressure increment is 25% at $r = 1.3$ and 221% at $r = 3$. For the contact discontinuity, the density increment from the magnetopause side to the bow shock side is 14% at $r = 1.3$ and 36% at $r = 3$. The stronger the incoming shock, the stronger the generated fast shock and the contact discontinuity. The plasma density and pressure variations at the slow expansion wave or the slow shock are again small for all the incident shock strength in the chosen parameter domain. The magnetic pressure variations at the slow expansion wave and the slow shock are significant.

The strengths of the generated shocks, expansion waves, and discontinuities also depend on the other parameters β and θ. The slow shock and the slow expansion wave are found to have a larger relative jump in plasma density and thermal pressure for lower β. The lower the plasma β, the larger the density jump at the contact discontinuity. The θ dependence of the strengths are found to be weak from the simulations. However, the slow shock and the slow expansion wave disappear for the cases with $\theta = 0$ or $\theta = 90^{o}$. The same results hold for the cases with incident reverse fast shocks or slow shocks, which will not be repeated in the following sections.

3.3.2 Reverse Fast Shock

Figure 3.5 shows the spatial distributions of plasma density, pressure, and magnetic pressure at times t =0 and 0.23 for a case with an incident reverse fast shock which propagates towards the Sun in the plasma frame. Initially the bow shock is located at $x = 0.75$. The incident fast shock is initially located x=0.97 close to the right boundary of the simulation domain. Because of the super-fast flow of the solar wind in the negative x direction, the fast shock is actually moving towards the bow shock. From the bow shock side (downstream) to the sunward side (upstream) of the reverse fast shock, the plasma density, pressure, and magnetic pressure all decreases. The plasma flow speed in the negative x direction increases. In the specific case

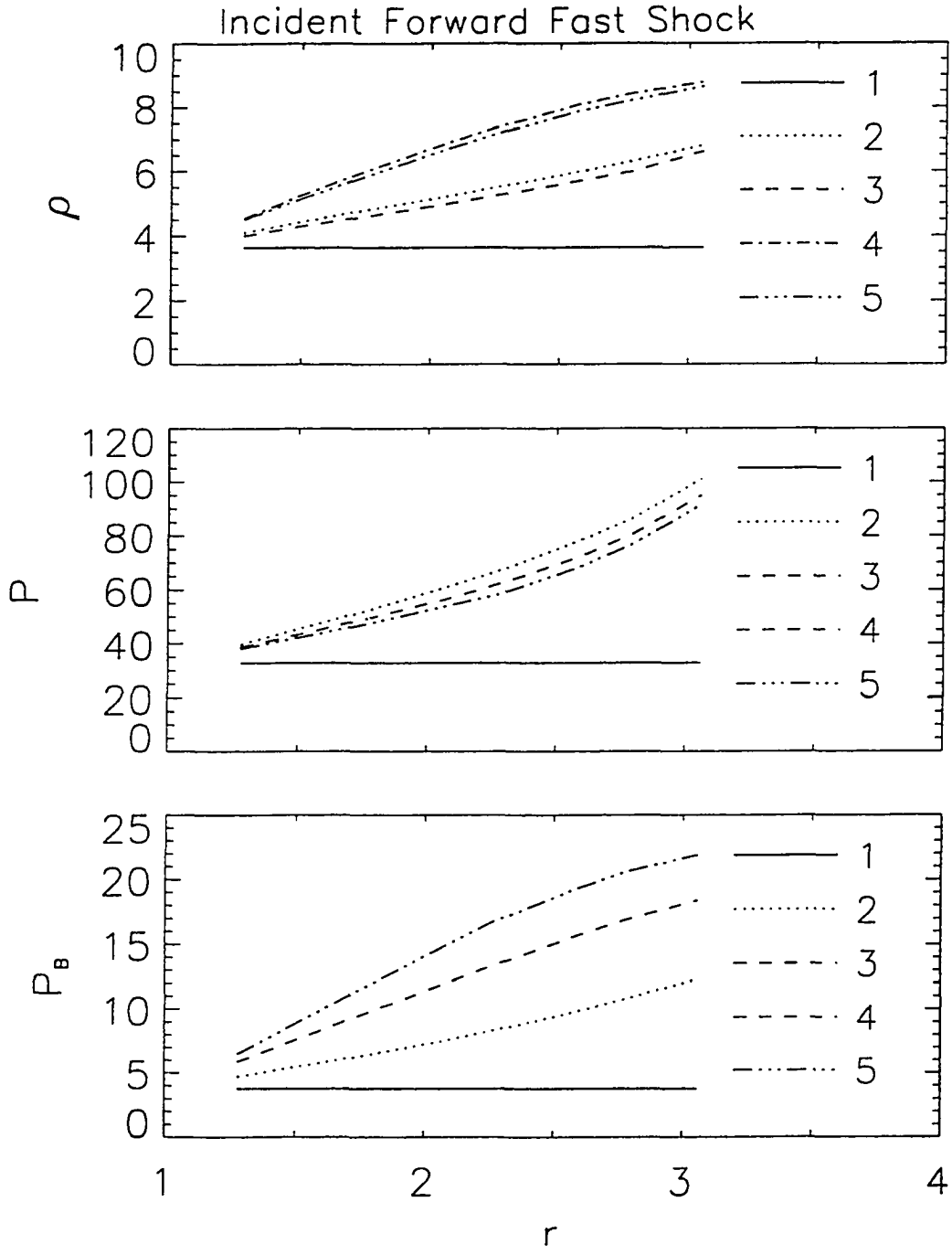

Figure 3.4 Plasma density ρ, pressure P, and magnetic pressure P_B in the five uniform regions after the interaction as functions of the strength of the incident shock r, given $M_A = 7$, $\beta = 1$, and $\theta = 45^o$.

shown in Figure 3.5, the parameters are chosen as $M_A = 4$, $\beta = 1$, $\theta = 45^o$, and $r = 1.5$.

As the incident reverse fast shock crosses the bow shock, a fast expansion wave, a slow shock, a contact discontinuity, and a slow expansion wave are produced downstream of the bow shock. In the plot for $t = 0.23$, the positions of the fast shock, slow shock, slow expansion wave, and the contact discontinuity are indicated by the dashed lines. At $t = 0.23$, the fast expansion wave is located at $x = 0.11$. From its upstream (left side) to downstream (right side), the plasma density, pressure, and magnetic pressure all decreases. The slow shock is located at $x = 0.49$. From the upstream (left) to the downstream (right) of the slow shock, the plasma density and pressure increase while the magnetic pressure decreases. The contact discontinuity is between the slow shock and the slow expansion wave and located at $x = 0.55$. From the magnetopause side to the bow shock side of the contact discontinuity, the plasma density decreases while the plasma temperature increases. The plasma flow velocity and magnetic field does not have any variation across the contact discontinuity. The slow expansion wave is located at $x = 0.62$. From the upstream (right) to the downstream (left), the plasma density and pressure decrease while the magnetic pressure increases. After the shock-shock interaction, the bow shock moves farther away from the Earth because of the sudden decrease of the dynamic pressure across the incident reverse shock. It is found in our simulations that the pressure decrement is about 25% at the fast expansion wave for $M_A = 10$, and the plasma density and pressure variations are small at the slow expansion wave or the slow shock. The dependence of the strengths of the transmitted shocks or waves on M_A, r and other parameters are similar to those shown in Figure 3.3 and 3.4 for the incident forward fast shocks.

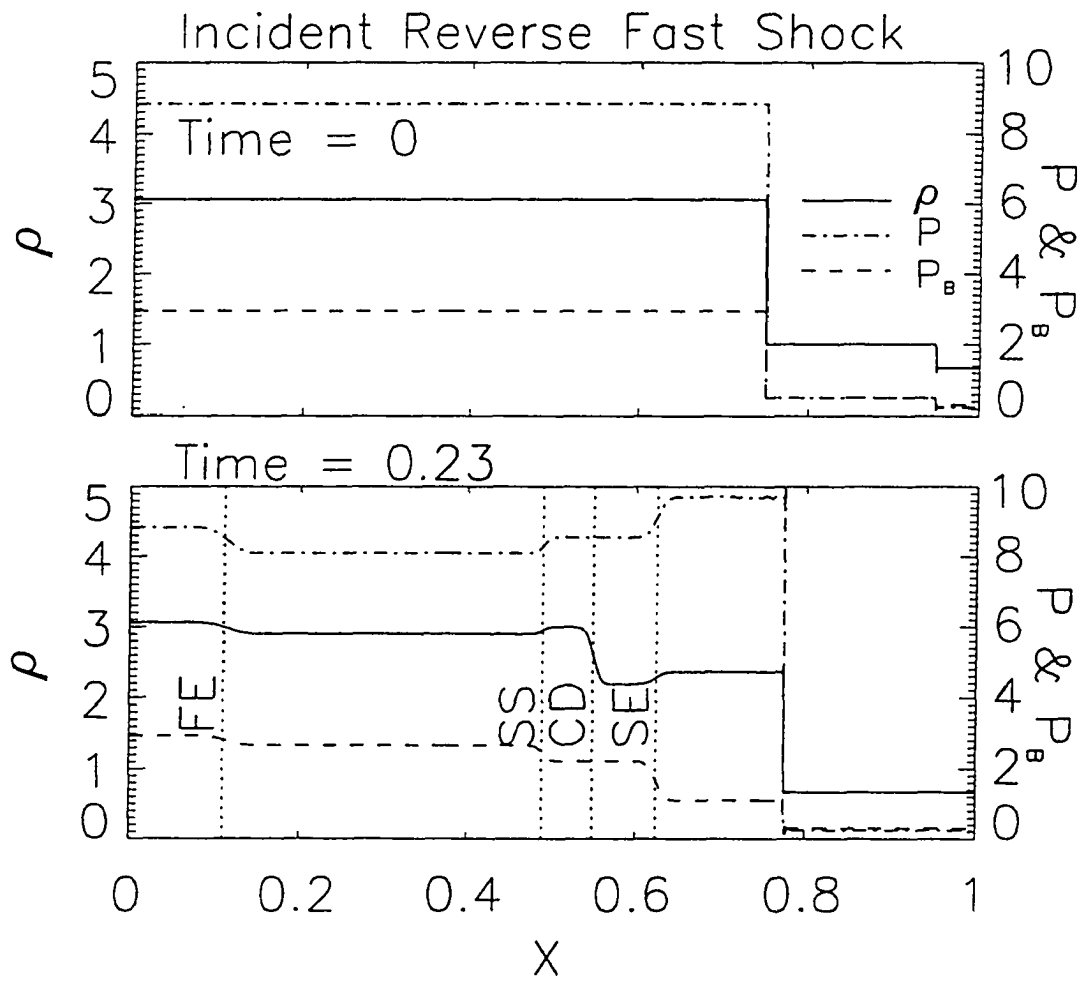

Figure 3.5 Spatial profiles of the plasma density ρ, pressure P, and magnetic pressure P_B at times t =0 and 0.23 for a case with an incident reverse fast shock. The parameters chosen are $M_A = 4$, $\theta = 45^o$, $\beta = 1$, and $r = 1.5$.

3.4 Incident Slow Shocks

3.4.1 Forward Slow Shocks

Figure 3.6 shows the spatial distributions of the plasma density, pressure, and magnetic pressure at times t =0 and 0.22 for a case with an incident forward slow shock which propagates towards the bow shock in the plasma frame. Initially, the bow shock is standing at the $x = 0.85$. The slow shock is located at $x = 0.95$ close to the right simulation boundary. From the upstream (left) to the downstream (right) of the incident slow shock, the plasma density and pressure both increase and the magnetic pressure decreases. For the specific case shown in Figure 3.7 the parameters are chosen as $M_A = 4$, $\theta = 45^o$, and $\beta = 0.5$. The strength r of the incident slow shock, which is defined as the ratio of the plasma density of the downstream to the upstream, is given as $r = 1.5$.

As the incident slow shock crosses the bow shock, from the left to the right, a fast shock, a slow shock, a contact discontinuity, and a slow expansion wave are generated. Because of the higher dynamic pressure after the incident forward slow shock, the bow shock moves towards Earth after impact with the slow shock. From the upstream (left) to the downstream (right) of the fast shock, the plasma density, pressure, and magnetic pressure all increase. From the upstream (left) to the downstream (right) of the slow shock, the plasma density and the pressure increase while the magnetic pressure decreases. From the magnetopause side to the bow shock side of the contact discontinuity, the plasma density increases. From the upstream (right) to the downstream (left) of the slow expansion wave, the plasma density and pressure decrease while the magnetic pressure increases.

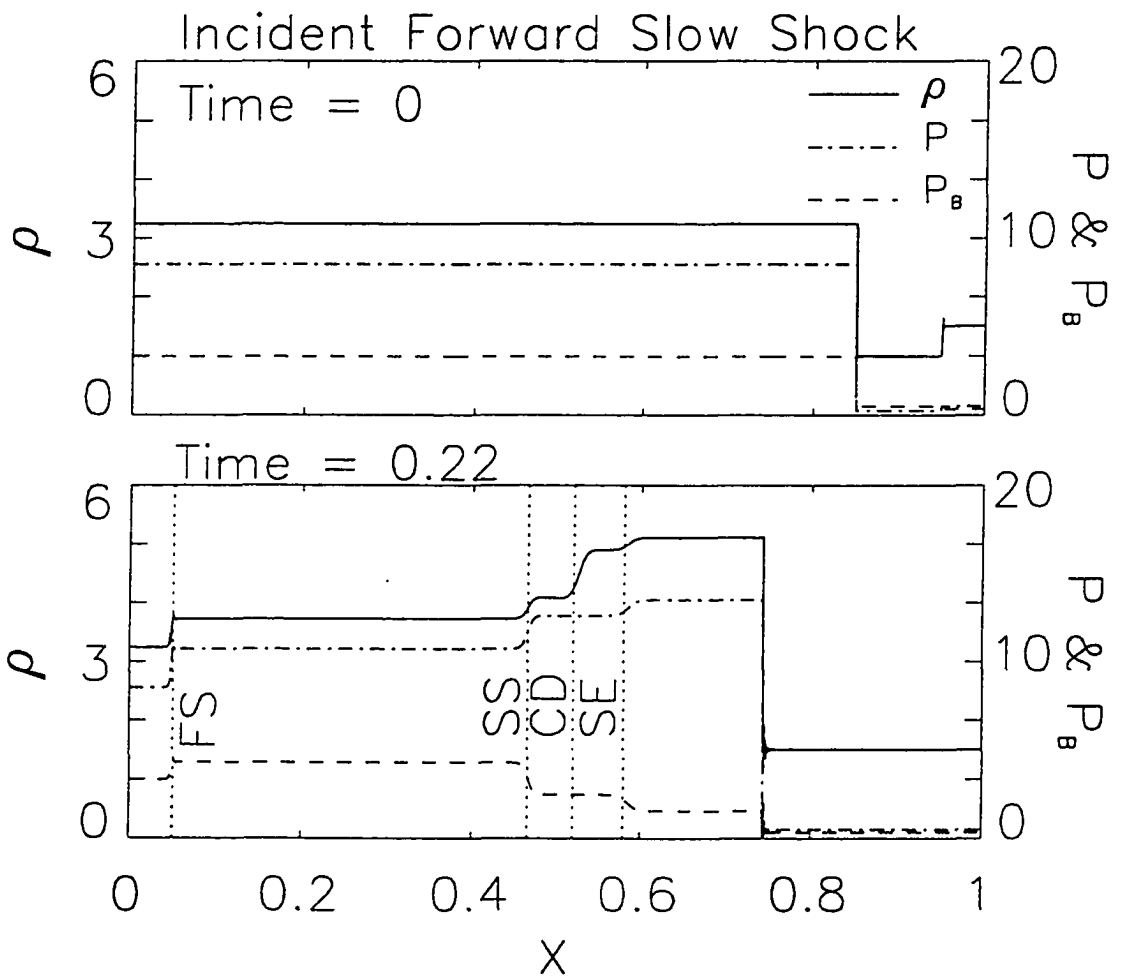

Figure 3.6 Spatial profiles of the plasma density ρ, pressure P, and magnetic pressure P_B at times t =0 and 0.22 for a case with an incident forward slow shock. The parameters chosen are $M_A = 4$, $\theta = 45^o$, $\beta = 0.5$, and $r = 1.5$.

Figure 3.7 shows the spatial profiles of the total pressure $P_T = P + P_B$ and dynamic pressure based on the total velocity $P_v = \rho v^2$ at time 0.22 for the same case shown in Figure 3.6. The dynamic pressure jump associated with the incident forward slow shock is about 13. After the interaction, the dynamic pressure jump is distributed to all the waves generated downstream of the bow shock. The total pressure P_T does not change at the slow shock, slow expansion wave, and the contact discontinuity. The increment in P_T is about 3 at the fast shock. The dynamic pressure based on the total flow velocity P_v has a jump of about 5 at the fast shock, 3 at the slow shock, and another 3 at the contact discontinuity. At the slow expansion wave, the dynamic pressure decreases a little from the left to right side. The jump of overall pressure $(P_T + P_v)$ at the generated fast shock is 8, which is 61% of the dynamic pressure jump associated with the incident slow shock. The jump of overall pressure is 23% at the slow shock. The same jump occurs at the contact discontinuity. The pressure variations at the slow shock and the contact discontinuity relative to the pressure jump at the incident shock are much higher in cases with low Alfven Mach numbers than cases with higher Alfven Mach numbers.

3.4.2 Reverse Slow Shocks

Figure 3.8 shows the spatial profiles of the plasma density, pressure, and magnetic pressure at times t =0 and 0.22 for a case with an incident reverse slow shock which propagates away from the bow shock towards the Sun in the plasma frame. Initially, the bow shock is standing at the $x = 0.7$, and the slow shock is located close to the left boundary. For the specific case shown in Figure 3.8, the parameters are chosen as $M_A = 4$, $\theta = 45^o$, $\beta = 1$, and $r = 1.5$.

As the incident slow shock crosses the bow shock, a fast expansion wave, a slow expansion wave, a contact discontinuity, and a slow shock are present downstream of

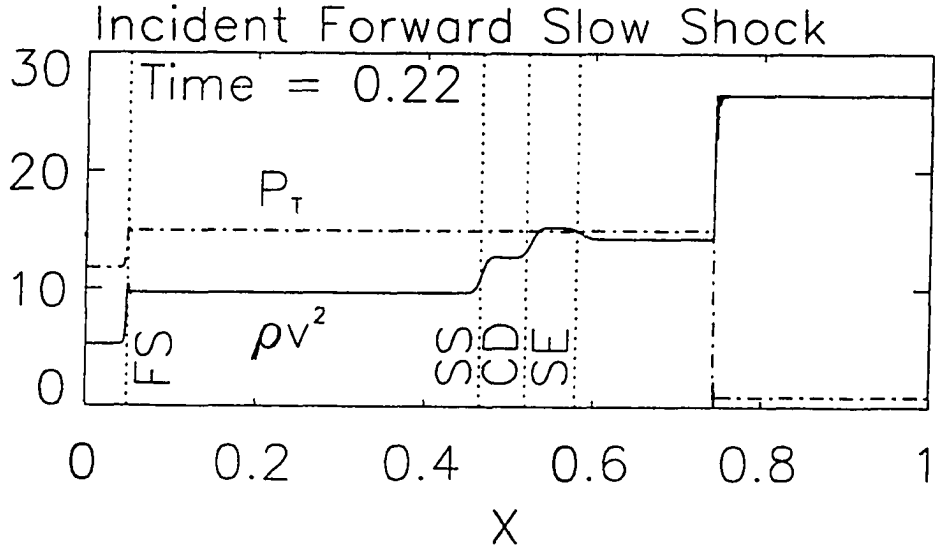

Figure 3.7 Spatial profiles of the dynamic pressure $P_v = \rho v^2$, and the total pressure $P_T = P + P_B$ at time 0.11 for the case shown in Figure 3.6.

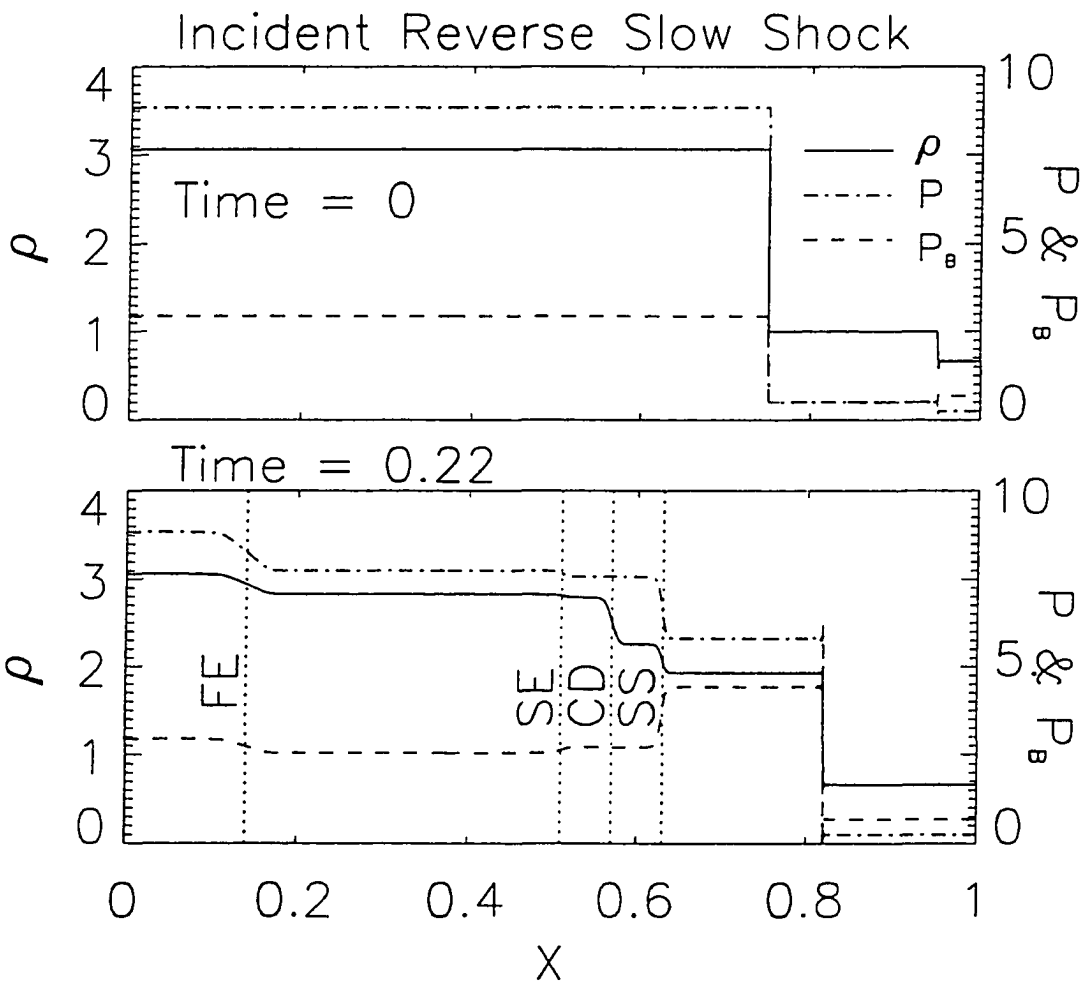

Figure 3.8 Spatial profiles of the plasma density ρ, pressure P, and magnetic pressure P_B at times t =0 and 0.22 for a case with an incident reverse slow shock. The parameters chosen are $M_A = 4$, $\theta = 45^o$, $\beta = 1$, and $r = 1.5$.

the bow shock as shown in Figure 3.8. Because of the lower dynamic pressure behind the incident reverse slow shock, the bow shock moves farther away from Earth after the impact of the the slow shock. From the upstream (left) to the downstream (right) of the fast expansion wave, the plasma density, pressure, and magnetic pressure decrease. From the upstream (left) to the downstream (right) of the slow expansion wave, the plasma density and the pressure both decrease while the magnetic pressure increases. From the magnetopause side to the bow shock side of the contact discontinuity, the plasma density decreases. From the upstream (right) to the downstream (left) of the slow shock, the plasma density and pressure increase while the magnetic pressure decreases.

3.5 Incident Rotational Discontinuities

3.5.1 Forward Rotational Discontinuities

Figure 3.9 shows the plasma density, thermal pressure, magnetic pressure, two tangential components of the magnetic field, total pressure ($P_T = P + P_B$), and the dynamic pressure associated with the total velocity ($P_v = \rho v^2$) at time 0.36 after an incident forward rotational discontinuity interacts with the bow shock. Initially, the bow shock is located at $x = 0.85$. The incident rotational discontinuity is located just upstream of the bow shock, and propagates towards the Earth in the plasma frame. For the case shown in Figure 3.9, the parameters are chosen as $M_A = 5$, $\beta = 1$, $\theta = 60^o$, and $\Delta\phi = 180^o$. Because there is no pressure variation associated with the incident rotational discontinuity, the bow shock remains at its original position after the interaction. A localized plateau appears in the plasma density and

thermal pressure. The magnetic pressure is depressed accordingly. The maximum density enhancement in the plateau is 16% of the background value. The maximum thermal pressure enhancement is about 30% of the background value. The maximum decrement of the magnetic pressure is close to 100% of the background value. As shown in the lowest panel of Figure 3.9, the sum of the thermal pressure and the magnetic pressure is constant across the generated density plateau. We also draw a line for the dynamic pressure based on the total flow velocity. This quantity is useful because the plasma flow tangential to the bow shock may partly become normal flow for the magnetopause since the bow shock and the magnetopause are generally not parallel to each other. From Figure 3.9, this dynamic pressure is enhanced slightly over 100%.

The leading edge of the plateau actually consists of an intermediate shock and a slow shock. They propagate towards the magnetopause in the plasma frame. Across the intermediate shock, plasma density and thermal pressure increase while the magnetic pressure decreases. These variations are the same across the slow shock. Simulations show that the tangential magnetic field rotates exactly the same angle across the intermediate shock as in the incident rotational discontinuity. In the case shown in Figure 3.9, the tangential magnetic field rotates 180^o across the intermediate shock. The magnetic field is in the $x - z$ plane in both the upstream and downstream regions of the intermediate shock. For cases with an incident rotational discontinuity of which the magnetic field rotation is out of the $x - z$ plane, the intermediate shock becomes a time-dependent intermediate shock since the shock normal and the magnetic field vectors in the upstream and downstream regions are not in the same plane. The shock thickness increases with time as $\sqrt{t}$ [*Wu*, 1988]. The trailing edge of the plateau is mainly a slow shock with enhancements of plasma density and thermal pressure and a decrease in magnetic pressure. Trailing the trailing edge is

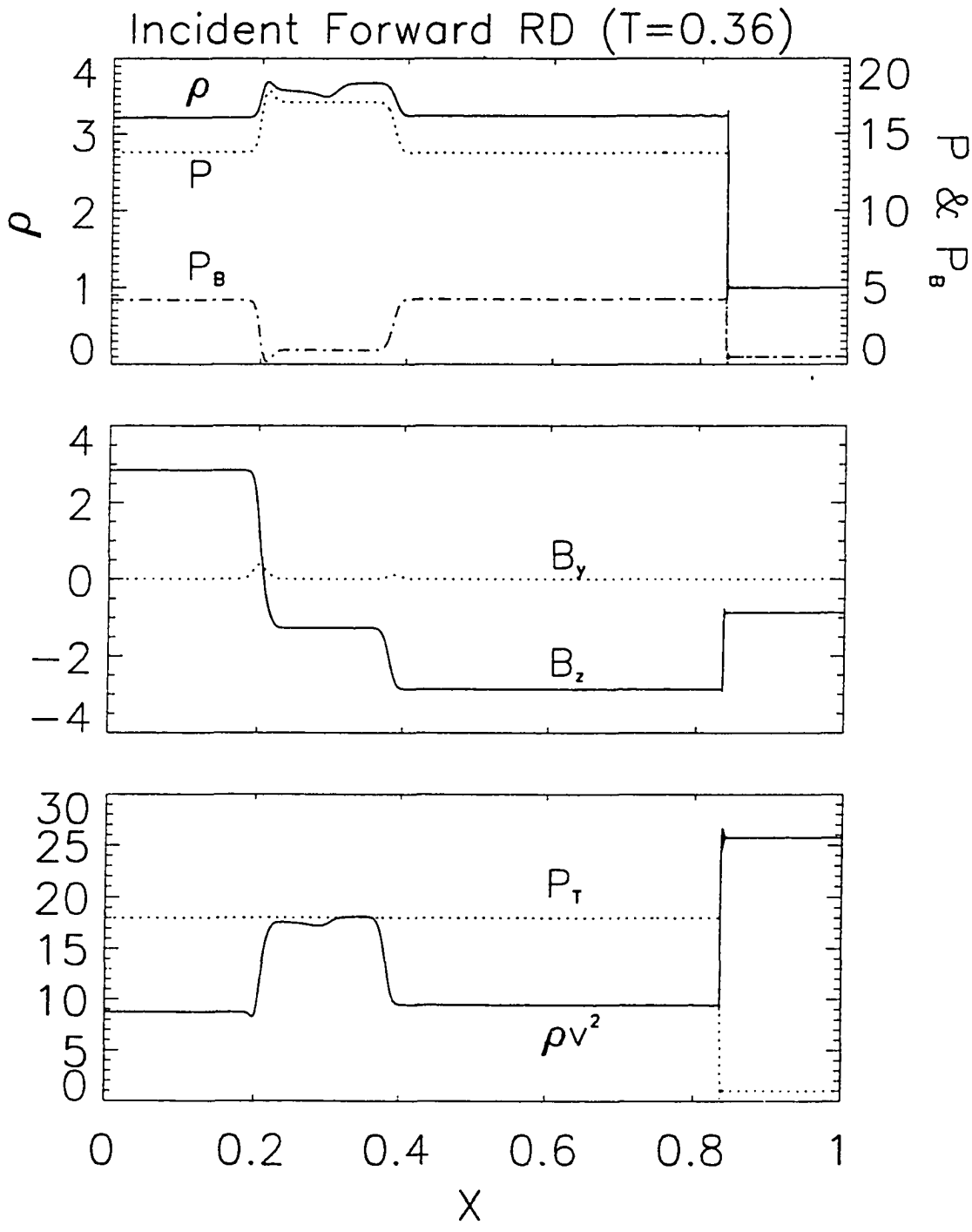

Figure 3.9 Spatial profiles of the plasma density ρ, pressure P, and magnetic pressure P_B, tangential components of the magnetic field B_y and B_z, total pressure $P_T = P + P_B$, and dynamic pressure P_v at time 0.36 for a case with an incident forward rotational discontinuity. The parameters chosen are $M_A = 5$, $\theta = 60^o$, $\beta = 1$, and $\Delta\phi = 180^o$.

an Alfven wave with variations only in the direction of the magnetic field. But the overall rotational angle across the Alfven wave is zero. The slow shock and Alfven wave propagate towards the bow shock in the plasma frame. The phase speeds for the Alfven mode and slow mode waves are very close to each other in the magnetosheath since the β value is usually very high. In the case shown in Figure 3.9, the phase speed for the Alfven mode and slow mode waves in the x direction are 0.28 and 0.24, respectively. At the same time, the normal plasma flow velocity is 1.54 in the negative x direction. As a result, the intermediate shock and the slow shock in the leading edge can hardly separate from each other. The same happens to the slow shock and the Alfven wave in the trailing edge. We have run a case with a weaker bow shock so that the plasma β is low downstream of the bow shock. The intermediate shock and the slow shock do separate in that case, and they can be identified by the Rankine-Hugoniot relations. There is a small amplitude fast-mode wave ahead of the plateau. In the middle of the plateau, there exists a plasma density variation without any variation on the plasma pressure and magnetic field, which is an entropy wave. Entropy wave is a wave mode in addition to the fast-mode, slow-mode, and Alfven-mode waves in MHD theory. Its phase speed is zero in the plasma frame. There are only variations on the plasma density and temperature in an entropy wave, but the thermal pressure, magnetic field, and flow velocity are all constants. Its discontinuity form is contact discontinuity.

It should be noted that the rotational discontinuity does not exist in the resistive MHD model. In this simulation, resistivity is included and the incident rotational discontinuity should not be stable. On the other hand, rotational discontinuities are frequently observed in the solar wind [*Burlaga*, 1969]. Hybrid simulations also show the existence of rotational discontinuities [*e.g., Swift and Lee*, 1983; *Goodrich and Cargill*, 1991; *Lin and Lee*, 1993]. Therefore, we introduced the incident rotational

discontinuity right before the bow shock to avoid its decay due to a finite resistivity in our simulation. We have also simulated cases with incident Alfven waves that rotate the magnetic field just as the rotational discontinuity but in a much longer distance. These cases are important for the magnetosheath considering the abundance of large amplitude Alfven waves observed in the solar wind [*Belcher et al.*, 1969]. The results are same as the incident rotational discontinuity cases except that the downstream slow shocks become slow compressional waves, and the intermediate shock becomes an Alfven wave.

Figure 3.10 shows the plasma density, thermal pressure, and magnetic pressure as functions of the magnetic field rotation angle $\Delta\phi$ across the incident rotational discontinuity. The values downstream of the bow shock before the interaction are background values and are indicated by the solid-dotted line. The maximum values for the plasma density and thermal pressure and the minimum value for the magnetic pressure in the plateau formed after the interaction are respectively indicated by the solid lines. The variation increases with increasing rotation angle $\Delta\phi$. The variation first increases slowly from $\Delta\phi = 0$, fast around $\Delta\phi = 90^o$, and become slow again for $\Delta\phi > 180^o$. There is little change in the plasma density enhancement for $\Delta\phi > 180^o$. In cases with $\Delta\phi > 180^o$ or with an incident Alfven wave train instead of a single Alfven wave, some smaller-scale structures appear in the large slow-mode structure. The plasma density and magnetic field are anti-correlated in the smaller-scale structures. The whole slow-mode structure becomes more complicated. It should be noted that the variation also depends on other parameters M_A, β, and ϕ. For example, the relative variations increase for decreasing M_A.

3.5.2 Reverse Rotational Discontinuities

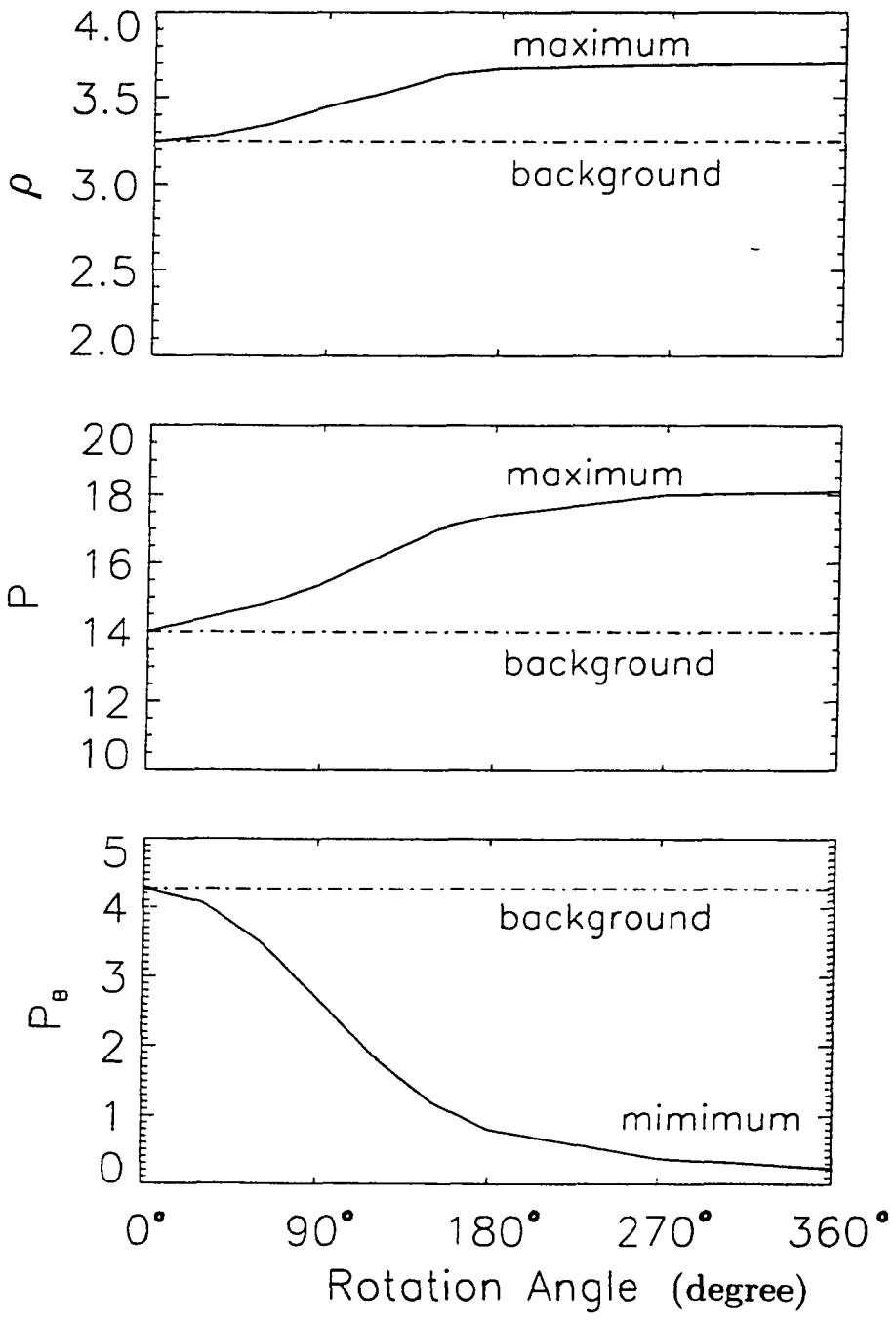

Figure 3.10 The plasma density ρ, pressure P, and magnetic pressure P_B as functions of the magnetic field rotation angle at the incident rotational discontinuity. The dot-dashed lines indicate the background value, while the solid lines indicates the maximum or minimum value after the interaction.

Figure 3.11 is the same as Figure 3.9 except that the incident rotational discontinuity propagates towards the Sun in the plasma frame, instead of towards Earth. Plateaus are formed in the plasma density and thermal pressure, and the corresponding magnetic pressure is depressed. The leading edge of the plateau consists of a slow shock and a small Alfven wave. The trailing edge consists of an intermediate shock and a slow shock. They propagate towards the bow shock in the plasma frame. An entropy wave appears in the middle of the plateau. Compared to the incident forward rotational discontinuity case, the leading edge and trailing edge in this case are reversed. The dependence of the maximum variation of the plasma density, pressure, and magnetic pressure on the parameters, such as the rotational angle and the M_A, are same as the cases with incident forward rotational discontinuities.

3.6 Summary

Figure 3.12 summarizes the results of the bow shock interaction with an incident interplanetary shock, which can be a forward fast shock, a reverse fast shock, a forward slow shock, or a reverse slow shock. Alfven waves, rotational discontinuities, or intermediate shocks are not generated in the interaction. A fast mode wave is produced in the interaction and propagates towards the magnetopause in the plasma frame. This fast mode wave is a fast shock when the incident shock is a forward fast shock or forward slow shock. It becomes a fast mode expansion wave when the incident shock is a reverse fast shock or a reverse slow shock. A contact discontinuity is also generated. From the magnetopause side to the bow shock side of the contact discontinuity, the plasma density increases (decreases) when the incident shock is of forward (reverse) propagation. In addition to the fast mode wave and the contact discontinuity, a pair of slow mode waves are also generated downstream of the bow

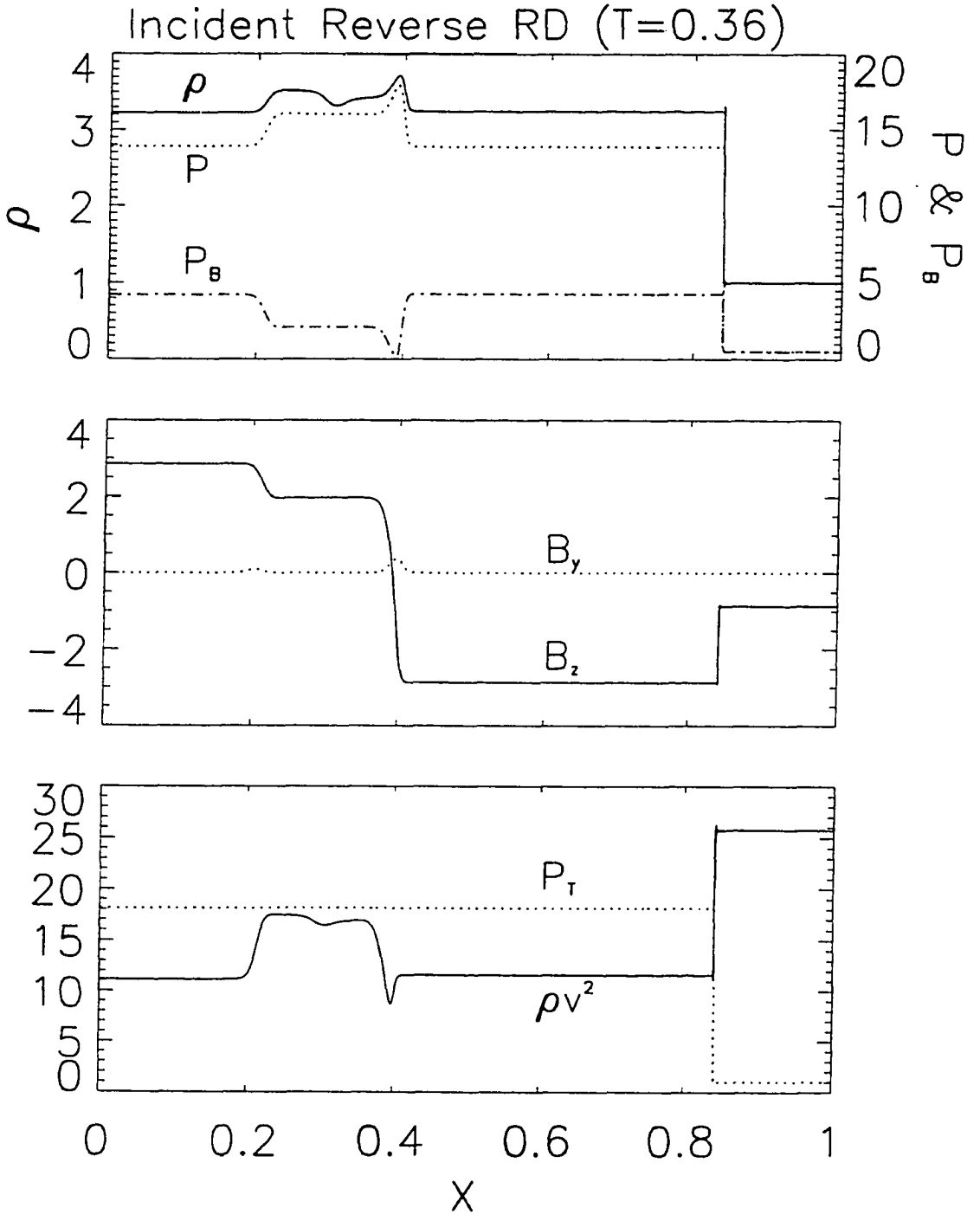

Figure 3.11 Same as in Figure 3.9 except for an incident rotational discontinuity.

shock. In the plasma frame, the one that propagates away from the bow shock is a slow expansion wave when the incident shock is a forward fast shock or a reverse slow shock. It becomes a slow shock when the incident shock is a reverse fast shock or a forward slow shock. The other slow mode that propagate towards the bow shock is a slow shock when the incident shock is a forward fast shock or a reverse slow shock. It becomes a slow expansion wave when the incident shock is a reverse fast shock or a forward slow shock. The bow shock itself is also modified after its interaction with the interplanetary shocks. For example, it moves towards (away from) the Earth when the incident shock is a forward (reverse) shock. It is noted that when the bow shock has a strength that is close to the incident forward fast shock, the slow modes become a pair of slow expansion waves. These cases are not included in Figure 3.12.

Figure 3.13 summarizes the results of the bow shock interaction with an incident rotational discontinuity which can propagate in the forward direction or in the reverse direction. The main products of the interaction include an intermediate shock and a pair of slow shocks. Across the intermediate shock, the tangential magnetic field rotates exactly the same angle as the incident rotational discontinuity. When the magnetic field does not satisfy the coplanary condition, the intermediate shock becomes a time-dependent intermediate shock (TDIS). A small Alfven wave and an entropy wave are also present in the simulation. For an incident forward (reverse) rotational discontinuity, the generated intermediate shock and a slow shock propagate towards the magnetopause (bow shock) while the other slow shock and the Alfven wave propagate towards the bow shock (magnetopause) in the plasma frame. Because of the high β property of the magnetosheath, the intermediate shock and the slow shock can hardly be separated from each other. As a result, a plateau is formed in the plasma density and thermal pressure. The magnetic pressure is depressed accordingly and is anti-correlated with the thermal pressure. For an incident rotational

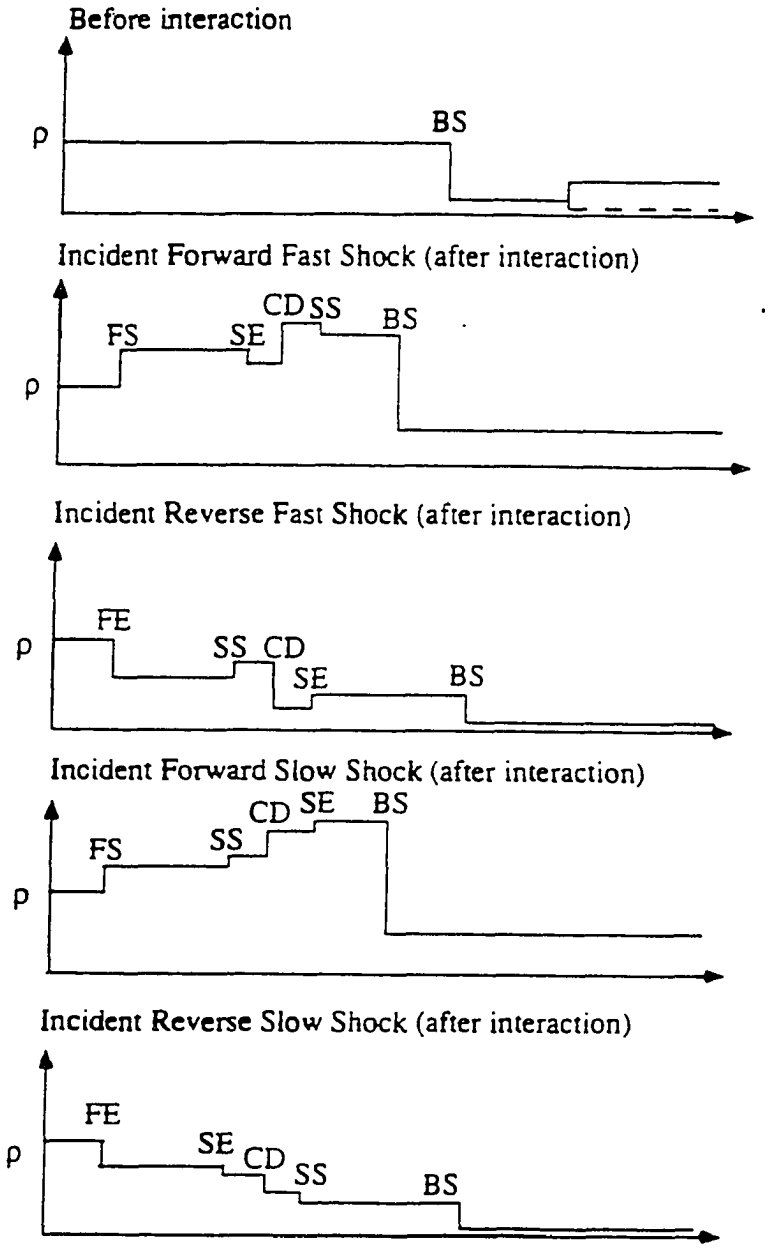

Figure 3.12 A schematic plot of the bow shock interaction with an incident interplanetary shock. The incident shock can be a forward fast shock, a reverse fast shock, a forward slow shock, or a reverse slow shock.

discontinuity with a magnetic field rotational angle of over 180^{o} or with an incident Alfven wave train instead of a single Alfven wave, some smaller-scale structures appear in the large slow-mode structure. The plasma density and magnetic field are anti-correlated in the smaller-scale structures.

Applications of these results to the slow-mode structures observed in the magnetosheath will be given in chapter 4 and 5.

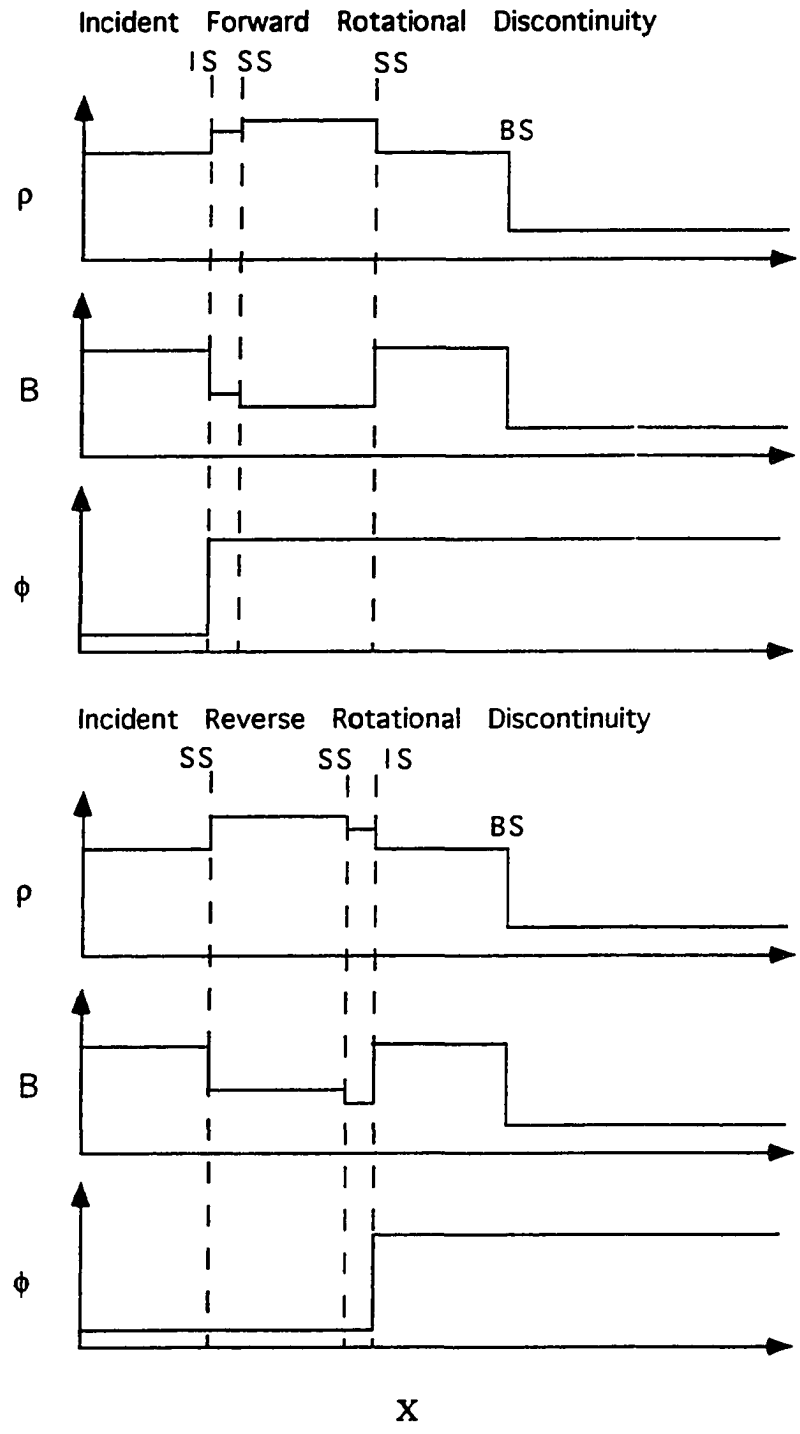

Figure 3.13 A schematic plot of the bow shock interaction with an incident forward or reverse rotational discontinuity. Only the main products of the interaction are shown in this plot.

Chapter 4 Generation of Slow-Mode Waves and Structures in the Inner Magnetosheath

The bow shock interaction with interplanetary shocks, rotational discontinuities, and large-amplitude Alfven waves are studied in chapter 3 in one-dimensional simulations. In this chapter, the interactions are studied further by using two-dimensional MHD simulations. In the two-dimensional simulations, the magnetopause is a boundary of the simulation domain and the bow shock is present in the middle of the simulation domain automatically as a result of the interaction between the super-fast solar wind flow and the magnetopause boundary. Along the Sun-Earth line, the solar wind flow speed decreases from super-fast speed to sub-fast and super-Alfven speed across the bow shock. It decreases further to zero at the stationary magnetopause since no plasma can go across the tangential discontinuity. This "slow-down" of the convection from post bow shock to the magnetopause has some important effects on the waves. The propagation and amplification of the waves generated at the bow shock are important issues and are addressed in this chapter.

The two-dimensional MHD simulation model is described in Section 4.1. The steady state magnetosheath is obtained as the first step of this study. In Section 4.2, the properties associated with the stationary configuration are briefly described. In Section 4.3, magnetosonic waves are imposed upstream of the stationary magnetosheath obtained in Section 4.2. The incident magnetosonic wave can be a fast-mode or a slow-mode wave. In Section 4.4, an Alfven wave is imposed upstream of the steady magnetosheath. The interaction between the bow shock and the waves are examined. The propagations of the generated waves in the nonuniform magnetosheath are also

studied. The simulation results are summarized in Section 4.5. The main results of this chapter has been published [*Yan and Lee*, 1994].

4.1 Two-Dimensional Simulation Model

Our study is based on compressible MHD equations (3.1-3.7). The two-dimensional assumption allows us to set $\partial/\partial z = 0$. In the x-y plane, the polar coordinates (r, θ) with the earth as the origin are used in the simulation. The simulation is carried out in a domain defined by $10R_E < r < 40R_E$ and $|\theta| \leq \pi/2$. The boundary at $r = 10R_E$ is assumed to be the magnetopause on which the normal components of flow velocity and magnetic field are set to zero while the first order derivatives of all other quantities are set to zero. Along the outflow boundaries ($10R_E < r < 40R_E$, and $\theta = \pm\pi/2$) the first-order derivatives of all physical quantities are set to zero. On the upstream boundary at $r = 40R_E$, all physical quantities are set to the values of the solar wind. The Runge-Kutta scheme with a second-order accuracy in space and fourth-order accuracy in time is adopted to intergrate the MHD equations. A total of 600×1200 grid points are uniformly distributed in r and θ directions with a spatial resolution of $0.05R_E$ in the r direction and about $0.04R_E$ in the θ direction near the magnetopause. The numerical dissipation involved in the adopted finite difference method is estimated to be about 0.001 in the normalized unit of $\mu_0 V_A R_E$.

In this chapter, the magnetic field $\mathbf{B}$, density ρ, and velocity $\mathbf{v}$ are normalized by the solar wind magnetic field B_0, density ρ_0, and Alfven velocity $V_{A0} = B_0/\sqrt{\mu_0\rho_0}$, respectively. The length is normalized by Earth's radius R_E, time by $t_A = R_E/V_{A0}$, and pressure by $P_0 = B_0^2/\mu_0$.

4.2 Steady Magnetosheath

As the first step of this study, we keep the solar wind and the IMF parameters unchanged for a long time until the magnetosheath finally reaches a steady state. Figure 4.1 shows the magnetic field lines, flow velocity, and contours of the thermal pressure and plasma density in the simulation plane for the steady state. The solar wind parameters are: Alfven Mach number $M_A = 5$, $\beta = 0.5$, $B_x = B_z/2 = B_0/\sqrt{5}$, and $B_y = 0$. By assuming $B_0 = 7$ nT and $\rho_0 = 5$ cm^{-3} in the solar wind, we have $V_{A0} = 70$ km/s, $V_{sw} = 350$ km/s, and $t_A \approx 1.5$ minutes.

Because of the two-dimensional assumption, creation of a steady state solution requires the y component of the IMF be zero. If not, the magnetic flux would continue to pile up in front of the magnetopause. In the actual three-dimensional situation, the IMF can be oriented in any direction, and a steady state magnetosheath will always be found for any set of upstream conditions. Note that the magnetic field and the flow velocity may have z components in the two-dimensional simulation even though the simulation is only in the x-y plane.

In Figure 4.1, the magnetopause is located at the $r = 10\ R_E$ half circle by the boundary conditions. The outer boundary at $r = 40\ R_E$ is in the solar wind. The bow shock appears in the simulation domain automatically because of the interaction between the magnetopause boundary and the super-fast flow of the solar wind. Upstream of the bow shock, all physical quantities are uniform in space. The flow velocity is in the -x direction. Along the Sun-Earth line across the bow shock, the plasma flow velocity decreases from super-fast speed to a sub-fast speed. The plasma density and the thermal pressure are both enhanced. The x component of the magnetic field does not change since it is perpendicular to the shock front, but the z component, which is perpendicular to the simulation domain, is enhanced. The total

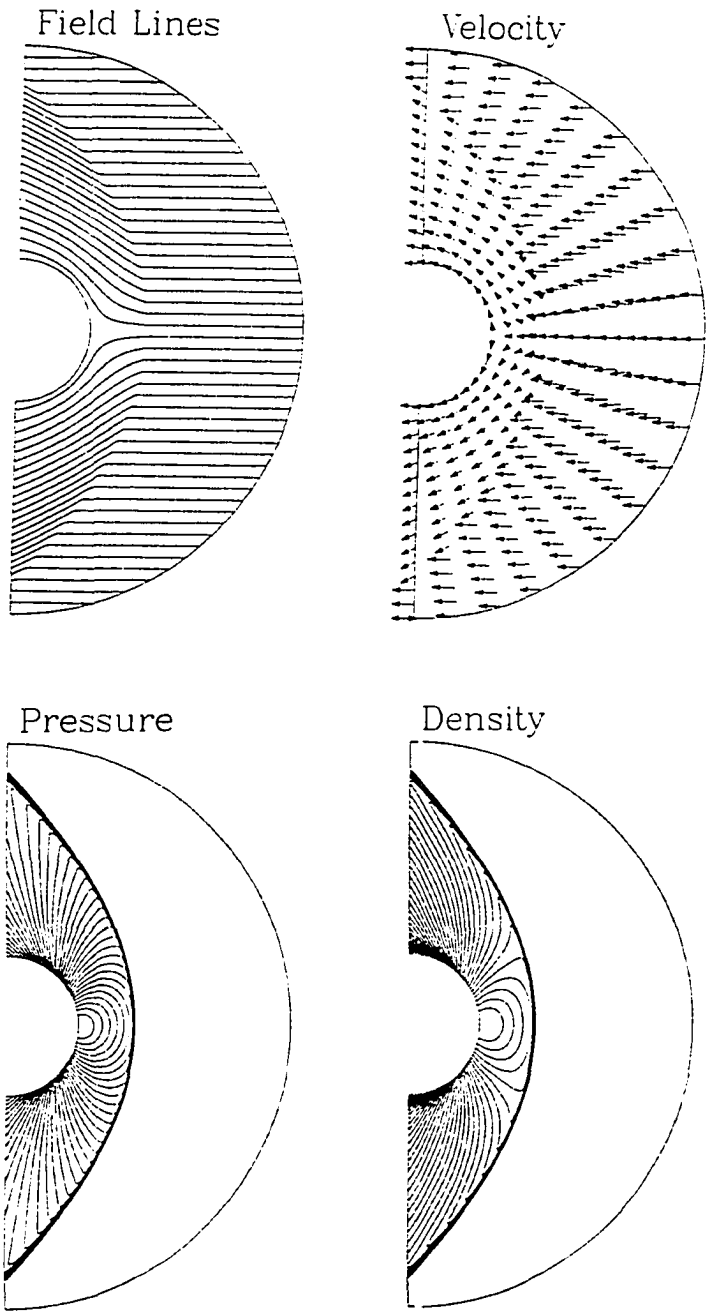

Figure 4.1 Magnetic field lines, plasma flow velocity, and contours of thermal pressure and plasma density of the steady magnetosheath.

magnetic field, therefore, increases. From the bow shock to the magnetopause, the plasma flow speed further decreases while the plasma density and thermal pressure increase. The plasma flow velocity in the simulation plane becomes zero at the magnetopause. At the same time, the plasma density and the thermal pressure reaches their maximum values in the magnetosheath. Away from the Sun-Earth line, the flow speed decreases across the bow shock. The flow normal to the shock front decreases from a super-fast speed to a sub-fast speed. However, the downstream total speed in the region far away from the subsolar area can be higher than the fast mode speed since the large tangential component does not change much across the shock. The plasma density enhancement decreases slowly away from the sub-solar area, while the thermal pressure enhancement decreases rather fast. The magnetic field lines are compressed since there is a finite tangential component in the simulation plane.

The above described configuration of the steady magnetosheath is quite similar to that obtained in the gasdynamic model as shown in Figures 1.1 and 1.2. The difference is that there is no y component of magnetic field in our simulation. As a result, there is no magnetic flux pile up and plasma depletion in the magnetosheath. The stationary bow shock is about $8R_E$ away from the magnetopause along the Sun-Earth line. For the stationary configuration $\rho = 3.4\rho_0$, $B = 2.9B_0$, $P = 17.4B_0^2/\mu_0$, and $V = 1.7V_A$ just downstream of the bow shock along the Sun-Earth line. It should be noted that the distance is about 3-5 R_E in the actual three-dimensional case.

This is only the first step of the two-dimensional simulation. The next step, which is more important, is to impose some fluctuations in the solar wind upstream of the steady bow shock to study the bow shock interaction with the fluctuations and propagation properties of the generated slow-mode waves in the nonuniform magnetosheath.

4.3 Incident Magnetosonic Waves

An magnetosonic wave is next superposed in the ambient solar wind upstream of the bow shock. The perturbed quantities are chosen according to the polarization of each mode. For fast-mode and slow-mode waves, the perturbed quantities can be written as [*e.g., Kuo*, 1988]

$$v_{x1} = V_{s,f}\rho_1/\rho_0 \tag{4.1}$$

$$v_{z1} = -\frac{V_A^2 V_{s,f}\sin\alpha\cos\alpha}{V_A^2\cos^2\alpha - V_{s,f}^2}(\frac{\rho_1}{\rho_0}) \tag{4.2}$$

$$B_{z1} = -\frac{V_{s,f}^2 B_0\sin\alpha}{V_{s,f}^2 - V_A^2\cos^2\alpha}(\frac{\rho_1}{\rho_0}) \tag{4.3}$$

$$P_1 = C_s^2\rho_1 \tag{4.4}$$

$$v_{y1} = B_{x1} = B_{y1} = 0\ , \tag{4.5}$$

where the subscript "1" indicates the perturbed quantities, V_s (V_f) indicates the phase speed of slow-mode (fast-mode) wave along the Sun-Earth line, V_A is the Alfven speed, C_s is the sound speed, and α is the angle between the magnetic field and the x direction, which directs from Earth to the Sun. The perturbed density is chosen as

$$\rho_1 = \delta\rho\sin[\frac{2\pi(x-x_0)}{\lambda_x}]\exp[-(\frac{y}{y_0})^2] \tag{4.6}$$

in the region $18R_E < x < 34R_E$, and $\rho_1 = 0$ in other regions. We set the wavelength $\lambda_x = 16R_E$, $x_0 = 18R_E$, and $y_0 = 8R_E$. The Gaussian function in ρ_1 is chosen such that the upstream boundary can be easily handled.

4.3.1 Incident Fast-Mode Wave

In Case 1, an incident fast-mode wave given by Equation 4.1-4.6 with $\delta\rho = 0.5\rho_0$ is superposed on the stationary configuration at t=0. Figure 4.2 shows the resulting

plasma density contours at six different times t=0, 3.5, 7, 10.5, 14, and 17.5 t_A ($t_A \approx$ 1.5min). Figure 4.3 shows the corresponding contours for thermal pressure. Figure 4.4 shows the magnetic field lines at time $t = 7\ t_A$. Figure 4.5 shows the profiles of plasma density ρ, thermal pressure P, and magnetic field B along the Sun-Earth line at t=0 (dashed line) and t=$7t_A$ (solid line). At t=0, the incident fast-mode wave is imposed just upstream of the bow shock. The variations of the plasma density and the magnetic field are right in phase as shown Figure 4.5 (dashed lines) indicate that the incident wave is a fast-mode wave.

The interaction between the incident magnetosonic wave and the bow shock will generate four wave modes downstream of the bow shock [e.g., *Mckenzie*, 1970]. They are: (a) one fast-mode wave, (b) two slow-mode waves, and (c) an entropy wave. In the plasma frame, the fast-mode wave, one slow-mode wave and one Alfven wave propagate towards the magnetopause; the other slow-mode wave and Alfven wave propagate towards the bow shock. The entropy wave does not propagate in the plasma frame. Since the downstream plasma is flowing from the bow shock to the magnetopause at a speed that is between the fast-mode phase speed and the Alfven speed, all four waves travel from the bow shock to the magnetopause.

The fast-mode wave propagates very fast in the magnetosheath. Its phase speed is found to be about $3.5V_{A0}$. Together with the convection velocity, the fast-mode wave can travel from the bow shock to the magnetopause in $1.5t_A$, and travel from the magnetopause back to the bow shock in about $5t_A$. In Figure 4.2, waves already appear in the magnetosheath at t=$3.5t_A$. The leading edge in the kink of the density contours is associated with the fast-mode wave, which propagates towards the magnetopause. It is found in the simulation that the fast-mode wave is reflected back at the magnetopause. As shown in Figure 4.2, at t=$7t_A$, the fast-mode wave has been reflected at the magnetopause and is propagating towards the bow shock. It can be

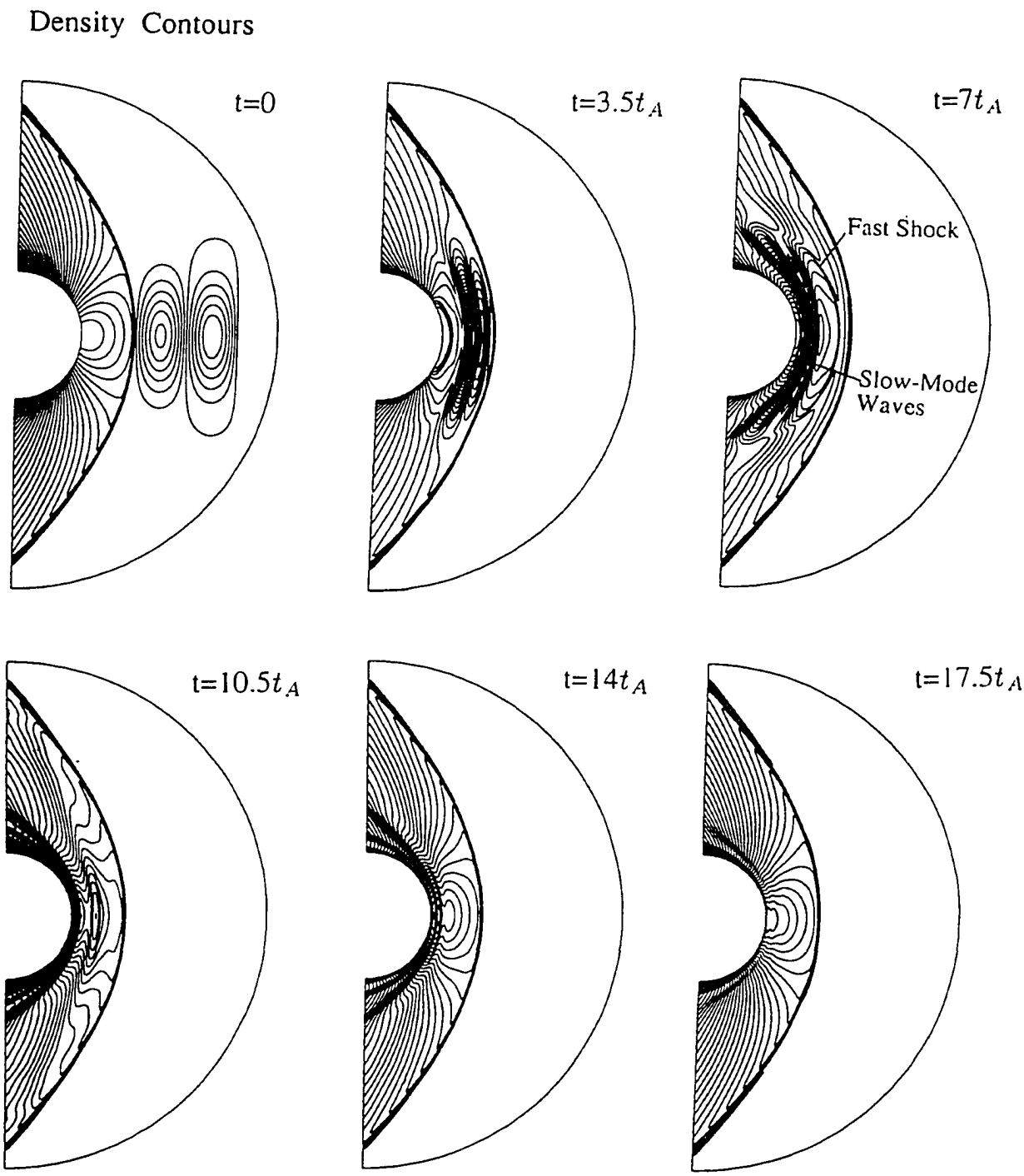

Figure 4.2 Plasma density contours at t=0, 3.5, 7, 10.5, 14, and 17.5 t_A (t_A = 1.5min) for Case 1. A fast-mode wave is imposed upstream of the bow shock at t=0.

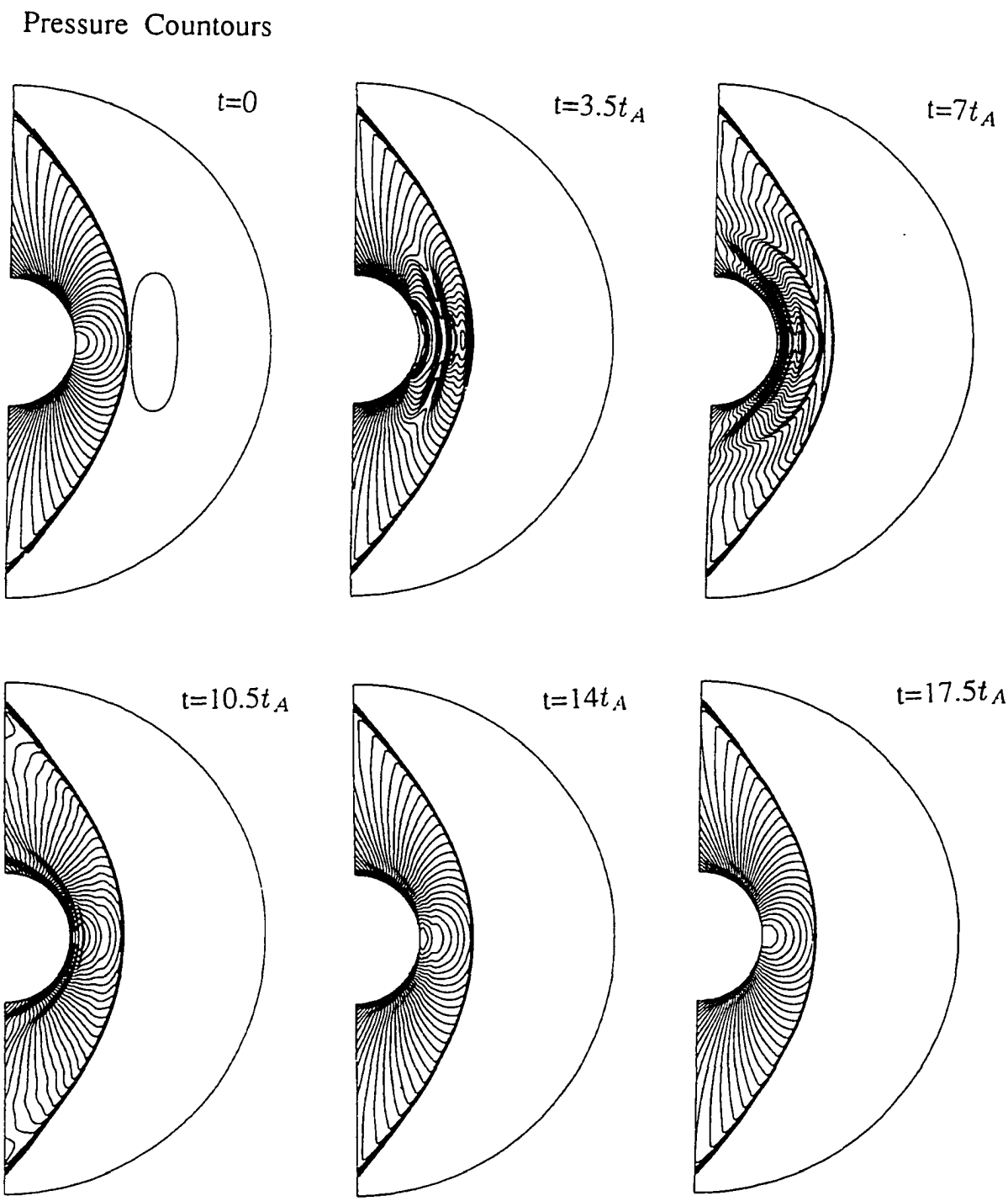

Figure 4.3 Thermal pressure contours at t=0, 3.5, 7, 10.5, 14, and 17.5 t_A (t_A = 1.5min) for Case 1. A fast-mode wave is imposed just upstream of the bow shock at t=0.

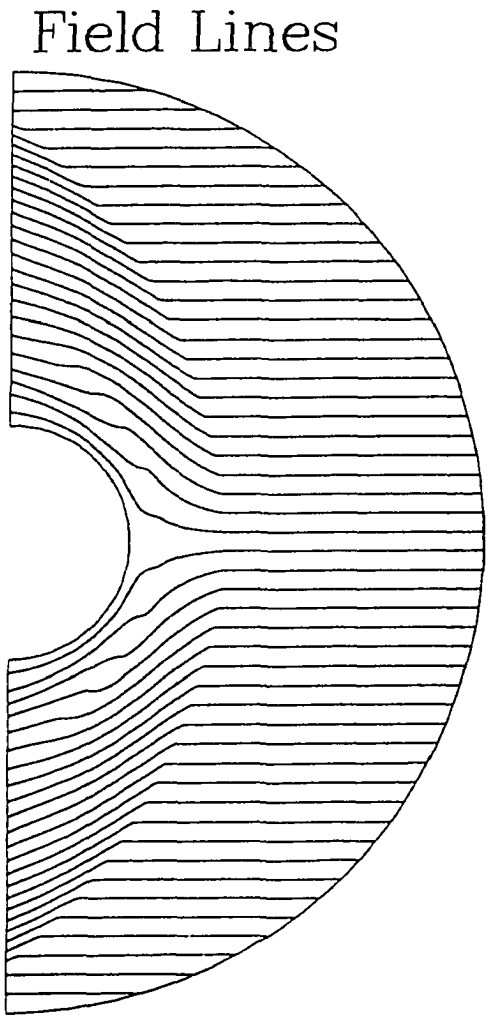

Figure 4.4 Magnetic field lines in the simulation plane for Case 1 with an incident fast-mode wave at t=7 t_A ($t_A \approx 1.5$ min).

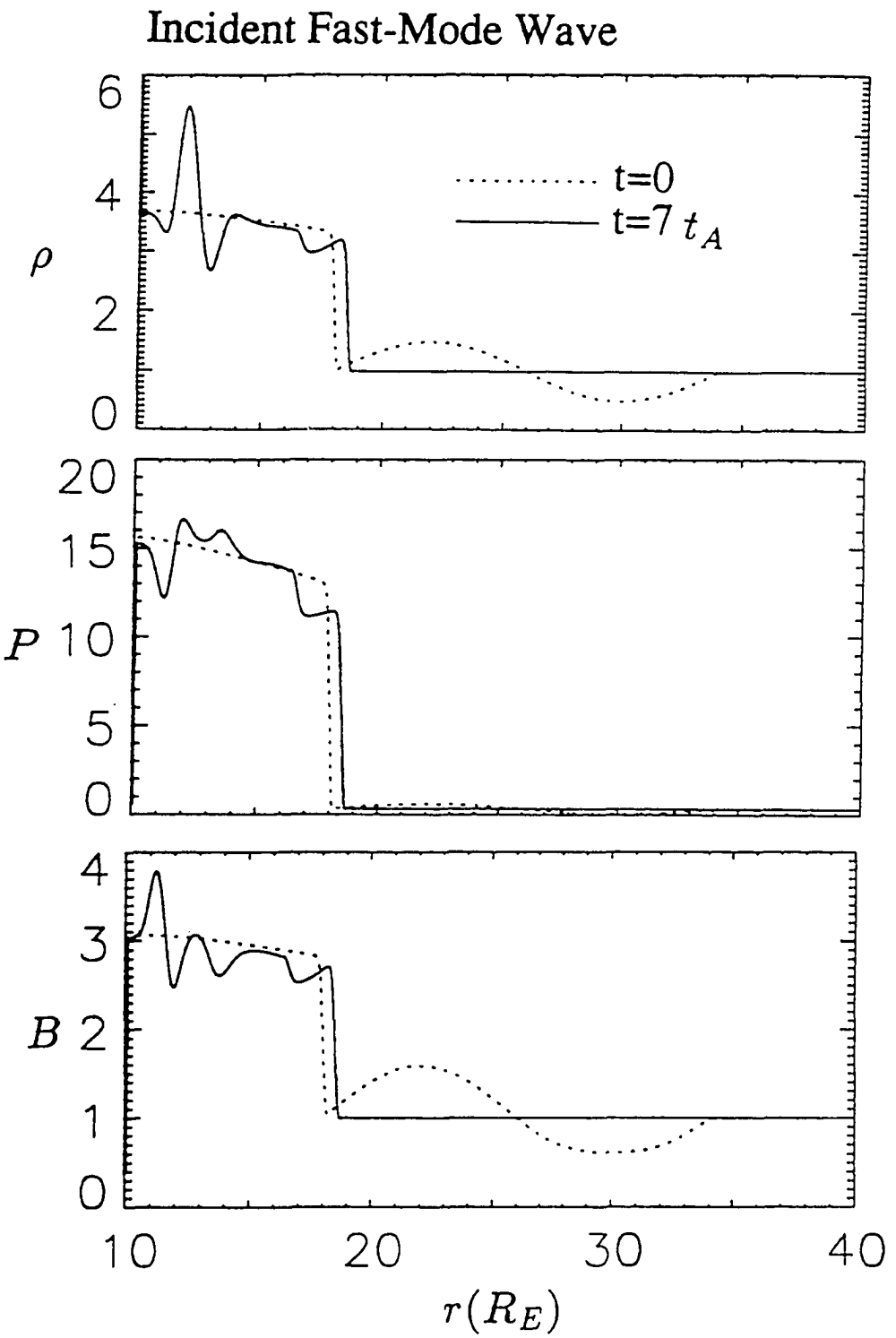

Figure 4.5 Profiles of plasma density ρ, pressure P, and magnetic field B along the Sun-Earth line at t=0 (dashed lines) and t=7t_A (solid lines) for Case 1 with an incident fast-mode wave.

seen in Figure 4.5 (solid lines) that the fast-mode wave has steepened to form a fast shock. In this simulation, the magnetopause is treated as a rigid body. Actually the magnetopause would move back and forth and some of the fast-mode wave energy would be transferred into the magnetosphere. The reflected waves should not be as strong as in this simulation. The fast shock merges into the bow shock before t=10.5t_A. The Alfven waves resulted from the interaction are very weak in this case.

At t=3.5t_A, the slow-mode waves have been formed in the magnetosheath and they are propagating towards the magnetopause. At t=7t_A, the excellent anti-correlation between the plasma pressure and the magnetic field shown in Figure 4.5 (solid lines) indicate that these waves are mainly slow-mode waves. The phase difference between the plasma pressure and density indicates the existence of the entropy wave. At this moment, the slow-mode waves have gone into the inner magnetosheath. Although there is only one period of a sinusoidal variation in the upstream incident wave, two complete periods of sinusoidal variations are present in the resulting slow-mode waves due to the separation of the two transmitted slow-mode waves in the magnetosheath. The kinks on the magnetic field lines as shown in Figure 4.4 correspond to the slow-mode waves in the inner magnetosheath. The wave fronts of all generated waves are mainly parallel to the magnetopause. The wavelength of the slow-mode waves normal to the magnetopause is $\lambda_n \approx 1.5R_E$ while the tangential wavelength λ_t is much larger than λ_n. In the three-dimensional configuration, λ_n may be further reduced due to compressed distance between the bow shock and the magnetopause. After t=7t_A, the slow-mode waves propagate more slowly towards the magnetopause because the actual propagation speed, which is the sum of the convection speed and the phase speed normal to the magnetopause, decreases to zero at the magnetopause. At the later time, the amplitude of the slow-mode waves decreases because the wave energy is convected tailward around the magnetopause.

The density and thermal pressure contours at t=7, 10.5, 14, and 17.5t_A in Figures 4.2 and 4.3 show clearly the slow propagation and decay of the slow-mode waves. The slow-mode waves stand in front of the magnetopause for about 10t_A (15 minutes) from t=7t_A when they have arrived the inner magnetosheath to t=17.5t_A asthey almost fade away.

4.3.2 Incident Slow-Mode Wave

In Case 2, we impose a slow-mode wave in the upstream solar wind. Figure 4.6 is the same as Figure 4.2 except that it for Case 2. Figure 4.7 is the same as Figure 4.3 except that it is for Case 2. Figure 4.8 shows the profiles of plasma density, pressure, and magnetic field along the Sun-Earth line at t=0 (dashed lines) and t=7t_A (solid lines). The results with the incident slow-mode waves are quite similar to those with incident fast-mode waves. The anti correlation between the plasma density ρ and magnetic field B upstream of the bow shock at t=0 indicates the incident wave is a slow-mode wave. The downstream fast-mode wave resulting from the interaction between the incident wave and the bow shock is also found to propagate from the bow shock to the magnetopause and then be reflected back to the bow shock. It should be noted that after the fast shock merges into the bow shock, another slow-mode wave is generated downstream of the bow shock which is convected to the magnetopause. The same process of wave mode conversion also occurs in the incident fast-mode wave case. No strong Alfven waves are generated through the interaction process. The generated slow-mode waves also stay in the inner magnetosheath for over 15 minutes before being convected away tailward.

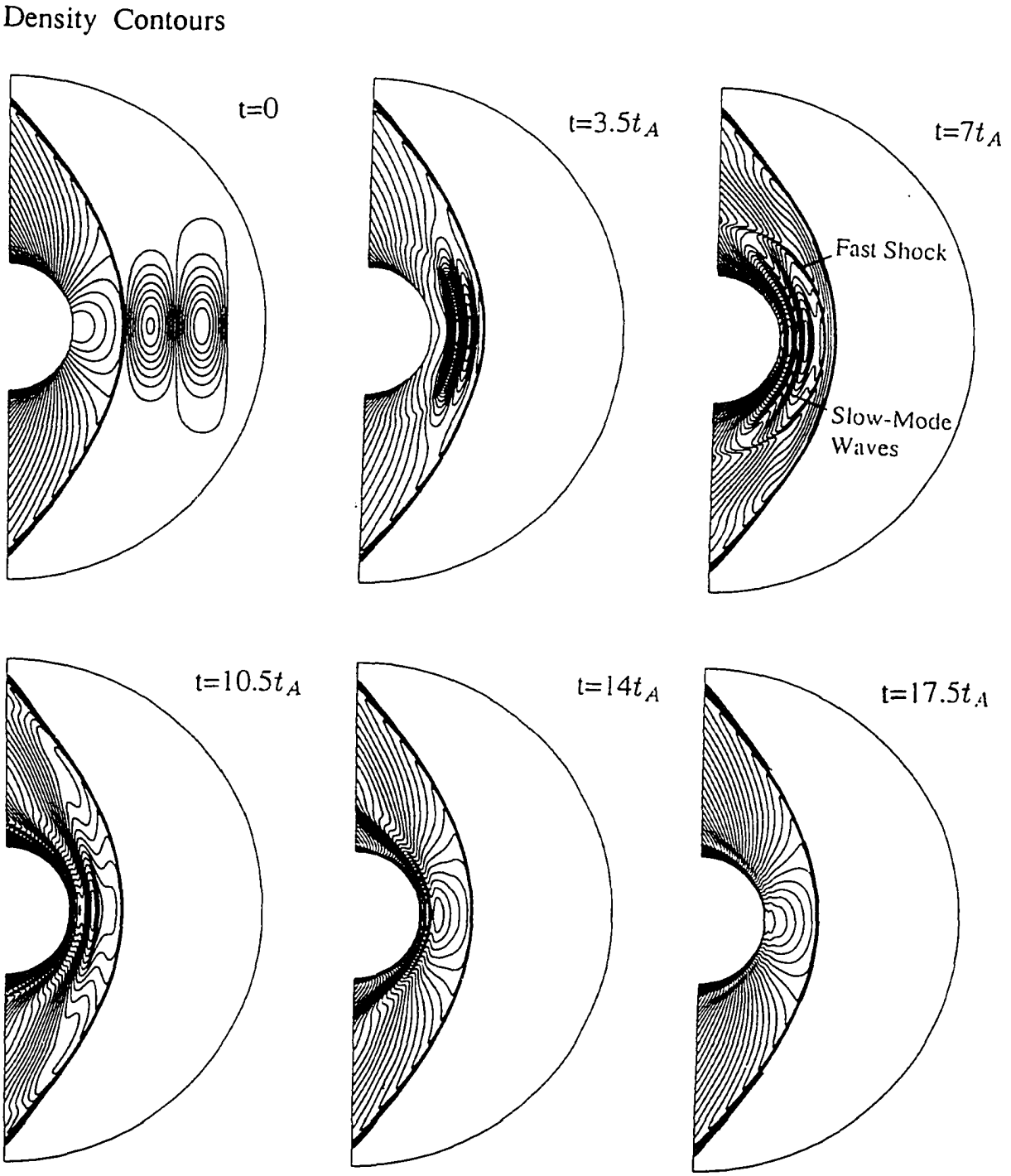

Figure 4.6 Profiles of density ρ, pressure P, and magnetic field B at t=0 (dashed lines) and t=7t_A (solid lines) for Case 2 with an incident fast-mode wave.

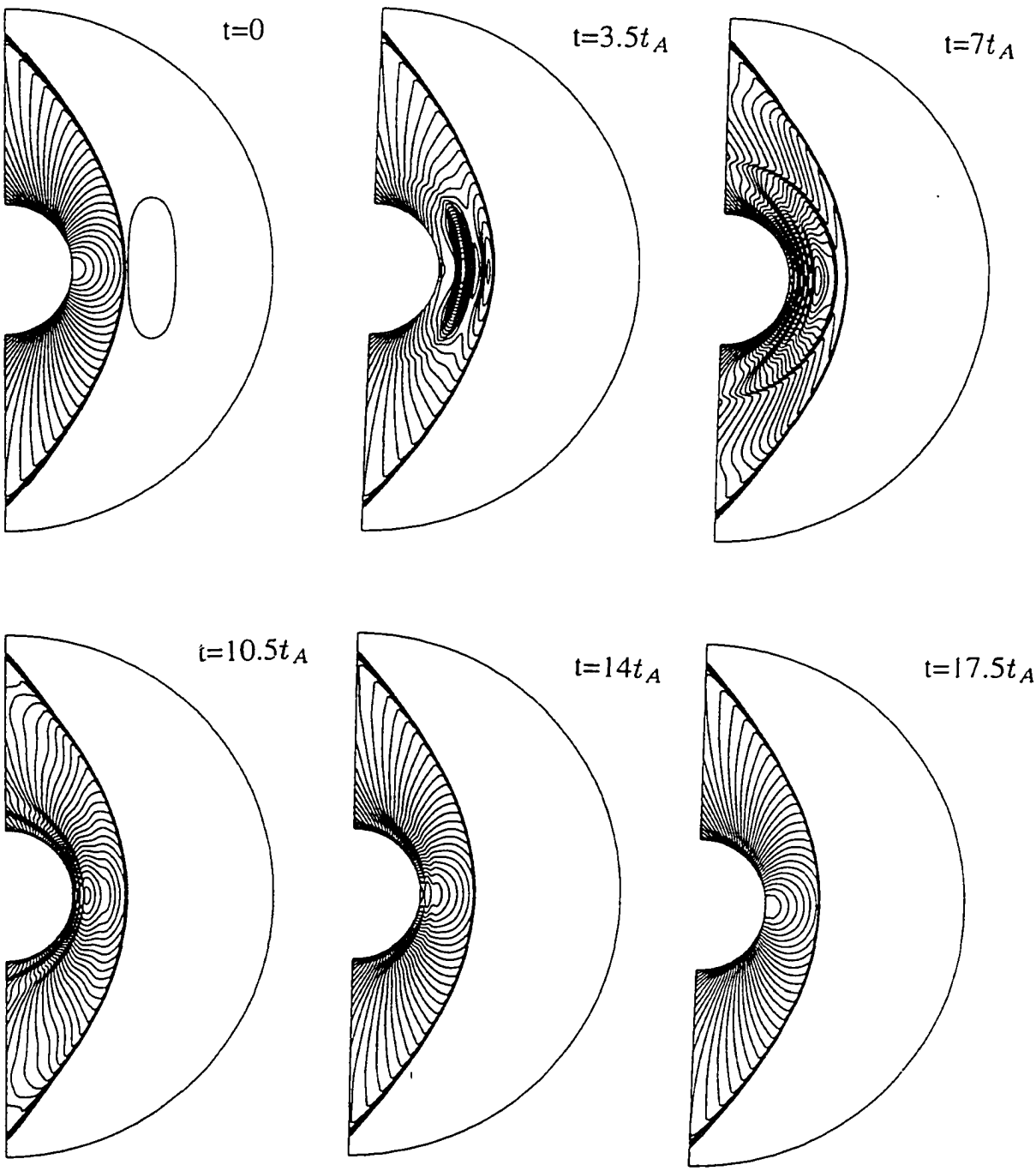

Figure 4.7 Profiles of density ρ, pressure P, and magnetic field B at t=0 (dashed lines) and t=7t_A (solid lines) for Case 2 with an incident fast-mode wave.

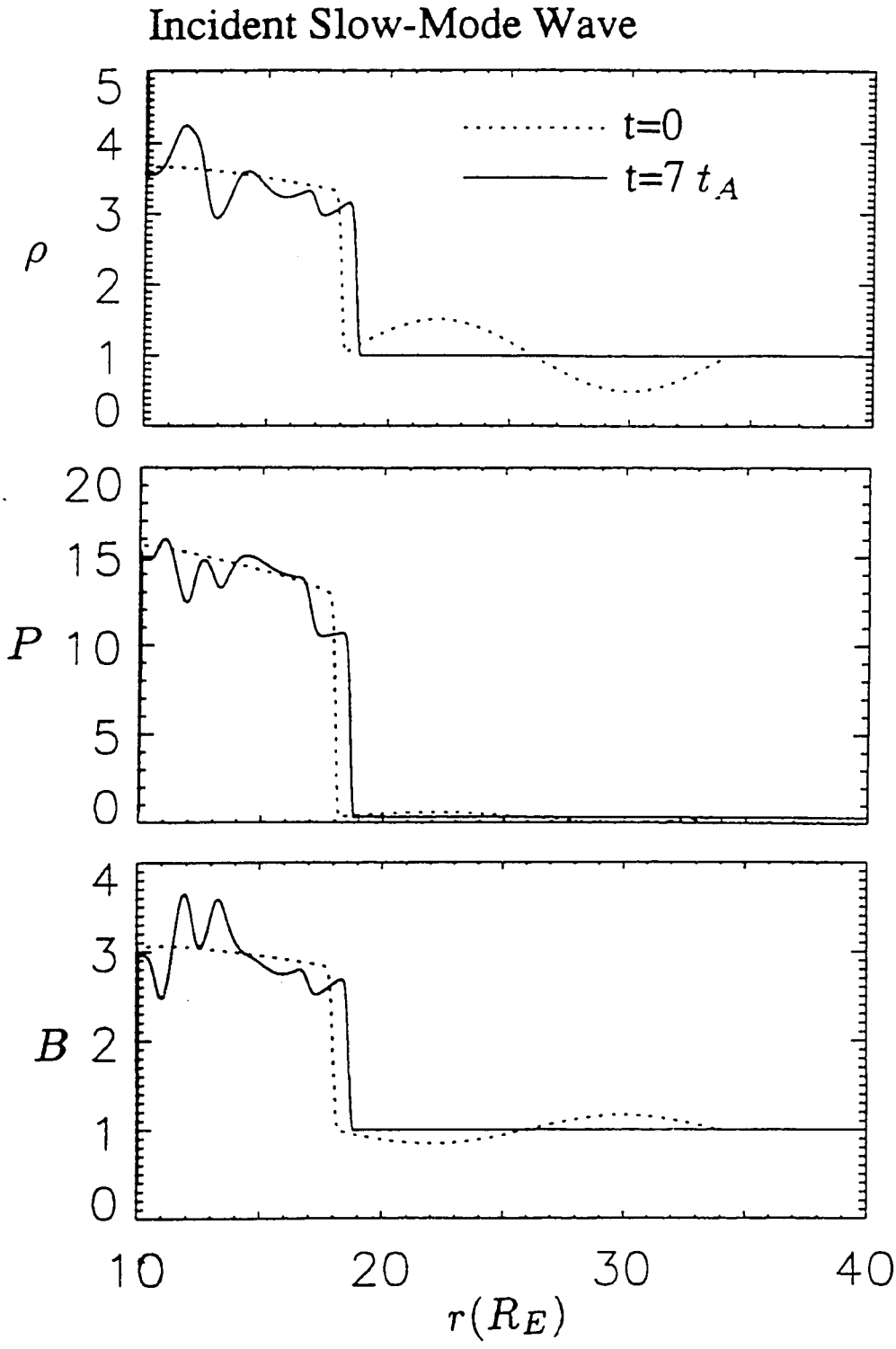

Figure 4.8 Profiles of density ρ, pressure P, and magnetic field B at t=0 (dashed lines) and t=7t_A (solid lines) for Case B with an incident fast-mode wave.

4.4 Incident Alfven Wave

In Case 3, a large amplitude Alfven-mode wave is imposed upstream of the bow shock. Across the Alfven wave, the projection of the magnetic field on the y-z plane rotates 360^o circularly, and the corresponding plasma flow velocity in the plane also rotates by the same angle. The relative directions of the velocity and magnetic field are chosen such that the Alfven wave propagates towards Earth in the solar wind frame. This case corresponds to the incident forward rotational discontinuity discussed in Section 3.5, but the wave length for this incident Alfven wave is set to be the same as the incident magnetosonic waves in Section 4.3.

There is no strong fast-mode wave generated from the interaction between the bow shock and the incident Alfven wave, which agrees with the one-dimensional simulation in Section 3.5. Figure 4.9 shows the magnetic field lines and contours of plasma density and thermal pressure in the simulation plane at $t = 7t_A$. The corresponding profiles of plasma density, pressure, magnetic field magnitude B , and B_y along the Sun-Earth line at t=0 (dashed lines) and t=$7t_A$ (solid lines) are shown in Figure 4.10. Across the incident Alfven wave (t=0), the plasma pressure and magnetic field magnitude are constant, while B_y and B_z change sinusoidally.

The anti-correlation between the density and magnetic field at t=$7t_A$ (solid lines) indicates the presence of slow-mode waves in the inner magnetosheath. What is interesting is that there is a region in which the plasma density is higher than the background value and the corresponding magnetic field is below the background value. This slow-mode structure is divided into two structures with smaller scale length. Each of them has a peak in plasma density and a valley in magnetic field strength. Note that there is no plasma density variation in the upstream solar wind for

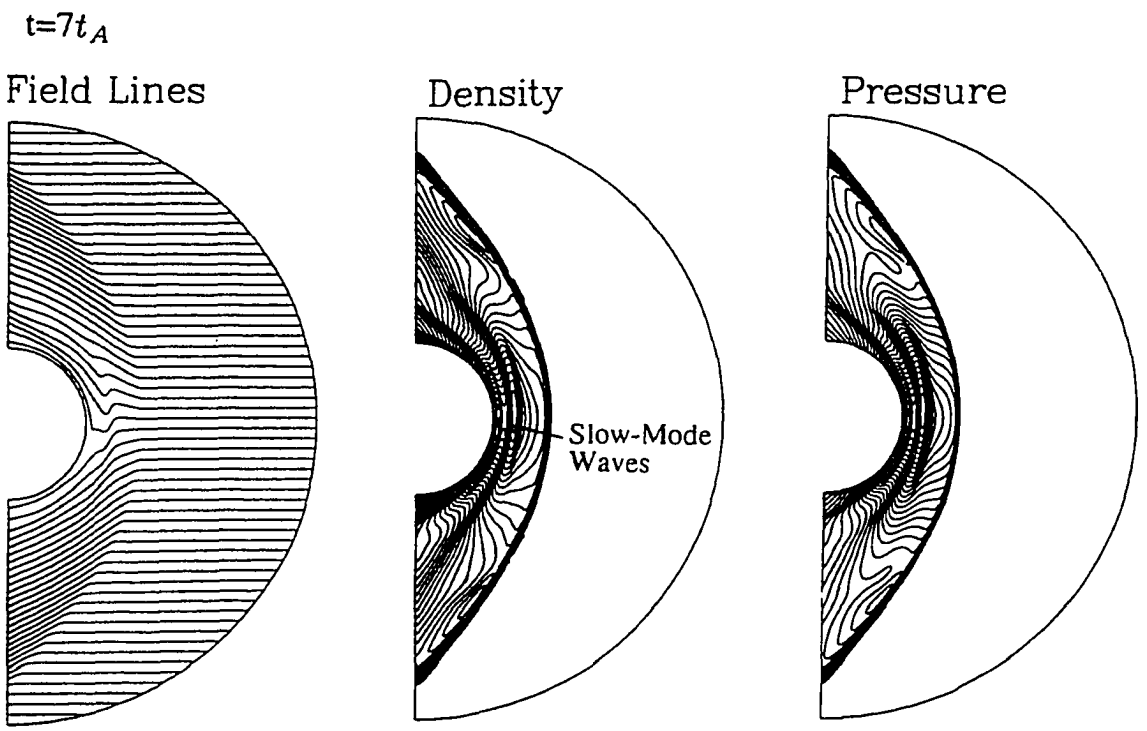

Figure 4.9 Magnetic field lines and contours of the plasma density and thermal pressure in the simulation plane at t=7t_A in the case with incident Alfven waves.

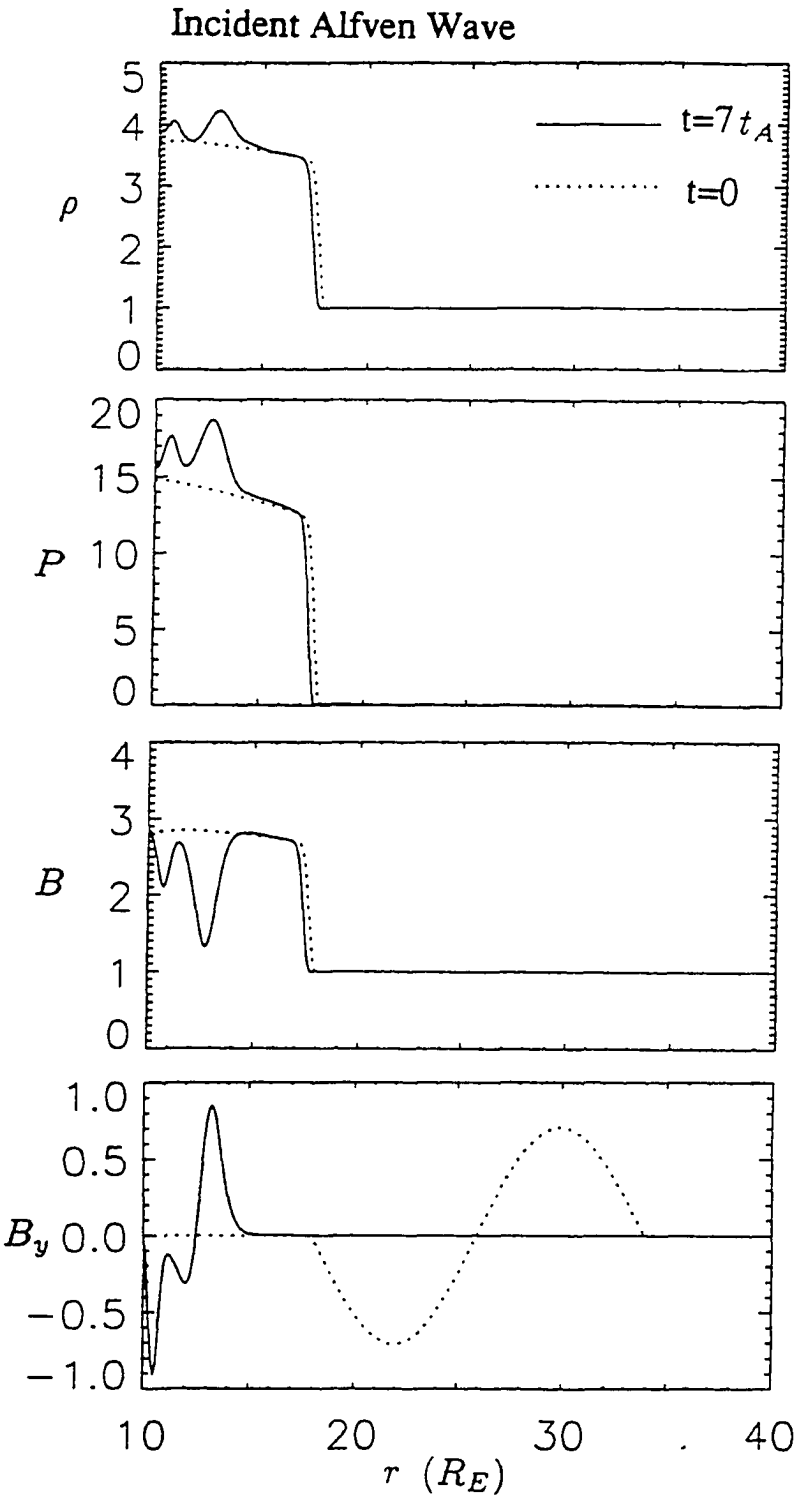

Figure 4.10 Profiles of plasma density ρ, magnetic field B, and B_y at t=0 (dashed lines) and t=7t_A (solid lines) for Case 3 with an incident Alfven wave.

the incident Alfven wave case, but slow-mode waves with enhanced plasma density and depressed magnetic field are still generated in front of the magnetopause.

Now look at the y component of the magnetic field whose variation indicates the change of magnetic field direction in the y-z plane. The direction variation is all through the generated slow-mode structure, which means that large-amplitude Alfven waves are mixed with the generated slow-mode structure. Like the magnetosonic waves, the incident Alfven wave is compressed to a smaller wavelength in the direction normal to the bow shock during its interaction with the bow shock.

The amplitudes of density and magnetic field variations are found to be larger than those in the one-dimensional simulation with the same solar wind parameters. The amplification is due to the "slow-down" of the group velocity of the slow-mode waves in the direction normal to the magnetopause. This mechanism may amplify the slow-mode waves and steepen the wave fronts.

4.5 Summary

In summary, we have developed a two-dimensional semi-global MHD simulation model to study the interaction between the bow shock and interplanetary MHD waves, which include the fast-mode, slow-mode, and Alfven waves. The simulation results can be summarized as follows.

(1) All three wave modes can lead to the presence of slow-mode waves in front of the dayside magnetopause. The plasma density and magnetic field are anti-correlated in these slow-mode waves. It should be emphasized that the directional variation of the IMF in an Alfven wave may generate slow-mode structure with an overall plasma density enhancement and a magnetic field depression in the inner magnetosheath. The

generated structure consists of smaller structures with anti-correlated plasma density and magnetic field.

(2) Fast-mode and entropy-mode waves are also generated by incident magnetosonic waves. The fast-mode wave is reflected at the magnetopause and propagates back towards the bow shock. When it finally merges into the bow shock, another slow-mode wave is generated that then propagates towards the magnetopause. No significant fast-mode wave is found to be generated in the Alfven wave incident case. However, the generated slow-mode waves are mixed with Alfven waves.

(3) Because of the small propagation speed normal to the magnetopause, these waves stay in the inner region of the dayside magnetosheath for more than 15 minutes, which is much longer than the convection time ($\sim$4 minutes) of the incident wave in the upstream solar wind. This slow propagation property makes them look like steady state structures of the inner magnetosheath.

(4) The wavelength in the direction normal to the magnetopause is much smaller than that in the tangential direction, which is due to the compression of the normal wave length at the bow shock and farther in the magnetosheath, and agrees with the observation of MHD waves in the inner magnetosheath.

Since MHD waves are often present in the solar wind, this mechanism may lead to the presence of slow-mode structures frequently observed in front of the magnetopause. The pressure anisotropy is believed to play an important role in the low frequency plasma waves in the magnetosheath [*Anderson and Fuselier*, 1993]. Its effect on the slow-mode waves in front of the magnetopause is another topic for study. Satellite observations show that the magnetopause is in constant motion which can be created by the variation of solar wind flow speed and total pressure. The movement and oscillation of the magnetopause may also generate slow-mode waves in the inner magnetosheath, which will be studied in the future.

Chapter 5 Discussion and Summary

Fluctuations of the plasma density and magnetic field on time scales over 5 minutes frequently appear in the magnetosheath. As in the four example cases of chapter 2, the fluctuations have their sources in the solar wind. However, fluctuations in the solar wind are strongly modified at the bow shock and can be quite different from those observed in the magnetosheath. In example Cases 3 and 4, the slow-mode structures observed in the inner magnetosheath with plasma density enhancements and magnetic field depressions are not caused by variations in the plasma density and the amplitude of the magnetic field: It is the variations of the IMF direction that lead to the slow-mode structures in the inner magnetosheath.

As studied in the MHD simulations in chapters 3 and 4, the interactions between Earth's bow shock and rotational discontinuities or large-amplitude Alfven waves in the solar wind generate slow-mode structures in the magnetosheath. The generated structure with enhanced plasma density and thermal pressure and depressed magnetic field is similar to the observed slow-mode structure in the inner magnetosheath. The thickness of the plateau in the plasma density generated through the interaction between an incident rotational discontinuity and the bow shock can be estimated by considering one of the edges of the density plateau is mainly an intermediate shock while the other edge is mainly a slow shock. Assume that the slow shock and the intermediate shock propagate, respectively, at the phase speeds C_s of the slow-mode waves and C_I of the Alfven mode waves. The plateau between the intermediate shock

and the slow shock has a thickness

$$d = (C_s + C_I)t \tag{5.1}$$

where

$$t = L_b/v \tag{5.2}$$

Here L_b is the distance from the observation point to the bow shock and v is the flow speed in the magnetosheath. In the region near the subsolar point, $L_d \approx 3R_E$, $v \approx 100$ km/s, and $C_I \approx C_s \approx 15$ km/s. The thickness of the density plateau is then $\approx 0.9\ R_E$, which is of the same order as the width of the slow-mode structure observed in the magnetosheath [*Song et al.*, 1992]. Note that the plateau is not formed immediately after the interaction at the bow shock. It is formed gradually as its leading and trailing edges separate from each other. This can explain why the slow-mode structures are often observed in the inner magnetosheath and not in the region close to the bow shock. As shown in the incident Alfven wave case in chapter 4, several slow-mode structures with a smaller spatial scale appear in the generated large-scale structure. The smaller-scale structures also exhibit an enhanced plasma density and depressed magnetic field. These properties appear in the satellite observations as in the example Case 3 and 4 of chapter 2.

It seems that the magnetosheath favors slow-mode fluctuations instead of fast-mode fluctuations for time scales over 5 minutes. According to the statistical results, 98% of the large-scale fluctuations in the plasma density and the magnetic field are slow-mode fluctuations, where there is an anti-correlation between the plasma density and the magnetic field magnitude. Our theoretical studies show that when an interplanetary fast or slow-mode wave crosses the bow shock into the magnetosheath, both fast-mode and slow-mode waves are generated in the

magnetosheath. The interaction between an interplanetary Alfven wave or rotational discontinuity generates a slow-mode structure in the magnetosheath with enhanced plasma density and depressed magnetic field. The observed dominant slow-mode structures in the magnetosheath agree with the observational fact that the solar wind fluctuations are mainly Alfven waves.

Figure 4.6 shows that the number of slow-mode events increases from the outer magnetosheath to the inner magnetosheath. About 69% of the events occurred in the inner 1/3 of the magnetosheath. This observation result also agrees with the bow shock-Alfven wave interaction model. According to the simulations, the plateau of the plasma density is formed gradually as its leading edge and trailing edge gradually separate from each other. If the structure is encountered by the satellite in the region close to the bow shock, the plateau has not formed yet since its leading edge and trailing edge do not have the time to separate from each other. They cannot be detected as large-scale structures even though the plateau has already formed. In the outer magnetosheath, the convection speed is about 100 km/s. Assuming that the structure has a thickness of 1 R_E, it takes only 1 minute for the satellite to pass through it. However, their propagation speeds become very small as they are close to the magnetopause as in the simulation in chapter 4. There it might take half an hour for the satellite to go through the structure.

It is shown in the statistical results that the observed slow-mode events with density enhancements greater than 50% are more frequently observed in the inner magnetosheath, which suggests there exists some amplification to the slow-mode waves during the process in which they are convected to the inner magnetosheath. The first amplification effect comes from the "slow down" of the plasma flow from the post bow shock to the magnetopause. As discussed in chapter 4, this gives an amplification of the slow-mode waves, making the fluctuations larger and steeper.

Another amplification effect is the plasma β variation in the magnetosheath. Because of the gradual pile-up of the magnetic field and the gradual depletion of the plasma density from the bow shock to the magnetopause, the plasma β value decreases from very high value right downstream of the bow shock to a relatively low value. The β value can be below unity in the area close to the magnetopause. For a slow-mode wave, the relative plasma density and pressure variations are higher relative to the magnetic field variations when the background plasma β is low. Thus the generated slow-mode expansion waves and shocks may have a stronger plasma density and pressure variations as they are convected into the low β area close to the magnetopause. The second amplification effect does not appear in the two-dimensional simulation in chapter 4 since there is no pile up of the magnetic field in the simulation plane and no plasma density depletion.

Figure 4.6 may also suggest that some of the slow-mode structures observed in the inner magnetosheath are generated locally. Actually, these events were first reported by *Song et al.* [1992]. Further observational studies are needed to answer the questions about how many of the slow-mode events in the inner magnetosheath come from the upstream region and how many are generated locally. One possible mechanism to generate these slow-mode waves locally is the motion of the magnetopause, the inner boundary of the magnetosheath. The magnetopause is moving all the time because of solar wind pressure variations or large-scale surface waves on the magnetopause. The outward motion compresses the magnetosheath plasma and magnetic field, which may generate waves in the magnetosheath. Such slow-mode waves should stay in the inner magnetosheath until their energy is convected to the tailside.

As an interplanetary shock propagates through the bow shock, the dynamic pressure variation associated with it are distributed among the shocks, expansion waves, and the contact discontinuity generated through the interaction. When the

Alfven Mach number is high, as in the case shown in Figure 3.2, most of the dynamic pressure jump at the incident shock goes to the generated fast shock or fast expansion wave. The dynamic pressure jump at the contact discontinuity is also significant. In response to the one-step jump of the dynamic pressure in the solar wind, the pressure jumps in several steps in the magnetosheath. This is similar to the cases with incident tangential discontinuities [*Wu et al.*, 1993]. In those cases, a fast shock (or a fast expansion wave) and a tangential discontinuity are generated in response to an incident tangential discontinuity. They both are responsible for significant pressure variations in the magnetosheath. It becomes more complicated when the Alfven Mach number is low, as in the case shown in Figure 3.7. In addition to the fast shock or fast expansion wave and the contact discontinuity, the slow shock and slow expansion wave may carry significant dynamic pressure variations. As a result, the overall pressure jump in the magnetosheath appears in three or more steps in response to the one-step jump in the solar wind. These stepwise pressure variations are expected to show some special signatures on ground observations.

As a rotational discontinuity or an Alfven wave in the solar wind propagates to the bow shock, there is no dynamic pressure variation associate with it. However, a structure is still generated in the magnetosheath with an enhanced dynamic pressure. The pressure enhancement is significant, heiring 100% in the case shown in Figure 3.9. This means that a variation of the IMF direction itself may create a strong transient pressure pulse in the magnetosheath, which may generate the magnetic impulse events or convection vortices in the magnetosphere [*Lanzerotti et al.*, 1986; *Friis-Christensen et al.*, 1988; *Lanzerotti et al.*, 1991; *Lee and Lysak*, 1992; *Konik et al.*, 1994].

We have studied the satellite observations of the magnetosheath and have developed MHD numerical simulation models to study the interaction between the

bow shock and interplanetary MHD fluctuations . The major findings in this thesis are listed below:

(1) Satellite observations show that fluctuations with time scales over 5 minutes frequently appear in the magnetosheath. For a dominant number of the large-scale fluctuations it is seen that the plasma density and magnetic field strength are anti-correlated, which indicates that they are slow-mode structures. These slow-mode structures are more frequently observed in the inner magnetosheath. Some of the slow-mode structures observed in the magnetosheath have their sources in the solar wind. However the modification by the bow shock may make the variations in the magnetosheath and those in the solar wind look quite different. Some of the slow-mode structures observed in the inner magnetosheath may be generated locally close to the magnetopause.

(2) Satellite observations also show that some of the slow-mode structures with enhanced plasma density and depressed magnetic field that are observed in the inner magnetosheath are associated with Alfven waves in the solar wind. In the Alfven waves, there is no variation in the plasma density or in the amplitude of the IMF, but the IMF direction changes. The MHD simulations show that the interaction between the bow shock and interplanetary rotational discontinuities or large-amplitude Alfven waves generates a slow-mode structure in the magnetosheath with enhanced plasma density and depressed magnetic field. The properties of the slow-mode structures are similar to the observations, which suggests that the observed slow-mode waves are generated through the interaction between the bow shock and interplanetary Alfven waves.

(3) The two-dimensional simulations show that the propagation of the slow-mode waves generated from the interaction between the bow shock and interplanetary fluctuations becomes very small in the direction normal to the magnetopause once

they are convected into the inner magnetosheath. This property makes them look like steady structures in front of the magnetopause. They stay in the inner magnetosheath for about 15 minutes before the wave energy is convected to the tailside by the plasma flow.

(4) The simulations show that the dynamic pressure variation associated with the slow-mode structure generated from the interaction between the bow shock and the interplanetary rotational discontinuities and large-amplitude Alfven waves can be over 100% of the local background value. When the Alfven Mach number upstream of the bow shock is small, the pressure variation becomes even larger. Considering the abundant rotational discontinuities and Alfven waves observed in the solar wind, the bow shock-Alfven wave interactions might be an important mechanism that produces pressure pulses in the magnetosheath without variations in the upstream solar wind dynamic pressure.

(5) The simulations also show that a slow shock and a slow expansion wave, in addition to a fast shock or fast expansion wave and a contact discontinuity, are generated through the interaction between the bow shock and interplanetary fast or slow shocks. The relative density variation at the slow shock or the slow expansion wave is usually below 10% even though the magnetic field variation can be very large. The overall pressure variations associated with the slow shock and the slow expansion wave becomes significant when the Alfven Mach number upstream of the bow shock is small. As a result, the overall pressure jump in the magnetosheath is in three or more steps in response to the one step jump in the solar wind. These stepwise pressure variations are expected to show some special signatures on ground observations.

It should be pointed out that this study has a potential application to magnetosheaths of other planets, to the interaction between interplanetary shocks, and to

the interaction between interplanetary shock and Alfven waves. The particle effect in the interaction processes is beyond the scope of this thesis. It can be studied through particle or hybrid simulations.

References

Anderson, B. J., and S. A. Fuselier, Magnetic pulsisions from 0.1 to 0.4Hz and associated plasma properties in the Earth's subsolar magnetosheath and plasma depletion layer, *J. Geophys. Res., 98*, 1461, 1993.

Bame, S. J., J. R. Asbridge, H. E. Felthauser, J. P. Glore, H. L. Hawk, and J. Chavez, ISEE 3 solar wind plasma experiment, *ISEE Trans. Geosci. Electron., GE-16*, 160, 1978.

Bame, S. J., J. R. Asbridge, H. E. Felthauser, J. P. Glore, G. Paschmann, P. Hemmerich, L. Lehamnn, and H. Rosenbauser, ISEE 1 and 2 fast plasma experiment and the ISEE 1 solar wind experiment, *ISEE Trans. Geosci. Electron., GE-16*, 216, 1978.

Barnes, A, Collisionless damping of hydromagnetic waves, *Phys. Fluid, 9*, 1483, 1966.

Barnes, A, and J. K. Chao, Landau damping and steepening of interplanetary nonlinear hydromagnetic waves, *J. Geophys. Res., 82*, 4711, 1977.

Berchem, J., and C. T. Russell, The thickness of the magnetopause current layer: ISEE 1 and 2 observations, *J. Geophys. Res., 87*, 2018, 1982.

Belcher, J. W., L. Davis Jr., and E. J. Smith, Large-amplitude Alfven waves in the interplanetary medium: Mariner 5, *J. Geophys. Res., 74*, 2302, 1969.

Belcher J. W., and L. Davis, Jr., Large-amplitude Alfven waves in the interplanetary medium, 2, *J. Geophys. Res., 76*, 3534, 1971.

Bonifazi, C., and G. Moreno, Reflected and diffuse ions backstreaming from the Earth's bow shock, 1, Basic properties, *J. Geophys. Res., 86*, 4397, 1981.

Brandt, J. C., *Introduction to the Solar Wind*, W. H. Freeman and Co., San Francisco, 1970.

Burlaga, L. F., A reverse hydromagnetic shock in the wind, *Cosmic Electrodn., 1*, 233, 1970.

Burlaga, L. F., Directional discontinuities in the interplanetary magnetic field, *Solar Phys. 7*, 57, 1969.

Burlaga, L. F., and J. K. Chao, Reverse and forward slow shocks in the soalr wind, *J. Geophys. Res., 76*, 7516, 1971.

Chao, J. K., and S. Olbert, Observation of slow shocks in interplanetary space, *J. Geophys. Res., 78*, 5411, 1973.

Crooker, N. U., and G. L. Siscoe, A mechanism for pressure anisotropy and mirror instability in the dayside magnetosheath, *J. Geophys. Res., 82*, 185, 1977.

Crooker, N. U., T. E. Eastman, and G. S. Stiles, Observation of plasma depletion in the magnetosheath at the dayside magnetopause, *J. Geophys. Res., 84*, 869, 1979.

Crooker, N. U., T. E. Eastman, L. A. Frank, E. J. Smith, and C. T. Russell, Energetic magnetosheath ions and the interplanetary magnetic field orientation, *J. Geophys. Res., 86*, 4455, 1981.

Diodato, L., E. W. Greenstadt, G. Moreno, and V. Formisano, A Statistical study of the upstream wave boundary outside the Earth's bow shock, *J. Geophys. Res., 81*, 199, 1976.

Dryer, M., Bow shock and its interaction with interplanetary shocks, *Radio Sci., 8*, 893, 1973.

Elphic, R. C., Multipoint observations of the magnetopause: Results from ISEE and IMPTE, *Adv. Space Res., 8*, 223, 1988.

Elphic R. C., and C. T. Russell, ISEE-1 and -2 magnetometer observations of the magnetopause, in *Magnetospheric Boundary Layers*, edited by B. Battrick, p. 43, *Rep. ESA SP-148*, European Space Agency, Paris, 1979.

Fairfield, D. H., Bow shock associated waves observed in the far upstream interplanetary medium, *J. Geophys. Res., 74*, 3541, 1969.

Fairfield, D. H., Average and unusual locations of the earth's magnetopause and bow shock, *J. Geophys. Res., 76*, 6700, 1971.

Fairfield, D. H., Waves in the vicinity of the magnetopause, in *Magnetospheric Particles and Fields*, p. 67, B. M. McCormac ed., D. Reidel Pub. Co., Dordrecht-Holland, 1976.

Farris, M. H., S. M. Petrinec, and C. T. Russell, The thickness of the magnetosheath: constants on the polytropic index, *Geophys. Res. Lett., 18*, 1821, 1991.

Frandsen, A. M. A., B. V. Connor, J. Van Amersfoort, and E. J. Smith, The ISEE 3 vector helium magnetometers, *ISEE Trans. Geosci. Electron., GE-16*, 195, 1978.

Friis-Christensen, E. M. A. McHenry, C. R. Clauer, and S. Vennerstrom, Ionospheric traveling convection vortices observed near the polar cleft: a triggered response to sudden changes in the solar wind, *Geophys. Res. Lett., 15*, 253, 1988.

Goodrich, C. C., and P. J. Cargill, An investigation of the structure of rotational discontinuity, *Geophys. Res. Lett., 18*, 65, 1991.

Gleaves, D. G. and D. J. Southwood, Magnetohydrodynamic fluctuations in the Earth's magnetosheath at 1500LT: ISEE 1 and ISEE 2, *J. Geophys. Res., 96*, 129, 1991.

Gosling, J. T., J. R. Asbridge, S. J. Bame, G. Paschmann, and N. Sckopke, Observation of two distinct populations of bow shock ions in the upstream solar wind, *Geophys. Res. Lett., 5*, 95, 1978.

Gosling, J. T., and E. Robson, Ion reflection, gyration, and dissipation at supercritical shocks, in *Collisionless Shocks in the Heliosphere: Reviews of Current Research, Geophys. Monogr. Ser., Vol. 35*, edited by B. T. Tsurutani and R. G. Stone, p. 141, AGU, Washington D. C., 1985.

Greestadt, E. W., I. M. Green, G. T. Inouye, D. S. Colburne, J. H. Binsack, and E. F. Lyon, Dual satellite observation of the Earth's bow shock, 1, The thick pulsation shock, *Cosmic Electrodyn., 1*, 160, 1970a.

Greestadt, E. W., I. M. Green, G. T. Inouye, D. S. Colburne, J. H. Binsack, and E. F. Lyon, Dual satellite observation of the Earth's bow shock, 2, Field-aligned upstream waves, *Cosmic Electrodyn., 1*, 279, 1970b.

Greestadt, E. W., and R. W. Fredricks, Shock systems in the collisionless plasmas, in *Solar System Plasma Physics, 3*, ed L. J. Lanzerotti, C. F. Kennel, and E. N. Parker, p. 3, North-Holland, Amsterdam, 1979.

Hada, T., and C. F. Kennel, Nonlinear evolution of slow waves in the solar wind, *J. Geophys. Res., 90*, 531, 1985.

Hoppe, M. M., C. T. Russell, L. A. Frank, T. E. Eastman, and E. W. Greenstadt, Upstream hydromagnetic waves and their association with backstreaming ions populations: ISEE-1 and ISEE-2 observations,*J. Geophys. Res., 86*, 4471, 1981.

Hundhausen, A. J., Interplanetary shock wave and the structure of solar wind disturbances, in *Solar Wind*, edited by C. P. Sonett, P. J. Coleman, and J. M. Wilcox, NASA SP-308, Washington, 393, 1972.

Hunderhausen A. J., *Coronal Expansion and Solar Wind*, Spring-Verlag, New York, Heidelberg, Berlin, 1972.

Hundhausen, A. J., T. E. Holzer, and B. C. Low, Do slow shocks precede some coronal mass ejections?, *J. Geophys. Res., 92*, 11,173, 1987.

Hubert, D., C. Perche, C. C. Harvey, C. Lacombe, and C. T. Russell, Observation of mirror waves downstream of a quasi-perpendicular shock, *Geophys. Res. Lett., 16*, 159, 1989.

Kaufmann, R. L. J.-T. Horng, and A. Wolfe, Large amplitude hydromagnetic waves in the inner magnetosheath, *J. Geophys. Res., 75*, 4666, 1970.

Kaufmann, R. L., and A. Konradi, Explorer 12 magnetopause observations: Large scale nonuniform motion, *J. Geophys. Res., 71*, 1481, 1969.

Kobel, E., and E. O. Fluckiger, A model of the steady state magnetic field in the magneosheath, *J. Geophys. Res., 99*, 23,617, 1994.

Konik, R. M., L. J. Lanzerotti, A. Wolfe, and C. G. Maclennan, Cusp-latitude magnetic impulse events, 2, interplanetary magnetic field and solar wind conditions, *J. Geophys. Res., 99*, 14,831, 1994.

Krauss-Varban, D., and N. Omidi, Structure of medium Mach number quasi-parallel shocks: upstream and downstream waves, *J. Geophys. Res., 96*, 17,715, 1991.

Lanzerotti, L. J., L. C. Lee, C. G. Maclennan, A. Wolfe, and L. Medford, Possible evidence of flux transfer events in the polar ionosphere, *Geophys. Res. Lett., 13*, 1089, 1986.

Lanzerotti, L. J., R. M. Konik, A. Wolfe, D. Venkatesan, and C. G. Maclennan, Cusp-latitude magnetic impulse events, 1, occurrence statistics, *J. Geophys. Res., 96*, 14,009, 1991.

Lee D.-H., and R. L. Lysak, Response of the dipole magnetosphere to pressure pulses, *Geophys. Res. Lett., 19*, 937, 1992.

Lee, L. C., and Z. F. Fu, A theory of magnetic flux transfer at the earth's magnetopause, *Geophys. Res. Lett., 12*, 105, 1985.

Lee, L. C., and M. Yan, Structure of field-aligned plasma jets associated with magnetic reconnection, to be published in *Phys. Fluids, B4*, 1992.

Lee, L. C., C. P. Price, C. S. Wu, and M. E. Mandt, A study of mirror waves generated downstream of a quasi-perpendicular shock, *J. Geophys. Res., 93*, 247, 1988.

Lee, L. C., M. Yan, and J. G. Hawkins, A study of slow mode structures in the dayside magnetosheath, *Geophys. Res. Lett., 18*, 381, 1991.

Lees, L., Interaction between the solar wind and the geomagnetic cavity, *AIAA J., 2*, 1576, 1964.

Lin, Y. and L. C. Lee, Structure of the dayside reconnection layer in resistive MHD and hybrid models, *J. Geophys. Res., 98*, 3919, 1993.

Luhmann, J. G., C. T. Russell, and R. C. Elphic, Spatial distributions of magnetic field fluctuations in the dayside magnetosheath, *J. Geophys. Res., 91*, 1711, 1986.

Mead, G. D., and D. B. Beard, Shape of the geomagnetic field solar wind boundary, *J. Geophys. Res., 69*, 1169, 1964.

McKenzie, J. F., Hydromagnetic wave interaction with the magnetopause and the bow shock, *Planet. Space Sci., 18*, 1, 1970.

Midgely, J. E., and L. Davis, Jr., Calculation by a moment technique of the perturbation of the geomagnetic field by the solar wind, *J. Geophys. Res., 68*, 5111, 1963.

Neugebauer, M., D. R. Clay, B. E. Goldstein, B. T. Tsurutani, and R. D. Zwickl, A reexamination of rotational and tangential discontinuities in the solar wind, *J. Geophys. Res., 89*, 5395, 1984.

Ness, N. F., C. S. Scearce, J. B. Seek, and J. M. Wilcox, Summary of the results from IMP 1 magnetic field experiment, *Space Res., 6*, 581, 1966.

Otto, A., L. C. Lee, and Z. W. Ma, Magnetic field and plasma properties associated with pressure pulses and magnetic reconnection at the dayside magnetopause, submitted to *J. Geophys. Res.*, 1994.

Paschmann, G., N. Sckopke, G. Haerendel, et al., ISEE plasma observations near subsolar magnetopause, *Space Sci. Rev., 22*, 717, 1978.

Phan, T.-D., G. Paschmann, W. Baumjohann, N. Sckopke, and H. Luhr, The magnetosheath region adjacent to the dayside magnetopause: AMPTE/IRM observations, *J. Geophys. Res., 99*, 121, 1994.

Russell, C. T., The ISEE 1 and 2 fluxgate magnetometers, *ISEE Trans. Geosci. Electron., GE-16*, 239, 1978.

Russell, C. T. and R. C. Elphic, ISEE observations of flux transfer events at the dayside magnetopause, *Geophys. Res. Lett., 6*, 33, 1979.

Scholer, M., Upstream waves, shocklets, short large-amplitude magnetic structures and the cyclic behavior of oblique quasi-parallel collisionless shocks, *J. Geophys. Res., 98*, 47, 1993.

Scholer, M., M. Fujimoto, and H. Kucharek, Two-dimensional simulations of supercritical quasi-parallel shocks: upstream waves, downstream waves, shock reformation, *J. Geophys. Res., 98*, 18,971, 1993.

Shen, W. W., and M. Dryer, Magnetohydrodynamic theory for the interaction of an interplanetary double-shock ensemble with the Earth's bow shock, *J. Geophys. Sci., 77*, 4627, 1972.

Skopke, N., G. Paschmann, A. L. Brinca, C. W. Carlson, and H. Luhr, Ion thermalization in quasi-perpendicular shocks involving reflected ions, *J. Geophys. Res., 95*, 6337, 1990.

Sibeck, D. G., A model for the transient magnetospheric response to sudden solar wind dynamic pressure variations, *J. Geophys. Res., 94*, 3755, 1990.

Sibeck, D. G., et al., The magnetospheric response to 8-minute period strong-amplitude upstream pressure variations, *J. Geophys. Res., 94*, 2505, 1989.

Siscoe, G. L., L. Davis, Jr., P. J. Coleman, Jr., E. J. Smith, and D. E. Jones, Power spectra and discontinuities of the interplanetary magnetic field: Mariner 4, *J. Geophys. Res.*, *73*, 61, 1968.

Song, P., C. T. Russell, J. T. Gosling, M. Thomsen, R. C Elphic, Observation of the density profile in the magnetosheath near the stagnation streamline, *Geophys. Res. Lett.*, *17*, 2035, 1990.

Song, P., C. T. Russell, M. Thomsen, Slow mode transition in the front side magnetosheath, *J. Geophys. Res.*, *97*, 8295, 1992.

Southwood, D. J. and M. G. Kivelson, On the form of the flow in the magnetosheath, *J. Geophys. Res.*, *97*, 2873, 1992.

Spreiter, J. R. and A. Alksne, Plasma flow around the magnetosphere, *Rew. Geophys.*, *7*, 11, 1969.

Spreiter, J. R., and B. R. Briggs, Theoretical determination of the form of the boundary of the solar corpuscular stream produced by interaction with the magnetic dipole field of the Earth, *J. Geophys. Res.*, *67*, 37, 1962.

Spreiter, J. R., A. L. Summers, and A. Y. Alksne, Hydromagnetic flow around the magnetosphere, *Planetary Space Sci.*, *14*, 223, 1966.

Swift, D. W., and L. C. Lee, Rotational discontinuities and the structure of the magnetopause, *J. Geophys. Res.*, *88*, 111, 1983.

Steinolfson, R. S., and A. J. Hundhausen, Concave-outward slow shocks in coronal mass ejections, *J. Geophys. Res.*, *95*, 15,251, 1990.

Tsurutani, B. T., E. J. Smith, R. R. Anderson, K. W. Ogilvie, J. D. Scudder, D. N. Baker, and S. J. Bame, Lion roars and nonoscillatory drift mirror waves in the magnetosheath, *J. Geophys. Res., 87*, 6060, 1982.

Turner, J. M., and G. L. Siscoe, Orientation of the 'rotational' and 'tangential' discontinuities in the solar wind, *J. Geophys. Res., 76*, 1816, 1971.

Volk, H. J., and R. D. Auer, Motion of the bow shock induced by interplanetary disturbances, *J. Geophys. Res., 79*, 40, 1974.

Whang Y. C., Slow shocks and their transition to fast shocks in the inner solar wind, *J. Geophys. Res., 92*, 4349, 1987.

Whang Y. C., Shock interactions in the outer heliosphere, *Space Sci. Rev., 57*, 339, 1991.

Winske, D., and K. B. Quest, Magnetic field and density fluctuations at perpendicular supercritical shocks, *J. Geophys. Res., 93*, 9681, 1988.

Wolfe, J. H., The large-scale structure of the solar wind, *Solar Wind*, p. 170, C. P. eds. Sonett, P. J. Coleman, and J. M. Wilcox, NASA, Washington, 1972.

Wu, B. H., M. E. Mandt, L.C. Lee and J. K. Chao, Magnetospheric response to solar wind dynamic pressure variations: interaction of interplanetary tangential discontinuities with the bow shock, *J. Geophys. Res., 98*, 21,297, 1993.

Wu, C. C., Effects of dissipation on rotational discontinuities, *J. Geophys. Res., 93*, 3969, 1988.

Wu, C. C., MHD flow past an obstacle: Large-scale flow in the magnetosheath, *Geophys. Res. Lett., 19*, 87, 1992.

Yan, M., L. C. Lee and E. R. Priest, Fast magnetic reconnection with small separatrix angles, *J. Geophys. Res., 97*, 8277, 1992.

Yan, M., L. C. Lee and E. R. Priest, Magnetic reconnection with large separatrix angles, *J. Geophys. Res., 98*, 7593, 1993.

Yan, M., A. Otto, D. Muzzell, and L.C. Lee, Tearing mode instability in a multiple current sheet system, *J. Geophys. Res., 99*, 8657, 1994.

Yan, M., and L. C. Lee, Generation of slow-mode waves in front of the dayside magnetopause, *Geophys. Res. Lett., 21*, 629, 1994.

Zwan, B. J. and R. A. Wolf, Depletion of solar wind plasma near a planetary boundary, *J. Geophys. Res., 81*, 1636, 1976.